Modeling Long Term Performance of Floating Offshore Wind Turbines During Wind and Wave Induced Platform Motion

Jackson Pilgrim Hardin

Oriel College

University of Oxford

A thesis submitted for the degree of

Msc by Research in Engineering Science

Trinity 2025

Acknowledgments

I would like to dedicate this thesis and all of the work it represents to my loving family who have supported me through the duration of this degree. To Mom, Dad, K, thank you for supporting my move overseas, coming to visit me countless times, and always being only a phone call away. To Liza, for making it work when we were apart and then making it so that we didn't have to be. I love you all.

I would also like to thank my supervisors Emma, Tom, and Federico. Through a tumultuous two years, the three of you have pulled together to make sure that I was never without guidance and help. Thank you for everything.

Abstract

Floating offshore wind energy has been identified as a critical source of future sustainable energy. This work characterizes the performance difference between floating and fixed offshore wind turbines in a large variety of operational conditions to better inform design decisions for floating turbines. Emphasis is placed on parameters that will drive the long-term performance of floating offshore wind turbines such as power performance, annual energy production, and contributors to component fatigue. The large number of test cases required to holistically understand the performance of floating versus fixed wind turbines necessitates fast-to-run analysis methods. However, the lower fidelity models typically utilized in wind energy analysis are challenged by the dynamic case of a freely floating turbine. First, the discrepancy between blade element momentum theory simulations and higher fidelity methods for floating turbines is characterized to better understand which metrics and range of conditions blade element momentum theory is effective for. In addition, the accuracy of blade element momentum theory for the floating case is quantified. Trends in the performance of a reference floating wind turbine undergoing prescribed harmonic motion across its operational wind speed range are then identified. Prescribed surge motion is found to increase turbine power capture at low wind speeds and decrease power capture near the rated wind speed. This effect is coupled with a large increase in the fluctuating components of turbine power and rotor thrust. A coupled aero-hydrodynamic floating offshore wind turbine model is then developed to simulate realistic platform and rotor motion. Turbine performance under a large range of regular wave loading is examined. Finally, floating offshore wind turbine performance is compared to static turbine performance under site-specific environmental conditions at four different representative case study locations. Performance metrics over one year are compared, and environmental parameters are identified which drive floating offshore wind turbine performance. The model predicts that the floating turbine will perform equal to or better than a static turbine baseline in power capture and annual energy production, but undergoes large load fluctuations contributing to component fatigue damage. The magnitude of load fluctuation due to platform motion is significant, but less than the contribution from wind speed turbulence.

Contents

Chapter 1

Introduction

We are currently in the midst of a climate crisis due to anthropogenic greenhouse gas emissions. Global average surface temperatures are predicted to increase by at least 2.0 degrees Celsius by 2100 relative to levels between 1850 and 1900 [1]. In order to combat the current climate crisis, sustainable, low-carbon energy sources must be tapped into. Offshore wind energy has successfully been demonstrated to generate large amounts of sustainable electricity, helping to meet global emission reduction goals. Moreover, the offshore wind resource is often conveniently located close to large coastal population centers [2]. In the past decade floating offshore wind turbines (FOWTs) have increasingly been identified as an important renewable energy source [3]. These floating turbines can be installed at greater water depths where average wind speeds are higher [4], and the ocean's low surface roughness results in less turbulent flow [5, 6], essentially harnessing a better wind energy resource than is available on or close to shore. The Global Wind Energy Commission estimates that 80 % of the world's offshore wind resource is located at water depths of greater than 60 meters [3], beyond the depth at which fixed bottom turbines are economically feasible. The international rise in FOWT capacity is illustrated in Figure 1.1, reproduced from Edwards et al. [7].

At the time of writing, there exists an installed capacity of 171 MW of floating offshore wind in Europe, making up 91 percent of the worldwide FOWT capacity. The largest farms include the Hywind Tampen farm in Norway [8] totaling 88 MW, the Hywind Scotland and Kincardine floating wind farms [9] in Scotland totaling 30 and 48 MW, and the WindFloat Atlantic project [10] in Portugal totaling 25 MW of installed capacity. Despite its advantages, floating wind is currently less cost-effective than onshore wind [11], largely due to the cost of designing, constructing, and transporting these large floating structures. However, the field of FOWT design is young, and we expect significant cost reduction through improved platform, rotor,

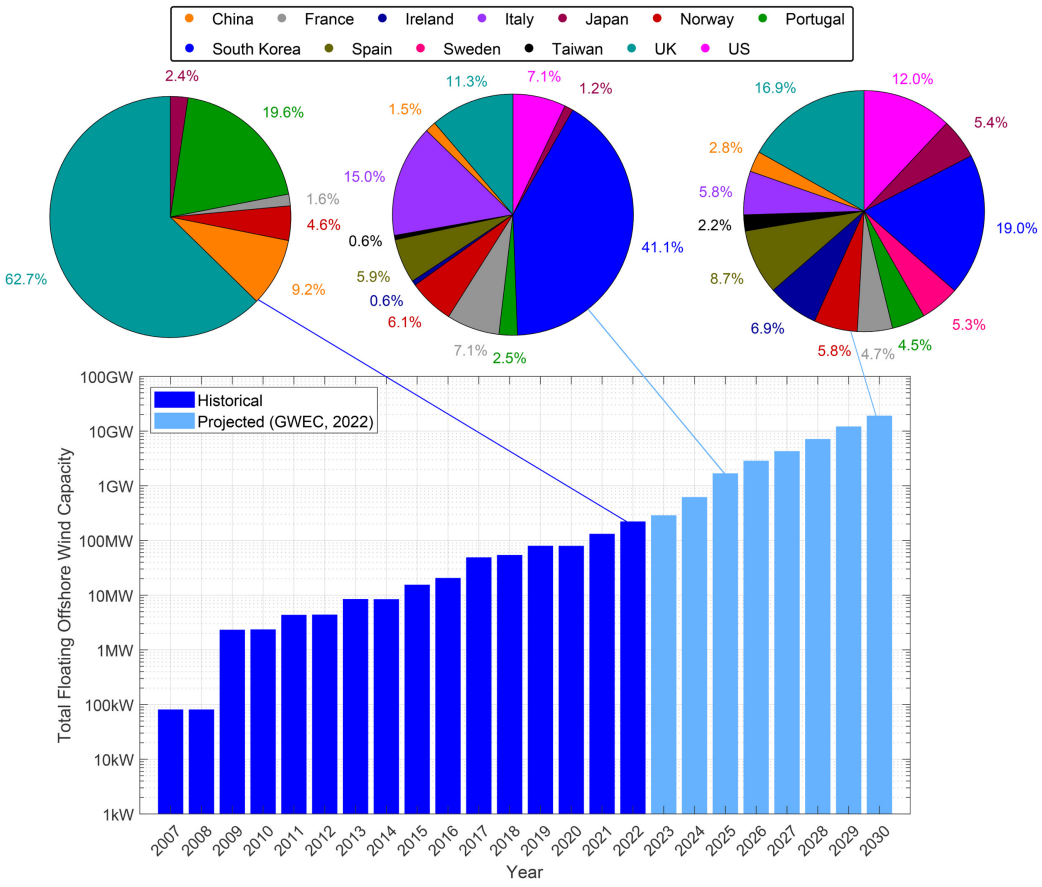

Figure 1.1: Historical (dark blue) and projected (light blue) global floating offshore wind capacity, with percentages of current (2022) installed and projected (2025 and 2030) capacity by country (top). Reproduced with permission of the authors from Edwards et al. 2023.

and controller design [11]. Cost reduction is also expected through the development of floating wind specific manufacturing and assembly facilities [12], as well as systems engineering optimization of the FOWT life-cycle design process [13].

Importantly, FOWTs experience six degree of freedom motion induced by wind and ocean waves [14, 15]. This fundamental difference to fixed bottom turbines results in significant changes to power performance and rotor loading. In order to characterize the effect of a system design decision such as turbine site selection, or choice of floating platform, a holistic analysis is required. This analysis should determine the performance of the FOWT system in a wide variety of wind and wave conditions, accounting for the follow-on motion effects. The number of test cases required to achieve this can be substantial. For example, the International Electrotechnical Commission lays out 39 design load cases in its offshore wind energy generation systems minimum design requirements as well as referencing 10 other design requirement documents which are applicable on a case by case basis [16]. As such, a huge number of test cases can be necessitated throughout the FOWT design process. Additionally, fixed offshore wind installations typically operate for 20 to 30 years [17]. We expect FOWTs to follow this trend, so performance metrics such as power and thrust coefficients and the average and fluctuating components of rotor loading must be analyzed over long time scales (months, years).

High-fidelity tools for the aerodynamic analysis of moving turbines such as blade-resolved, Reynolds averaged Navier-Stokes computational fluid dynamics (RANS-CFD) and actuator line computational fluid dynamics (ACL-CFD) models have demonstrated good accuracy in describing rotor and blade forces during operation. Liu et al. 2017 [18] present a fully coupled CFD analysis tool for FOWTs which utilizes a RANS-CFD aerodynamic solver. Their model predicts aerodynamic thrust and torque in static turbine tests with less than 11 % difference to experimental results from the NREL Phase VI turbine for all wind speeds tested.

Tran and Kim 2016 [19] used a three-dimensional, blade-resolved, RANS-CFD model to study the NREL 5 MW reference turbine under surge motion of varying frequency and amplitude. The problem is simplified by applying a set surge oscillation to the turbine model instead of predicting the motion that would be induced by a certain sea state. Their model found significant variation in both thrust and torque, increasing as frequency and amplitude increase. In an example worst-case scenario of 0.123 Hz frequency and 8 m (or 0.0625 rotor diameters) amplitude, the turbine thrust coefficient varies between 0.18 and 1.19, while the power coefficient varies between 0 and 1.3. Both power and thrust coefficients are relative to the free stream wind speed

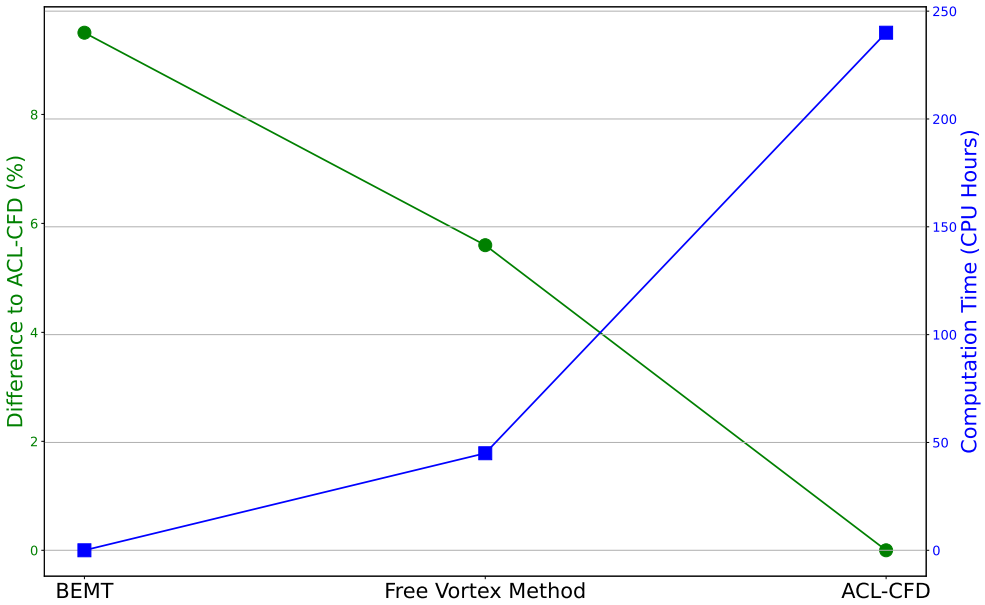

Figure 1.2: The percent difference compared to the highest fidelity model and computational expense of an ACL-CFD, FVM, and BEMT aerodynamic model for predicting rotor integrated parameters of a FOWT undergoing platform motion. Figure adapted from Shaler et al. [23]

and can exceed one when platform motion causes the relative wind speed experienced by the rotor to exceed the free stream velocity.

Mid-fidelity models such as free vortex wake methods (FVM) have also shown success in FOWT modeling. Sebastian and Lackner [20] utilized a FVM model and were able to predict thrust and power coefficients with less than 1.5 percent error compared to experimental results from the Energy Research Center of the Netherlands' MEXICO rotor. Lee and Lee [21] and Ramos-Garcia et al. [22] have also used FVM to model turbines in prescribed platform motion, predicting large variations in turbine performance under prescribed motion.

Despite their accuracy, these higher fidelity models can be orders of magnitude more computationally expensive than the low fidelity blade element momentum theory (BEMT) [23]. This discrepancy is illustrated in Figure 1.2 which shows the computational expense of an ACL-CFD, FVM, and BEMT model, as well as the percent difference of the FVM and BEMT models to the higher fidelity ACL-CFD.

In addition to the high volume of test cases, the analysis of floating wind is further complicated by the inclusion of system hydrodynamics. FOWTs are a coupled aerodynamic-hydrodynamic system in which the floater hydrodynamics induce motion that affects the turbine aerodynamics, which in turn generate forces that affect

the hydrodynamic force balance. As such, a true analysis of the FOWT system must include both an aerodynamic and hydrodynamic solver. This only exacerbates the computational expense of effective FOWT models.

Computationally inexpensive numeric models can be very effective tools, as they are fast enough [23] to allow for extensive simulation over a wide range of conditions. Performance prediction over a wide range of operating conditions allows us to develop a holistic performance assessment for FOWTs compared to fixed wind turbines.

Low-fidelity models have been used to examine turbine performance in prescribed harmonic motion [24], [25], [26]. We will extend this methodology to generate motion-adjusted performance curves for a large turbine representative of future FOWT installations. These motion-adjusted performance curves can be used during site-selection processes and for wind resource assessment. Low-fidelity modeling has also been used to study FOWT motion responses and performance in regular wave loading [27], [28], and irregular wave loading [29], [30]. We extend this work by examining both the motion response and power and thrust performance of a large FOWT in a wider range of regular wave loading than previously studied. We then analyze turbine performance in irregular sea states through four case studies of long-term FOWT performance in varying site locations. The effect of site-specific sea states, and particularly wind-wave misalignment, is examined in detail.

In this project we will explore the difference between floating and fixed turbine performance in realistic operating conditions over long time spans, taking into account the effects of sea-state induced platform motion. We aim to compare the performance of FOWTs to their fixed turbine counterparts in a large number of operational wind and sea-states over long time spans, while varying specific FOWT design variables. To do this, we will begin by validating lower fidelity aerodynamic models for the floating case and quantifying their error relative to higher fidelity methods. It is necessary to use low-fidelity models for this application, as it allows for comparison of fixed and floating turbines while testing a large number of cases over long time periods. The project will then continue to modeling of FOWTs as a coupled hydrodynamic - aerodynamic system. FOWT performance will be compared to a static turbine's performance over long time periods as variables such as wind and sea-state are varied.

This thesis is divided into four main sections followed by a conclusion. Each section contains an introduction to the topic and a review of the most relevant literature. In Chapter 2, we explore the use of the low-fidelity blade element momentum theory to analyze the average and fluctuating components of turbine power capture and rotor

thrust. We compare an in-house BEMT model to three higher-fidelity models. An in-house BEMT implementation was selected over an off-the-shelf tool such as OpenFast [31] or HAWC2 [32], to allow for maximum flexibility in testing various empirical corrections. An in-house BEMT code also maximizes our ability to tune both the aerodynamic and coupled models during development. The in-house BEMT model is compared to a blade-resolved RANS-CFD model and two experimental models which utilize a performance scaling methodology in test cases with prescribed rotor motion.

In Chapter 3, the aerodynamic model is used to predict turbine performance during prescribed, harmonic platform surge motion at two representative platform natural frequencies and a representative wave frequency. We present power and thrust performance curves for a large FOWT adjusted for the effect of this platform motion.

Chapter 4 presents a coupled aero-hydrodynamic model based upon the in-house BEMT aerodynamic model and a potential flow-based hydrodynamic time domain model. This coupled model is used to explore turbine performance at operational wind speeds under regular wave loading with a wide range of frequencies, amplitudes, and wave headings.

Finally, in Chapter 5, we examine the performance of a representative FOWT in realistic irregular sea states based on environmental conditions from four case study locations in the United States and the United Kingdom. We characterize the wind and sea state at these locations from 12 months of data and simulate turbine performance to generate site-specific power and thrust performance curves and predictions of site-specific annual energy production. We also analyze the effect of wind and wave misalignment on the average and fluctuating components of turbine power and rotor thrust.

Chapter 2

Characterizing the Performance of Blade Element Momentum Theory for Predicting Rotor Integrated Parameters during Platform Motion

2.1 Introduction

Blade element momentum theory, or BEMT, has been the industry standard for wind turbine analysis for some time, being utilized by popular tools such as NREL's OpenFAST [33], CCBlade [34], QBlade [35], and HAWC2 [32]. The BEMT model is a combination of blade element theory, which analyzes a section of the turbine blade as a two-dimensional airfoil, and momentum theory, which analyzes the macroscopic momentum balance of the working fluid across the rotor plane. The combination of these two theories is used to predict blade forces, power generation, and efficiency [36]. In addition, a variety of empirical corrections such as Prandtl's hub and tip loss [37] and Glauert's turbulent wake method [38] can be used to improve BEMT accuracy. Although BEMT assumes steady flow conditions, several dynamic inflow models have been developed which aim to account for the delay in flow characteristics at the rotor after an instantaneous change in upstream flow. A variety of dynamic inflow models exist [39, 40, 41], but generally, they begin by calculating quasi-steady values of the induced velocity at the rotor and altering them with a set of dynamic inflow differential equations or filters.

A primary concern in the application of BEMT to the floating case is the theory's assumption of quasi-steady flow conditions which may be violated during rapid motion

of the rotor disk. Unsteady inflow conditions could occur during surge and pitch motion, common in FOWT operation, in which the rotor disk moves in and out of the incoming wind. To have confidence in its use for floating turbine performance prediction, BEMT analysis of FOWT platform motion must be carefully vetted and validated with experimental results or higher fidelity numerical methods.

Apsley and Stansby [42] compared a BEMT solver to actuator line CFD for a static turbine, finding 1.5 % average difference in power coefficient for all tip speed ratios, and 1.8 % average difference in thrust coefficient for tip speed ratios between 2 and 8. In addition, BEMT predicted turbine power performance in oscillating flows with less than 15 % error relative to ACL-CFD. De Vaal and Moen [25] utilized BEMT with various dynamic inflow models to analyze power performance of the NREL 5 MW reference turbine and validated their model against a RANS CFD model in ANSYS FLUENT, achieving a maximum error of 5 percent.

Bergua et al. [43] describe the work conducted in Phase III of the OC6 project in which 54 aerodynamic solvers including BEMT, BEMT with dynamic inflow corrections, Generalized Dynamic Wake (GDW), Free Vortex Method (FVM), and CFD models are compared to experimental results from the UNAFLOW campaign [44]. They find that dynamic inflow corrections do not significantly improve the accuracy of BEMT in prescribed harmonic surge motion. Moreover, steady BEMT is seen to perform within 10 % difference to the higher fidelity FVM and CFD when simulating turbine operation with fixed blade pitch and fixed rotor speed. However, for load cases in which rotor speed or blade pitch are varied, the percent difference between BEMT and the higher fidelity methods increases to 15 - 20 %.

Papi et al. [45] compared rotor thrust predicted by a BEMT model, a BEMT model with a dynamic correction meant to account for the changing inflow conditions caused by platform motion, a free vortex method model, and an ACL-CFD simulation. The authors show that BEMT, both with and without the dynamic correction, predicts turbine thrust with less than 10% difference compared to the higher fidelity methods at rated wind speeds with small to medium frequency motion. However, BEMT with or without dynamic correction fails to capture the non-linear effects of motion at frequencies greater than two or three times the rotor rotational speed. As such, the types of motion studied must be determined to be within the range of accurate BEMT analysis. Additionally, the errors and inaccuracies should be well understood in order to make sound engineering decisions.

In light of these challenges, we aim to validate the use of the low fidelity blade element momentum theory for the case of rotor motion. Specifically, we aim to validate

its ability to predict turbine power output, crucial for FOWT design and economic feasibility. Additionally, we must validate the method's ability to predict rotor thrust and the fluctuation of rotor thrust, as these play an important role in the system hydrodynamic force balance, prediction of component fatigue damage, and turbine and platform design. In this chapter we characterize BEMT's accuracy in predicting rotor integrated parameters describing the mean and fluctuating components of power and thrust (C_{P}, C_{T}, ΔC_{P}, ΔC_{T}) relative to higher fidelity models. Additionally, we will determine limits to BEMT's applicability based on motion frequency and how extreme a certain platform motion is. We describe the extremity of platform motion by the normalized platform motion induced velocity (ΔU^*):

$$\Delta U^* = \frac{\max\left(\dot{X}_{\mathrm{hub}}\right)}{U_\infty}, \tag{2.1}$$

where X_{hub} is the position of the turbine hub in the free stream direction. For a simple, surge type, harmonic motion of the platform $X = A\sin(\omega t)$, where X is the platform position, A is the amplitude of motion, and ω is the frequency of motion, $\Delta U^* = \frac{A\omega}{U_\infty}$.

2.2 Methods

We elect to utilize an in-house implementation of blade element momentum theory (BEMT) to examine the effects of prescribed platform motion. The development of our own BEMT implementation allows for maximum flexibility in the selection of empirical corrections used in the model. In addition, the in-house code allows for a simple implementation, allowing us to test BEMT's baseline efficacy for modeling FOWTs without introducing the confounding variables of more complex modeling techniques such as body elasticity, dynamic stall, skewed wake, etc.

2.2.1 Classical BEMT Theory

BEMT is derived from the combination of 1-D momentum theory and blade element theory. The former conducts a conservation of mass and momentum analysis across an ideal, permeable disc representing the turbine's rotor. The latter analyzes the forces generated by a 2-D airfoil undergoing steady flow.

The BEM theory assumes that the incoming flow is quasi-steady (the free stream velocity, blade pitch, and rotor rotational speed are constant), and that the rotor may

be split into N equally spaced annuli within which the flow does not interact with any other annulus.

The torque and thrust contribution of each annulus can be expressed through momentum theory (Equations 2.2 and 2.3) and through blade element theory (Equations 2.4 and 2.5). A derivation of these expressions can be found in Hansen's *Aerodynamics of Wind Turbines* [46].

$$\mathrm{d}Q = 4\pi r^3 \rho U_\infty \Omega (1-a) a^{'} \mathrm{d}r, \tag{2.2}$$

$$\mathrm{d}T = 4\pi r \rho U_\infty^2 (1-a) a \mathrm{d}r, \tag{2.3}$$

where r is the local radius of the midpoint of the annulus, U_∞ is the free stream wind velocity far in front of the rotor, Ω is the rotational velocity of the rotor, $\mathrm{d}r$ is the width of the annulus, and ρ is the density of air.

$$\mathrm{d}Q = N_\mathrm{b} \frac{1}{2} \rho W^2 (C_\mathrm{l} \mathrm{sin}\phi - C_\mathrm{d} \mathrm{cos}\phi) c r \mathrm{d}r, \tag{2.4}$$

$$\mathrm{d}T = N_\mathrm{b} \frac{1}{2} \rho W^2 (C_\mathrm{l} \mathrm{cos}\phi + C_\mathrm{d} \mathrm{sin}\phi) c \mathrm{d}r, \tag{2.5}$$

where N_b is the number of blades, W is the incident flow speed at the airfoil, C_l and C_d are the airfoil lift and drag coefficients (these values are often obtained experimentally and pulled from an airfoil lookup table based on the airfoil angle of attack), and c is the chord length of the airfoil.

The relative inflow angle of the wind velocity incident on the airfoil (ϕ) can be expressed as a function of the axial and angular induction factors a and $a^{'}$ which generally describe how much the incoming flow is decelerated by the rotor. a and $a^{'}$ are defined as follows:

$$U_0 = (1-a) U_\infty, \tag{2.6}$$

$$V_\theta = 2 a^{'} \Omega r, \tag{2.7}$$

where U_0 is the wind speed directly in front of the rotor and V_θ is the azimuthal component of the flow velocity directly behind the turbine blade. This allows the two sets of equations for the torque and thrust contributions of the rotor annulus to be treated as a system of equations and solved via iteration for the variables a and $a^{'}$. Once solved, the thrust and torque contributions of each annulus can be summed to determine the rotor-wide thrust and torque.

2.2.2 BEMT Correction Methods

A variety of empirical corrections are used to augment this basic BEMT formulation. The corrections explored in this work are briefly described below.

The basic BEMT formulation assumes an infinite number of blades and does not account for vortices shed by the blade tip or by the blade near the hub. A hub and tip loss model attempts to correct for these assumptions. We use the expression formulated by Prandtl [47] as implemented in the AeroDyn theory manual [33].

$$\mathrm{d}Q = 4F_{\mathrm{hub}}F_{\mathrm{tip}}\pi r^3\rho U_\infty\Omega(1-a)a^{'}\mathrm{d}r, \tag{2.8}$$

$$\mathrm{d}T = 4F_{\mathrm{hub}}F_{\mathrm{tip}}\pi r\rho U_\infty^2(1-a)a\mathrm{d}r, \tag{2.9}$$

$$F_{\mathrm{hub}} = \frac{2}{\pi}\cos^{-1}\mathrm{e}^{-\frac{N_\mathrm{b}}{2}\frac{r-R_{\mathrm{hub}}}{r\sin\phi}}, \tag{2.10}$$

$$F_{\mathrm{tip}} = \frac{2}{\pi}\cos^{-1}\mathrm{e}^{-\frac{N_\mathrm{b}}{2}\frac{R-r}{r\sin\phi}}, \tag{2.11}$$

where R is the rotor radius and R_{hub} is the hub radius.

Glauert's correction is used for states in which the induction factor is large (greater than about 0.4). The correction accounts for an increase in thrust for large induction factors where momentum theory nonphysically predicts the thrust to decrease. Here we use a modification of the original Glauert correction [38], which avoids numerical instabilities when combined with the hub-tip loss model described above. This modification was developed by Buhl [48] and is again presented in the Aerodyn theory manual [33]. An empirical expression for the thrust coefficient and axial induction factor is used when the normal BEMT method predicts an axial induction factor over the critical value.

$$C_\mathrm{T} = \frac{8}{9} + \left(4F - \frac{40}{9}\right)a + \left(\frac{50}{9} - 4F\right)a^2, \tag{2.12}$$

and the axial induction factor in these states is then

$$a = \frac{18F - 20 - 3\sqrt{C_\mathrm{T}(50-36F) + 12F(3F-4)}}{36F-50}. \tag{2.13}$$

Dynamic inflow corrections have been developed to account for the non-instantaneous change in wake dynamics behind the rotor as the upstream conditions change. Originally validated for fast blade pitch changes, they have been applied by multiple authors to analyze platform motion [41, 40].

In this work we examine two dynamic inflow corrections, the Stig Øye correction presented in [39], and the Pitt Peters correction presented in [49].

The Stig Øye method replaces the quasi-steady induction factor found through classical BEM at a time t with a new induction factor by passing it through two differential equation filters shown in Equations 2.14 and 2.15.

$$y + \tau_1 \frac{\mathrm{d}y}{\mathrm{d}t} = U_0 + k\tau_1 \frac{\mathrm{d}U_0}{\mathrm{d}t}, \tag{2.14}$$

$$U_{0,\mathrm{adj}} + \tau_2 \frac{\mathrm{d}z}{\mathrm{d}t} = y, \tag{2.15}$$

where k is a constant $= 0.6$, U_0 is the initial induced velocity at the rotor plane, $U_{0,\mathrm{adj}}$ is the final, adjusted induced velocity, and y is an intermediate variable. The two time constants τ_1 and τ_2 are based on the rotor geometry as shown in Equations 2.16 and 2.17.

$$\tau_1 = \frac{1.1}{1 - 1.3a} \frac{R}{U_\infty}, \tag{2.16}$$

$$\tau_2 = \left[0.39 - 0.26 \left(\frac{r}{R}\right)^2\right] \tau_1. \tag{2.17}$$

These filters model the delay between the upstream change in flow conditions and the downstream wake conditions and forces experienced by the rotor. The Øye model stems from a free vortex wake analysis of wind turbine rotor [50, 51] assuming constant uniform circulation, an infinite number of blades, cylindrical wake shape, and a finite tip speed ratio.

The Pitt Peters correction alters the momentum theory thrust equations with an additional added mass term which accounts for the additional inertial thrust required to accelerate the working fluid as the flow changes.

$$\mathrm{d}T = 2\rho U_0 (U_\infty - U_0)\mathrm{d}A + \mathrm{d}M_\mathrm{a} \frac{\mathrm{d}U_0}{\mathrm{d}t}, \tag{2.18}$$

where $\mathrm{d}A$ is the area of the annulus, and $\mathrm{d}M_\mathrm{a}$ is the axial added mass of a solid disk of the working fluid.

$$\mathrm{d}M_\mathrm{a} = \frac{8}{3}\rho(R_2^3 - R_1^3). \tag{2.19}$$

R_1 and R_2 are the outer and inner radii of the annulus, and ρ is the fluid density.

If desired, the BEMT equations can be altered to analyze each turbine blade individually. Single blade modeling allows for the application of different relative velocities across each blade in rotational motion types where the platform induced

velocity experienced by each blade section is a function of azimuthal position as well as annulus. Both the blade element and momentum equations are split to consider a single blade and a third of an annulus, and the system of equations is solved separately for each blade. Equations 2.2, 2.3, 2.4, and 2.5 are altered accordingly:

$$\mathrm{d}Q = \frac{4}{3}\pi r^3 \rho U_\infty \Omega (1-a) a^{'} \mathrm{d}r, \tag{2.20}$$

$$\mathrm{d}T = \frac{4}{3}\pi r \rho U_\infty^2 (1-a) a \mathrm{d}r, \tag{2.21}$$

$$\mathrm{d}Q = \frac{1}{2}\rho W^2 (C_\mathrm{l}\sin\phi - C_\mathrm{d}\cos\phi) c r \mathrm{d}r, \tag{2.22}$$

$$\mathrm{d}T = \frac{1}{2}\rho W^2 (C_\mathrm{l}\cos\phi + C_\mathrm{d}\sin\phi) c \mathrm{d}r. \tag{2.23}$$

To simulate the effect of a prescribed platform motion, the platform, tower, and rotor are assumed to be rigid. Sinusoidal functions prescribing the platform motion in both surge and pitch are selected where A is the motion amplitude and ω is the motion frequency. The derivative of the displacement at the rotor hub caused by that motion (Equations 2.24 and 2.25 where H is the hub height, X_x is the surge motion displacement, and X_θ is the displacement due to pitch motion) is then added to the free stream velocity at each time step as shown in Equation 2.26. Because only the turbine hub velocity due to platform motion is calculated, the BEMT model treats surge and pitch motion the same: as an additional harmonically varying freestream velocity applied evenly across the entire rotor.

$$X_\mathrm{x} = A_\mathrm{x}\cos(\omega_\mathrm{x} t), \tag{2.24}$$

$$X_\theta = H\sin(A_\theta \cos(\omega_\theta t)), \tag{2.25}$$

$$U_{\infty,\mathrm{adj}} = U_\infty * \cos(\theta_\mathrm{avg}) + \frac{\mathrm{d}X_\mathrm{x}}{\mathrm{d}t} + \frac{\mathrm{d}X_\theta}{\mathrm{d}t}. \tag{2.26}$$

The term $\cos(\theta_\mathrm{avg})$ is added to account for the mean platform pitch angle, which occurs in many operating states. The free stream wind velocity is broken into perpendicular and parallel components relative to the tilted rotor plane, and the perpendicular component is taken to be the new free stream velocity.

In order to validate the various BEMT corrections described above, five implementations of the in-house BEMT solver were created. Each implementation includes

Method 1	BEMT
Method 2	BEMT, Single Blade (SB) Modeling
Method 3	BEMT, Hub-Tip Loss (HT) Correction
Method 4	BEMT, HT, Glauert (G) Correction
Method 5	BEMT, HT, G, Stig Øye
Method 6	BEMT, HT, G, Pitt-Peters

Table 2.1: Description of BEMT Methods Tested

additional correction methods. The corrections included in each version of the model are described in Table 2.1.

2.2.3 Quantification of Error

To quantify the discrepancy between the BEMT models being validated and higher fidelity models, we utilize two main error metrics. The first metric is a simple percent difference, which is computed as:

$$\%_{\text{dif}} = 100\left(\frac{x_i - \hat{x}_i}{x_i}\right), \tag{2.27}$$

where x_i is the parameter predicted by the high-fidelity model in a single test case and $\hat{x_i}$ is that same parameter predicted by BEMT.

The second error metric is root mean square error (RMSE) which is defined as follows:

$$RMSE = \sqrt{\frac{1}{n}\sum_{i=1}^{n}\left(\frac{x_i - \hat{x}_i}{x_i}\right)^2}. \tag{2.28}$$

Again, x_i is the parameter predicted by the high-fidelity model in a single test case, $\hat{x_i}$ is that same parameter predicted by BEMT, and n is the total number of test cases that were run.

Percent difference ($\%_{\text{dif}}$) is used to compare BEMT and a higher fidelity model for a single test case, and RMSE is used to compare BEMT and a higher fidelity model for a set of test cases.

2.3 Model Verification

The in-house BEMT code was compared to the widely used BEMT implementation OpenFast [31]. Power, thrust, and torque curves for the IEA 15 MW RWT when simulated with OpenFast and the NREL ROSCO controller are available in the reference

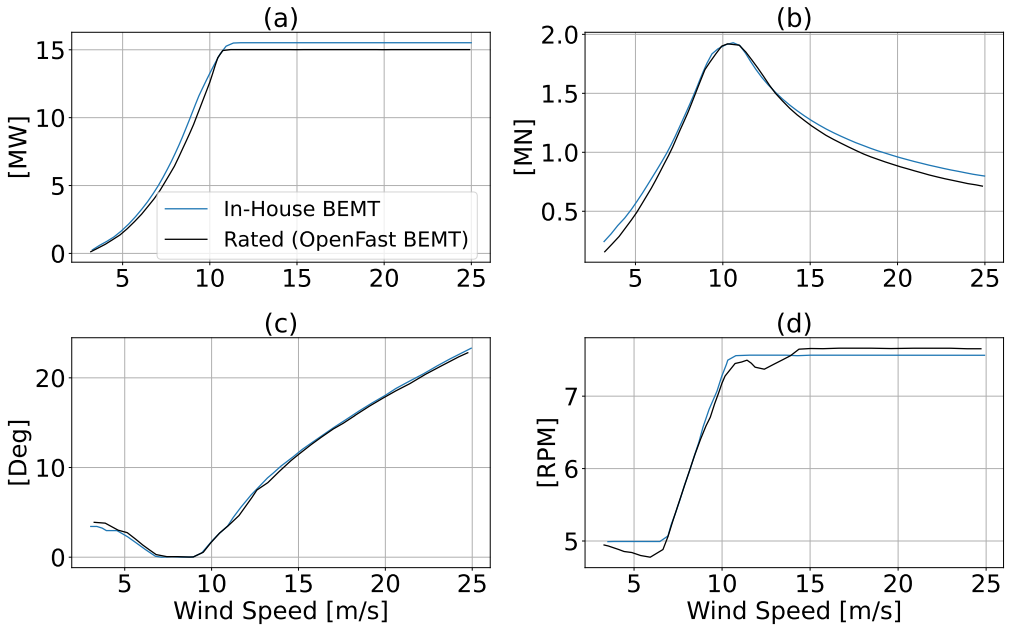

Figure 2.1: Power (a) and thrust (b) curves predicted by in-house BEMT code coupled with ROSCO versus the rated values computed with OpenFast and ROSCO. Blade pitch (c) and rotor speed (d) outputs from the ROSCO controller when coupled with the in-house BEMT versus OpenFast.

wind turbine and control software technical definition documents [52, 53]. Comparisons of the reference curves with an in-house BEMT implementation with Prandtl's and Glauert's corrections are shown in Table 2.2 and Figure 2.1. Figure 2.1 shows dimensional power and thrust, while Table 2.2 compares the power and thrust coefficients predicted by the in-house BEMT model and OpenFast. As shown in Table 2.2, the in-house BEMT solver predicts power and thrust coefficients with less than 4.5 % difference compared to OpenFast at the rated wind speed. The two models are very similar at below rated wind speed, but diverge slightly at high wind speeds. Above the rated wind speed, the in-house solver predicts higher power and thrust than OpenFast. This is due to OpenFast's flexible blade modeling, which decreases predicted power and rotor thrust. For simplicity, and computational efficiency, our model assumes a rigid tower, blade, and drive train. Even at the cut-out wind speed, the discrepancy between the two aerodynamic solvers is less than four percent in power coefficient and less than ten percent in thrust coefficient.

Metric	OpenFast	BEMT	Percent Difference
C_{P}	0.4616	0.4412	4.44%
C_{T}	0.6257	0.6405	2.30%

Table 2.2: In-house BEMT predicted power and thrust coefficients versus values from OpenFast with the ROSCO controller at the turbine rated wind speed.

D	20 m
D_H	3 m
U_D	2.0 m/s
λ_D	5.5
Airfoil	RIS$\varnothing$ A1-24

Table 2.3: Description of Schluntz and Willden Rotor, D is the rotor diameter, D_H is the hub diameter, U_D is the design freestream velocity, and λ_D is the design tip speed ratio.

2.4 Study 1: Comparison to Blade Resolved RANS-CFD for a Tidal Turbine

The first validation study conducted compared the in-house BEMT solver to blade resolved Reynolds averaged Navier-Stokes computational fluid dynamics (RANS-CFD) simulations of a 20 m diameter tidal turbine. Although this work focuses on the effect of platform motion on wind turbines, the physics between FOWTs and floating tidal turbines are largely the same. In addition, the BEMT models required for both tidal and wind turbine modeling are the same, albeit with different fluid densities. With this in mind, this study was used for validation as the data was of good quality and immediately available for our purpose. Simulations were conducted in steady conditions, as well as in surge and pitch type motion. The tidal turbine was originally developed by Schluntz and Willden [54] and modified by Wimshurst and Willden [55]. The primary rotor characteristics are shown in Table 2.3, and the blade geometry and airfoil polars are shown in Figures 2.2 and 2.3.

The BEMT aerodynamic solver with Prandtl's hub-tip loss correction and Glauert's correction (Method 4 from Table 2.1) was first used to simulate steady-state operating conditions at a range of tip speed ratios. The results were compared to blade-resolved RANS-CFD simulations as well as two BEMT simulations with varying turbulent wake methods implemented by Zilic de Arcos [56]. The rotor thrust coefficient and power coefficient predicted by each method are shown in Figure 2.4.

The in-house BEMT implementation exhibits a similar, or better, accuracy, relative to the RANS-CFD results, as the other two BEMT implementations. For predic-

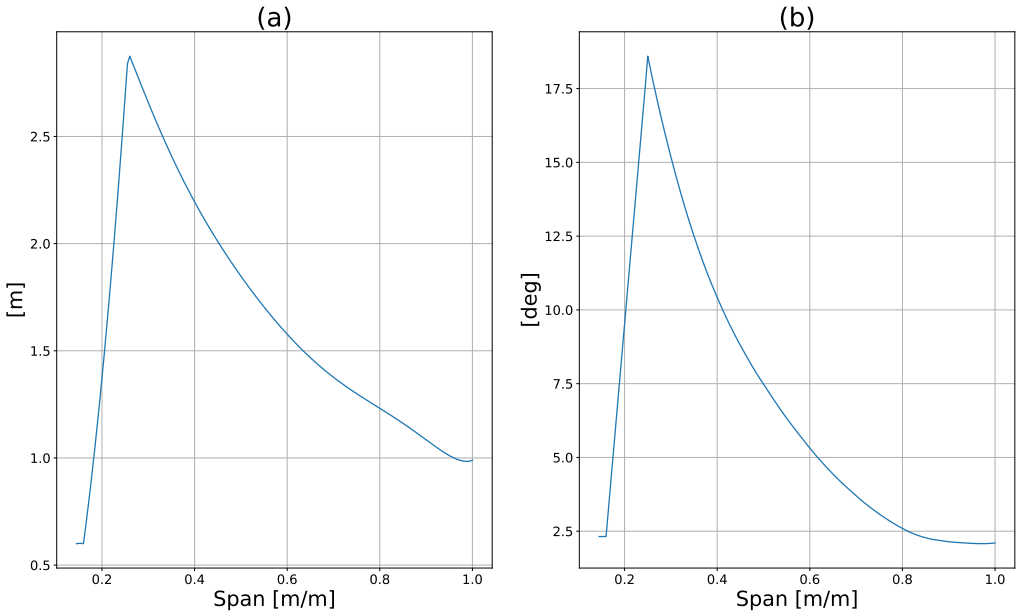

Figure 2.2: Blade chord (a) and twist (b) as functions of non-dimensional span for the Schluntz rotor design.

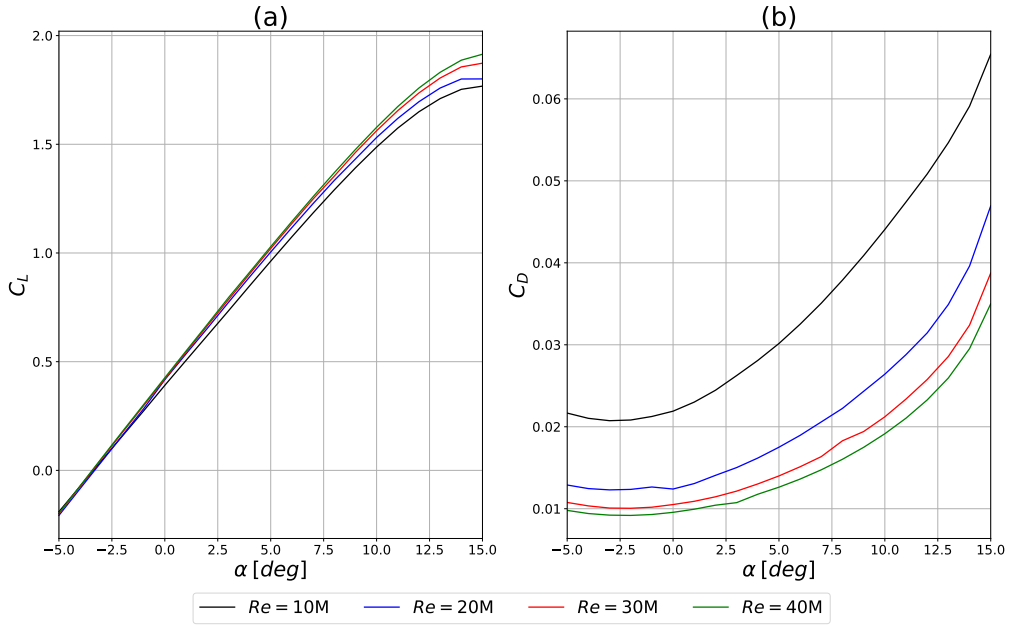

Figure 2.3: Airfoil lift (a) and drag (b) coefficients for the RISØ A1-24 airfoil used in the Schluntz rotor design. Lift and drag coefficients are shown as a function of blade angle of attack for multiple Reynolds numbers.

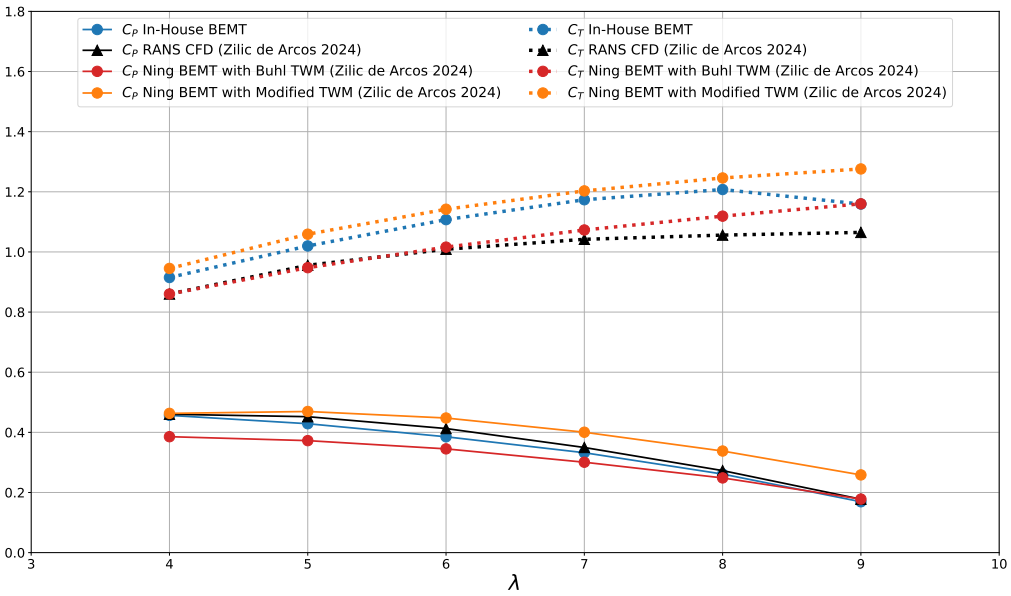

Figure 2.4: Power and thrust coefficients predicted by RANS-CFD, the in-house BEMT solver, a BEMT method with Buhl's turbulent wake model, and with a modified turbulent wake model. Data from RANS-CFD and two BEMT implementations is reproduced from Zilic de Arcos [56].

tion of power coefficient at medium tip speed ratios, the in-house BEMT solver outperforms the other two BEMT methods (4 - 5 % difference to RANS-CFD). However, the in-house BEMT predicts the thrust coefficient less accurately than the modified turbulent wake method from Zilic de Arcos (7 - 14 % difference to RANS-CFD). In general we see reasonable agreement with the higher fidelity RANS-CFD, and similar performance relative to other BEMT models.

The BEMT implementations with various empirical corrections were then compared to blade resolved RANS-CFD simulations of the tidal turbine in surge and pitch type motion conducted by Bin Osman [57]. Ten surge motion cases were studied in which the amplitude and frequency of the platform motion as well as the rotor tip speed ratio were varied. These test cases are described in Table 2.4.

Five implementations of the BEMT aerodynamic solver with varying empirical corrections were used to simulate the same test cases. A time series over one period of platform motion for Cases 2 and 7 is shown in Figure 2.5. For Case 2, a more moderate platform motion, the BEMT implementations achieve good accuracy relative to the RANS-CFD. The implementation with Prandtl's hub tip loss and Glauert's turbulent wake method performs the best relative to the high fidelity model in both C_P and C_T prediction. In general, the BEMT methods accurately model the sinusoidal response

Case	U_∞ [m/s]	A [m]	ω^*	λ
Case 1	2.0	0.25	1.00	4.4
Case 2	2.0	0.5	1.00	4.4
Case 3	2.0	0.75	1.00	4.4
Case 4	2.0	1.0	1.00	4.4
Case 5	2.0	1.0	0.70	4.4
Case 6	2.0	1.0	0.85	4.4
Case 7	2.0	1.0	1.3	4.4
Case 8	2.0	1.0	1.00	4.2
Case 9	2.0	1.0	1.00	4.6
Case 10	2.0	1.0	1.00	4.8

Table 2.4: Description of operating conditions for the ten test cases conducted by Bin Osman [57]. U_∞ is the free stream velocity, A is the amplitude of platform motion, ω^* is motion frequency normalized by the rotor rotational speed, and λ is the tip speed ratio.

of the power and thrust coefficient to the prescribed harmonic motion. However, for the more extreme platform motion in Case 7, the blade resolved RANS-CFD is able to predict non-linear responses due to spanwise flow anomalies that the BEMT is unable to model. In this case, the accuracy of the BEMT model degrades. However, this type of motion is unrealistic for turbine operation (power and thrust coefficient reach zero during the motion cycle).

The various BEMT methods' predictions of the average power and thrust coefficient over a period of platform motion for all ten test cases, as well as the percent difference to that predicted by the RANS-CFD, are shown in Figures 2.6 and 2.7. The predictions for the amplitude of the power and thrust coefficient are shown in Figures 2.8 and 2.9.

There are multiple results at a constant normalized platform induced velocity, as a subset of the test cases only vary the rotor rotational speed, which affects turbine performance but not motion induced velocity. In the prediction of average power and thrust coefficient there is a clear trend between normalized platform induced velocity and error relative to the higher fidelity RANS-CFD. The BEMT implementations with Prandtl's and Glauert's correction, as well as the Stig Øye method perform the best, achieving approximately 3 % RMSE in thrust coefficient prediction and 8 % in power coefficient relative to the RANS-CFD. For prediction of the amplitude of thrust and power coefficient there is not a clear relationship between error and platform induced velocity. The single blade and Prandtl - Glauert implementations perform the best achieving between 4 and 10 % RMSE relative to the RANS-CFD. A discrepancy to

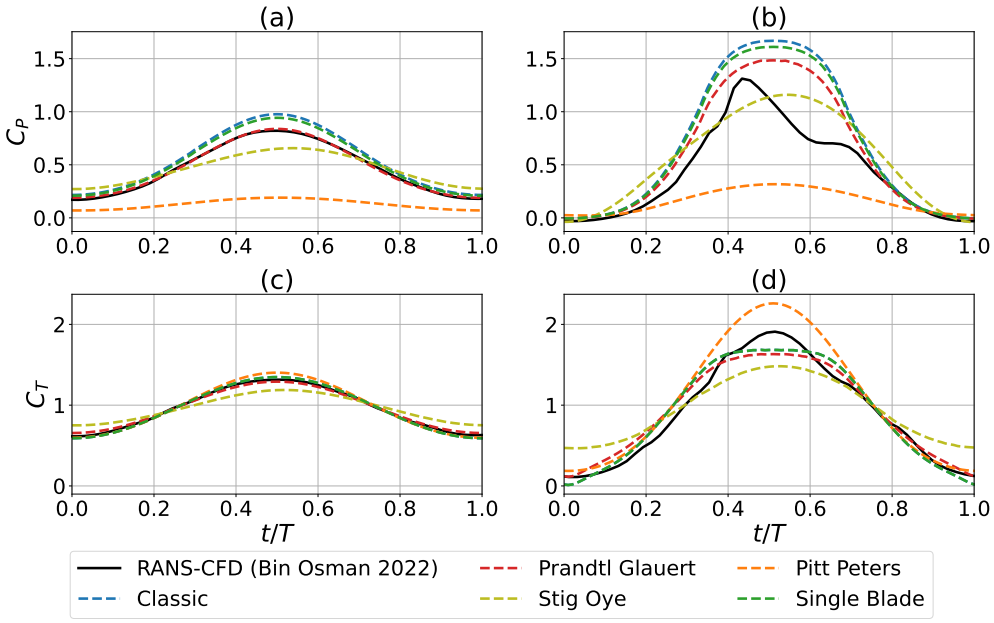

Figure 2.5: Time series of power coefficient (a and b) and thrust coefficient (c and d) over one period of platform motion for surge case 2 (a and c) and case 7 (b and d).

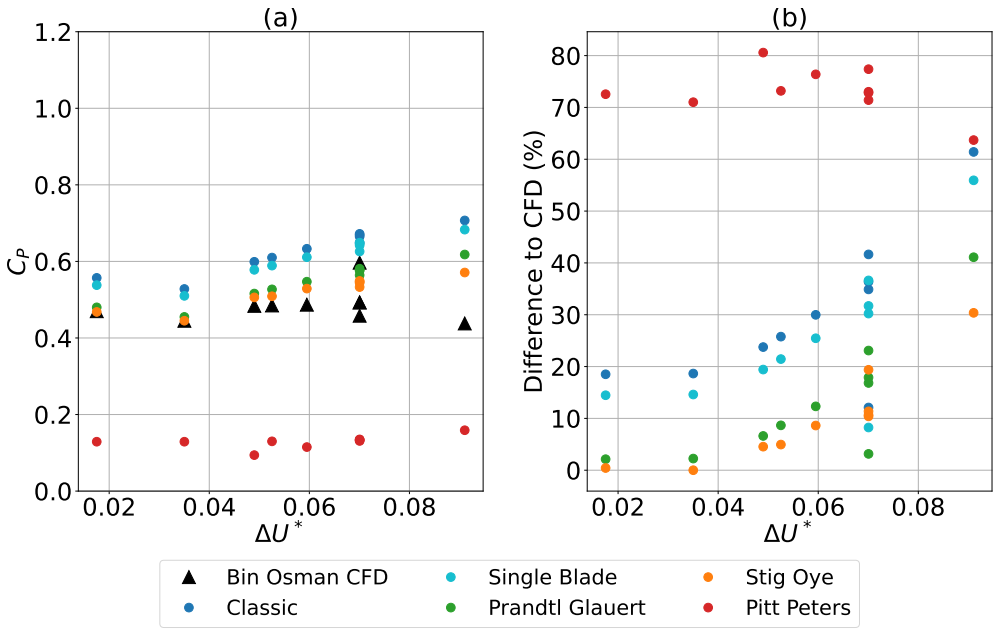

Figure 2.6: The average power coefficient over one period of platform motion predicted by the blade resolved RANS-CFD presented by Bin Osman [57] and by various implementations of the in-house BEMT solver. Results are presented as a function of the platform motion induced velocity normalized by the free stream velocity.

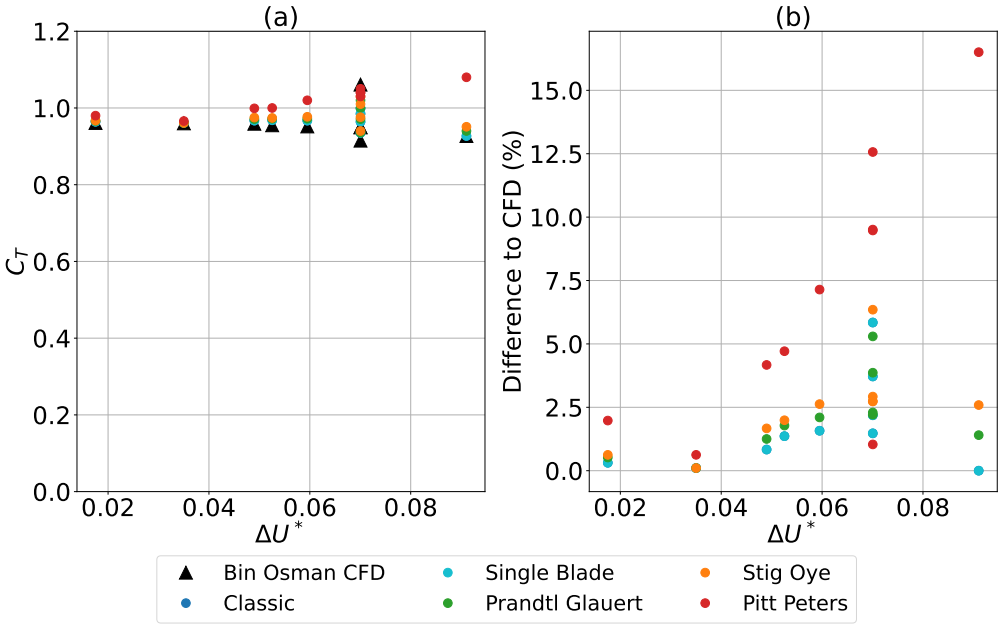

Figure 2.7: The average thrust coefficient over one period of platform motion predicted by the blade resolved RANS-CFD presented by Bin Osman [57] and by various implementations of the in-house BEMT solver. Results are presented as a function of the platform motion induced velocity normalized by the free stream velocity.

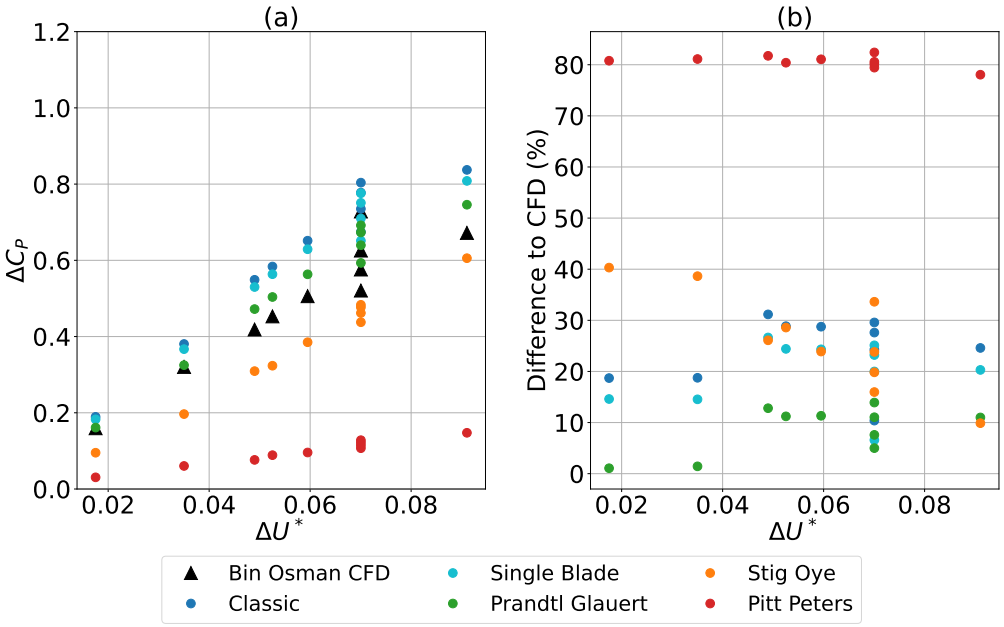

Figure 2.8: The amplitude of the power coefficient over one period of platform motion predicted by the blade resolved RANS-CFD presented by Bin Osman [57] and by various implementations of the in-house BEMT solver. Results are presented as a function of the platform motion induced velocity normalized by the free stream velocity.

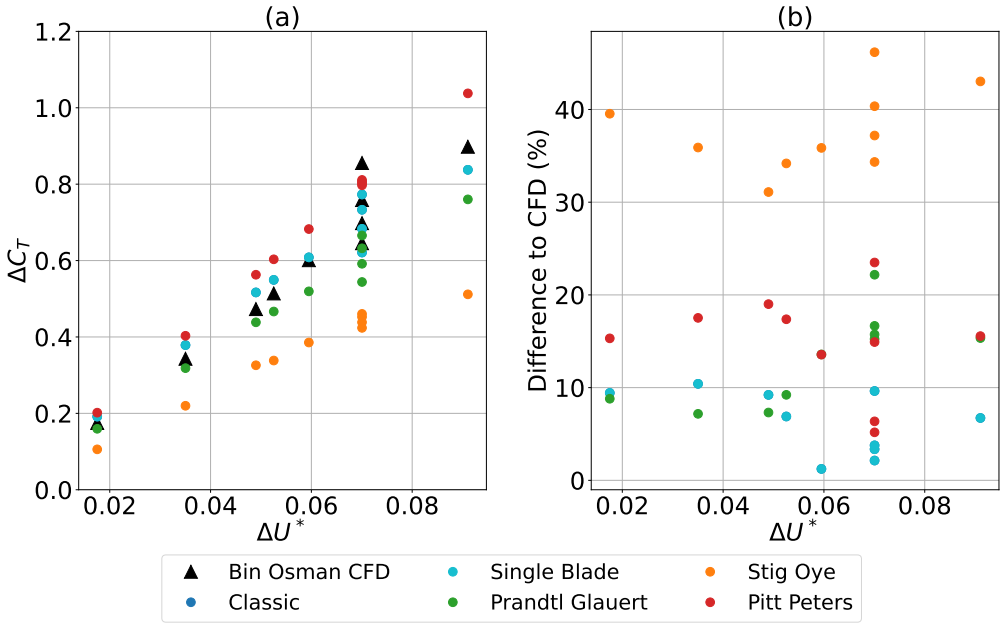

Figure 2.9: The amplitude of the thrust coefficient over one period of platform motion predicted by the blade resolved RANS-CFD presented by Bin Osman [57] and by various implementations of the in-house BEMT solver. Results are presented as a function of the platform motion induced velocity normalized by the free stream velocity.

the higher fidelity model of less than 10 % is considered to be acceptable in this case, given the two orders of magnitude decrease in computational expense granted by the BEMT method. In addition, we see the BEMT method's ability to predict the mean and fluctuating components of power and thrust with an acceptable and similar error for all parameters. This lends confidence to BEMT's ability to be combined with a hydrodynamic flow solver for coupled FOWT analysis.

2.5 Study 2: Comparison to an Experimental Model of the DTU 10 MW Reference Wind Turbine

The prior verification study demonstrated the in-house BEMT solver's ability to accurately predict mean and fluctuating rotor parameters compared to RANS-CFD. However, we would like to further confirm that BEMT can accurately model the fluctuating components of rotor thrust and torque, as these parameters will have important implications for a fully coupled aero-hydrodynamic model.

The next validation study consisted of a comparison to an experimental model designed to replicate the rotor thrust characteristics of the DTU 10 MW reference

Parameter	DTU 10 MW RWT	Scale Model
D	178.3 m	1.2 m
D_H	5.60 m	0.10 m
U_D	11.40 m/s	3.80 m/s
λ_D	7.5	7.5
Airfoil	Multiple Airfoils - FFA W3 Series	SD7032

Table 2.5: Description of the Taruffi et al. [59] rotor design as well as the full - scale DTU 10 MW RWT [61], D is the rotor diameter, D_H is the hub diameter, U_D is the design freestream velocity, and λ_D is the design tip speed ratio.

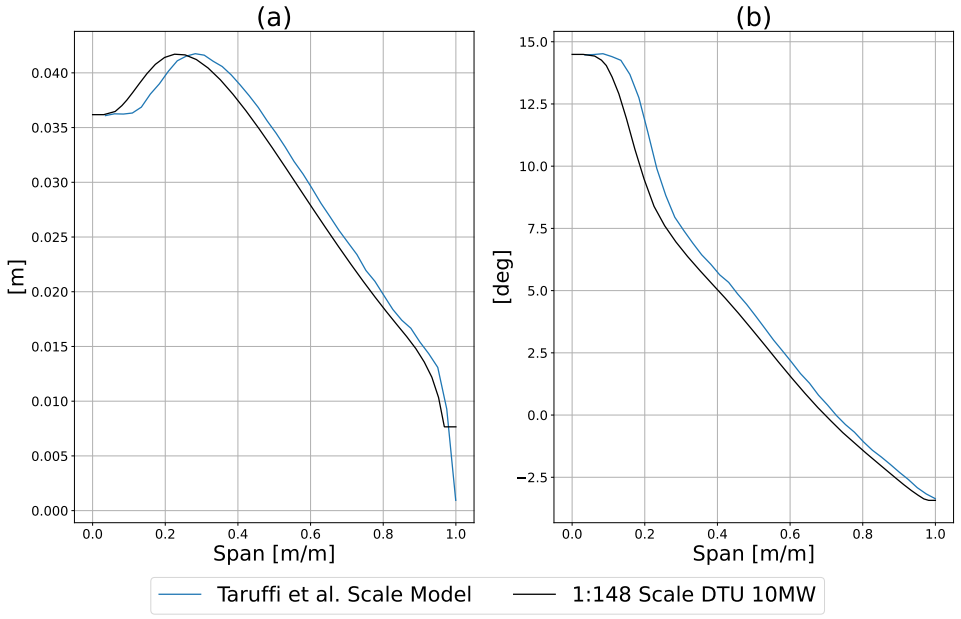

Figure 2.10: Blade chord (a) and twist (b) as functions of non-dimensional span for the Taruffi et al. [59] rotor design as well as geometrically scaled values for the DTU 10 MW RWT [61].

wind turbine (RWT) designed by Bak et al. [58]. The experimental results were obtained from a 1:148 scale model designed by Taruffi et al. [59] utilizing an airfoil design presented in Fontanella et al. 2023 [60]. The scale turbine was operated in a wind tunnel while the turbine base was mechanically actuated to simulate platform motion. The primary rotor characteristics of the Taruffi et al. turbine are shown in Table 2.5, and the blade geometry and airfoil polars are shown in Figures 2.10 and 2.11.

It is noteworthy that the blade geometry of the Taruffi et al. turbine is not geometrically scaled from the full DTU 10 MW RWT geometry. Additionally, the airfoil utilized in the experimental model is different from those used in the full scale

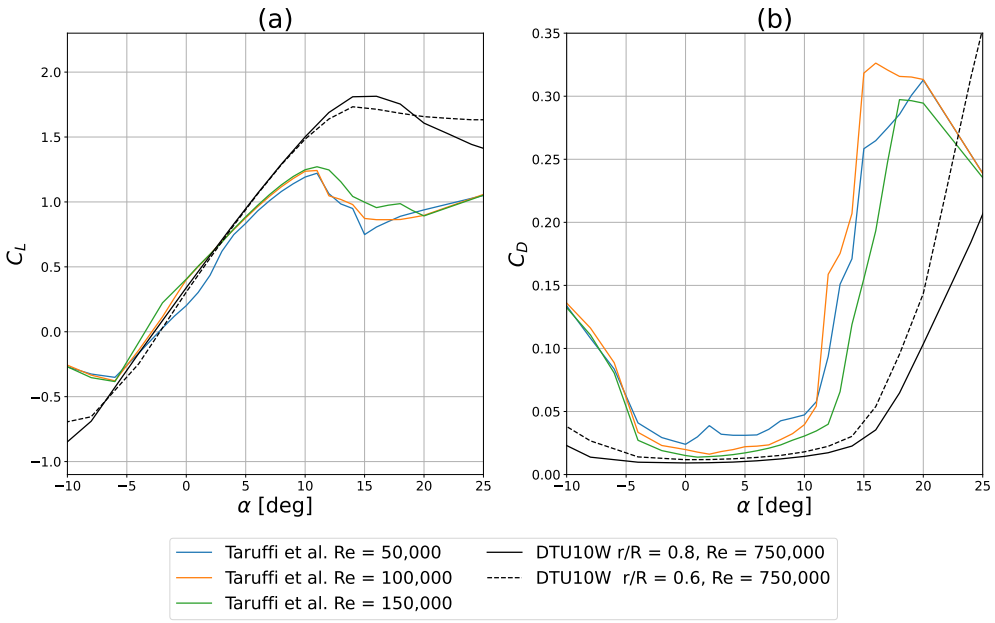

Figure 2.11: Airfoil lift (a) and drag (b) coefficients for the SD7032 airfoil used in the Taruffi et al. [59] rotor design as well as for the full scale DTU 10 MW RWT [61] blade. Lift and drag coefficients are shown as a function of blade angle of attack for multiple Reynolds numbers. For the DTU 10 MW RWT the airfoil shape changes along the blade span, so lift and drag coefficients are shown at two points along the span.

turbine. As such, the lift and drag coefficients between the experimental and full scale blades are not the same. The Taruffi et al. model is performance scaled, and the experiment does not aim to match Reynolds numbers between the experimental and full scale blades. The experimental blade geometry is instead tuned to preserve the rotor thrust coefficient from the full scale turbine for a wind speed reduction factor of three. In order to both assess the accuracy of our BEMT method and the implications of this performance scaling methodology, we compare the experimental results with BEMT simulation of the experimental blade geometry and scaled down flow speed, as well as with BEMT simulation of the full scale blade geometry with the full scale flow speed.

We first compare the BEMT method to the experimental model for steady state operation with no platform motion. The results from the Taruffi et al. experimental model for five wind speeds up to the rated wind speed are compared with results from OpenFast Generalized Dynamic Wake (GDW) Model analyzing the experimental geometry, the in-house BEMT analyzing the experimental geometry, the in-house BEMT analyzing the full scale geometry, and the reference curve for the DTU 10 MW RWT computed with the HAWC2 BEMT software in Figure 2.12.

The Taruffi experimental results and all of the numeric models are clustered tightly and agree with the reference curve for the prediction of turbine thrust at each wind speed. This result is expected considering the experimental model was specifically tuned to match rotor thrust with the full scale geometry. However, when looking at power prediction we see a large spread between the models. The in-house BEMT implementations analyzing the full scale geometry match the reference curve. This result is expected given that the reference curve is also found by running a BEMT analysis of the full scale geometry. The experimental model generates significantly less power than the reference curve would predict (10 - 30 % of the reference value). This is likely due to the decreased airfoil efficiency ($\frac{C_L}{C_D}$) of the experimental model compared to the full scale. This is roughly captured by the in-house BEMT analyzing the experimental geometry which shows a decrease in power production compared to the full scale geometry. However, the discrepancy of the in-house BEMT model's prediction of power relative to the experimental results is significant (up to 100 % difference) and increases with increasing wind speed. The discrepancy between the BEMT and the experimental results in this low airfoil efficiency and low Reynolds number flow regime is likely due to increased drag effects and transitions between laminar and turbulent flow. The FAST GDW model performs slightly better relative to the experimental results. However, the GDW model still predicts a negative power

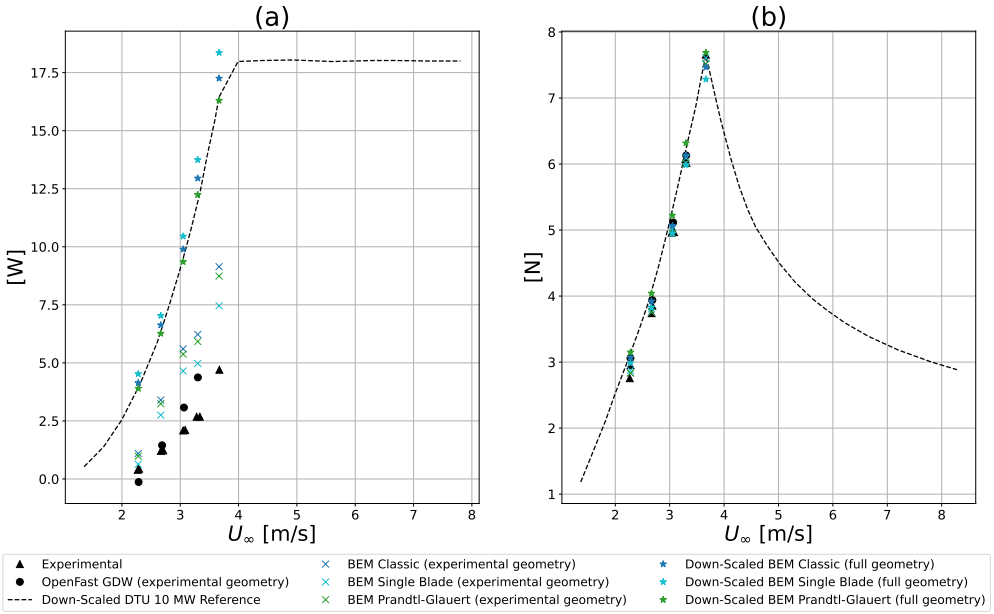

Figure 2.12: The power (a) and thrust (b) curves for the DTU 10 MW RWT [61] with results from the Taruffi et al. [59] experimental model, OpenFast Generalized Dynamic Wake (GDW) model, and three implementations of the in-house BEMT method analyzing both the experimental and full scale turbine geometry. Reslults analyzing the full scale geometry and the DTU 10 MW reference curves have been down scaled to match the experimental scale power and thrust.

Case	U [m/s]	A [mm]	ω [Hz]	Ω [rpm]
Case 1	4.0	47.7	1.0	480
Case 2	4.0	23.9	2.0	480
Case 3	4.0	15.9	3.0	480
Case 4	4.0	13.6	3.5	480
Case 5	4.0	11.9	4.0	480
Case 6	4.0	10.6	4.5	480
Case 7	4.0	9.5	5.0	480

Table 2.6: Description of operating conditions for the seven test cases conducted by Taruffi et al. [59] U is the free stream velocity, A is the amplitude of platform motion, ω is motion frequency, and Ω is the rotor rotational speed.

output above the cut-in wind speed, and has large discrepancies to the experimental results at the 3.5 m/s wind speed case.

In addition to the steady state results, we compare the variation in thrust predicted by BEMT to the Taruffi et al. experimental model for seven surge type motion cases. The details of the motion cases analyzed are shown in Table 2.6. Throughout these cases, the maximum velocity due to platform motion (ΔU) is kept constant. The amplitude of rotor thrust coefficient for each case as predicted by the various BEMT implementations and by the experimental model is shown in Figure 2.13. The amplitude of thrust coefficient is normalized by the rated value, and frequency is represented as rotor reduced frequency where $f_r = \frac{fR}{U_\infty}$.

The steady BEMT implementations (classical, single blade, and Prandtl's and Glauert's correction) do not exhibit a frequency dependence, so predict the same thrust fluctuation for all cases where the normalized platform induced velocity is constant. The Stig Øye method does exhibit frequency dependence. However, for this range of frequencies and rotor geometry, the variation is very minor (magnitude of $10^{-3}\, C_T$). In contrast, the Pitt Peters method displays a strong frequency dependence. However, the accuracy of the Pitt Peters method relative to the experimental results is very poor for reduced frequencies between 0.6 and 1.3. The other BEMT methods are relatively tightly grouped, ranging from 10 to 31 absolute percent difference to the experimental results.

Fontanella et al. 2021 [44] determined through experimental testing that the airfoil utilized in this campaign would begin to experience unsteady local flow characteristics in surge motion with rotor reduced frequency greater than one half. Importantly, we see the best accuracy of the BEMT methods below this limit (5.5 to 11 % difference to experimental results). The range of frequencies tested here is significantly above the natural frequencies of representative floating platforms (The UMaine Volturnus

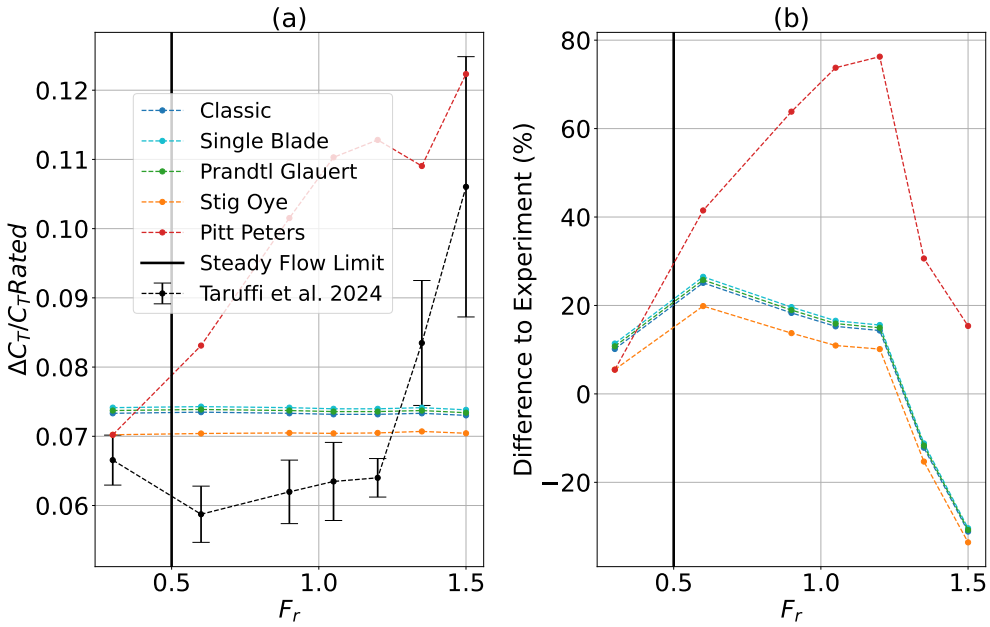

Figure 2.13: Normalized amplitude of thrust coefficient over a single period of platform motion as a function of rotor reduced frequency (a) and the percent difference of the BEMT methods relative to the experimental results (b).

floater has a natural frequency of 0.007 Hz in surge [62]). Motion at this natural frequency would result in a reduced frequency of 0.08. Motion at a representative wave frequency of 0.1 Hz would result in a reduced frequency of roughly 1. The discrepancy between the BEMT and experimental models is smaller for reduced frequencies below 1.25 than above 1.25. Motion at wave or platform natural frequencies will result in reduced frequencies equal to or less than 1.25: the region in which BEMT error is smaller. Across all test cases, the absolute root mean square error is 18.4 % for the implementation with Prandtl and Glauert's corrections.

Additionally, we compare the results shown in Figure 2.13 to the predictions of the BEMT model analyzing the full scale DTU 10 MW geometry. The normalized amplitude of thrust coefficient predicted for both geometries and the experimental results are shown in Figure 2.14. The Stig Øye method analysis of the full scale geometry exhibits a stronger frequency dependence than the experimental scale geometry. This is due to the tuning of the Stig Øye time constants based on the blade radius. The larger rotor causes a larger value of the first time constant, resulting in larger thrust fluctuations.

We see that for all BEMT implementations the fluctuation of thrust predicted for the full scale geometry is significantly different than that predicted for the experimental scale geometry. In addition, for all implementations except for Prandtl's and

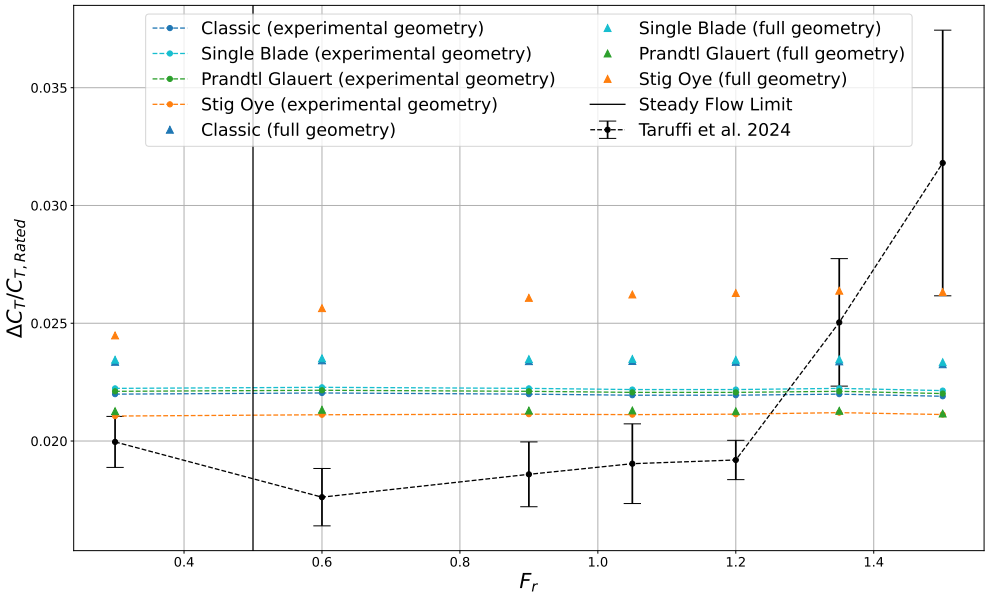

Figure 2.14: The normalized amplitude of thrust coefficient predicted by BEMT for the full scale DTU 10 MW RWT [61] geometry and the Taruffi et al. [59] experimental geometry versus the experimental results. The full scale geometry results are down scaled to match the other two datasets.

Glauert's corrections, the thrust fluctuation predicted by BEMT for the full scale turbine has greater discrepancy to the experimental results. This result suggests that while experimental performance scaling to preserve a single parameter, like thrust coefficient in steady conditions, will create a turbine that accurately reproduces that parameter, there is no guarantee of that performance scaled geometry accurately reproducing any other parameter. In this case, a turbine specifically tuned to preserve thrust coefficient at steady state may not accurately recreate the fluctuation of thrust in a prescribed motion case. However, it is necessary to consider that BEMT is an imperfect tool, especially in dynamic cases. As such, further exploration using higher fidelity simulation tools may be required to definitively quantify the accuracy of experimental performance scaling methodologies.

2.6 Study 3: Comparison to an Experimental Model of the IEA 15 MW Reference Wind Turbine

A final validation study was conducted comparing the BEMT implementations to an additional experimental model. Fontanella et al. [63] conducted wind tunnel testing of a 1:100 scale model of the IEA 15 MW RWT [52] using a similar performance

Parameter	IEA 15 MW RWT	Scale Model
D	240 m	2.4 m
D_H	7.94 m	0.18 m
U_D	10.59 m/s	3.53 m/s
λ_D	9	9
Airfoil	Multiple Airfoils - FFA W3 Series	SD7032

Table 2.7: Description of the Fontanella et al. [63] rotor design as well as the full - scale IEA 15 MW RWT [52], D is the rotor diameter, D_H is the hub diameter, U_D is the design freestream velocity, and λ_D is the design tip speed ratio.

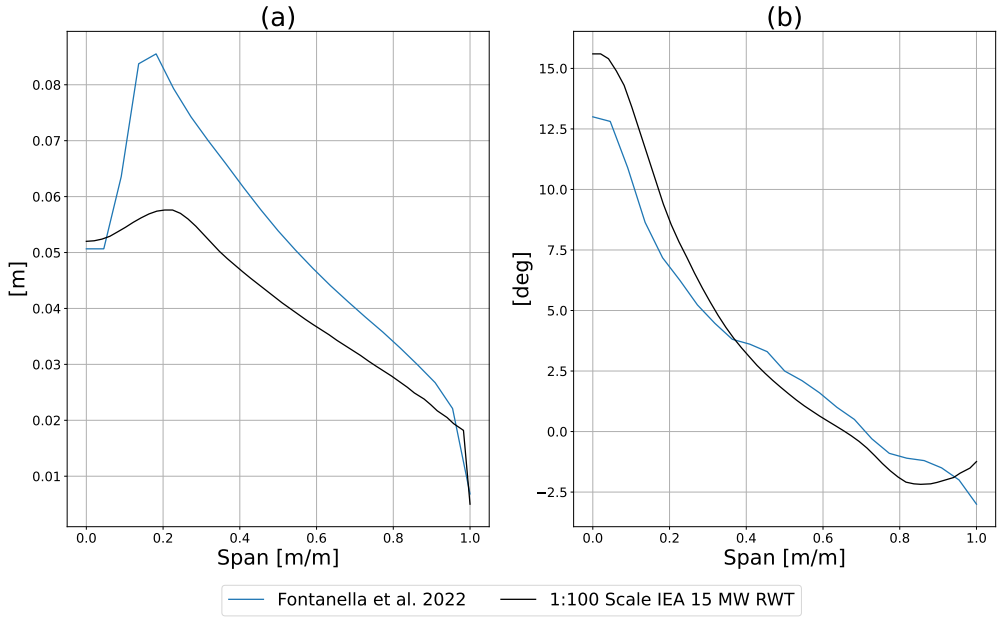

Figure 2.15: Blade chord (a) and twist (b) as functions of non-dimensional span for the Fontanella et al. [63] rotor design as well as geometrically scaled values for the IEA 15 MW RWT [52].

scaling methodology as Taruffi et al. [59]. In this case, the blade geometry was tuned to preserve the span-wise lift distribution for a wind speed reduction factor of three. The experimental model was then operated while actuators at its base prescribed platform motion in each of its six degrees of freedom individually. The primary rotor characteristics of the Fontanella et al. turbine are shown in Table 2.7, and the blade geometry and airfoil polars are shown in Figures 2.15 and 2.16.

Here we compare the BEMT prediction of power and thrust amplitude to the five cases in surge-type motion analyzed by Fontanella et al. The five cases are described in Table 2.8.

In each case, the rotor aerodynamic torque and thrust are measured via force

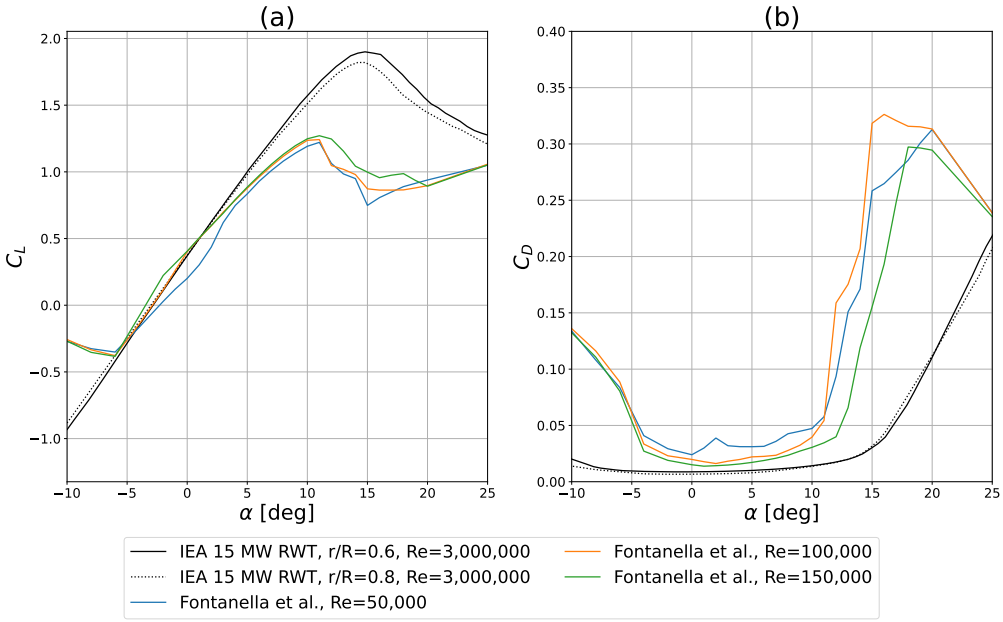

Figure 2.16: Airfoil lift (a) and drag (b) coefficients for the SD7032 airfoil used in the Fontanella et al. [63] rotor design as well as for the full scale IEA 15 MW RWT [52] blade. Lift and drag coefficients are shown as a function of blade angle of attack for multiple Reynolds numbers. For the IEA 15 MW RWT the airfoil shape changes along the blade span, so the lift and drag coefficients are shown at two points along the span.

Case	U [m/s]	A [m]	ω [Hz]	λ
Case 1	2.95	0.060	0.350	9.0
Case 2	2.95	0.114	0.175	9.0
Case 3	2.95	0.006	3.175	9.0
Case 4	5.00	0.114	0.350	9.0
Case 5	5.00	0.013	3.175	9.0

Table 2.8: Description of operating conditions for the five test cases conducted by Fontanella et al. [63] U is the free stream velocity, A is the amplitude of platform motion, ω is motion frequency, and λ is the tip speed ratio.

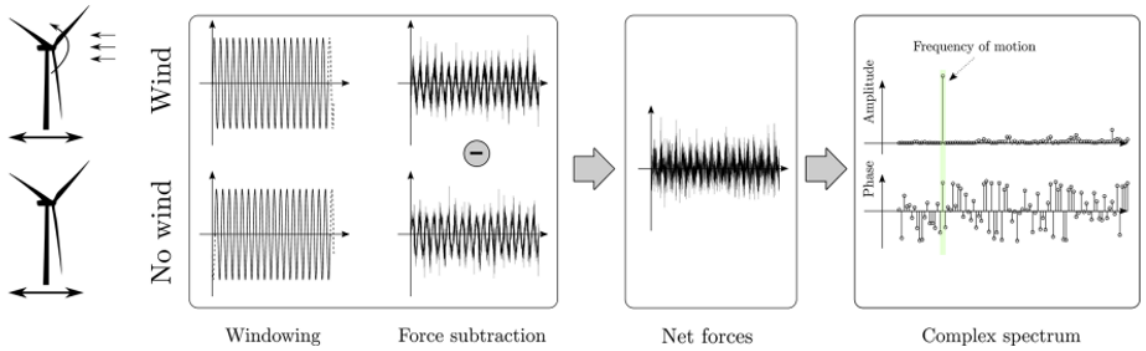

Figure 2.17: Diagram describing data processing to determine the thrust and torque amplitude for each test case reproduced from Fontanella et al. [63].

gauges at the rotor hub during the same platform motion, both with and without the wind tunnel active. The forces measured during the platform motion without wind are denoted the inertial forces and subtracted from the time series with the wind tunnel active. The resultant time series of thrust and torque is then the aerodynamic force. These time series are treated via fast Fourier transform (FFT) and plotted as the magnitude of the aerodynamic response as a function of frequency. The magnitude at the prescribed platform motion frequency is taken to be the torque and thrust amplitude of the turbine. This process is described in Fontanella et al. 2022 [63], as well as illustrated in Figure 2.17 from that publication.

Using raw data obtained from the authors, we obtained the torque and thrust amplitude in each test case, with good agreement to the published data. An example time series and associated frequency domain FFT from Case 3 is shown in Figure 2.18.

With the turbine aerodynamic torque and thrust response obtained, we are able to compare the experimental results to those predicted by BEMT. The amplitude of the power and thrust for the experimental turbine as a function of the maximum platform induced velocity normalized by the free stream velocity is shown in Figure 2.19.

The BEMT methods agree fairly well with the experimental results for the three cases with lower normalized platform induced velocity (2 to 24 % difference to the experimental results for the steady BEMT methods in thrust amplitude). However, for large platform induced velocities, the BEMT method's accuracy relative to the experimental results is much worse (19 to 58 % difference for the steady BEMT methods in thrust amplitude).

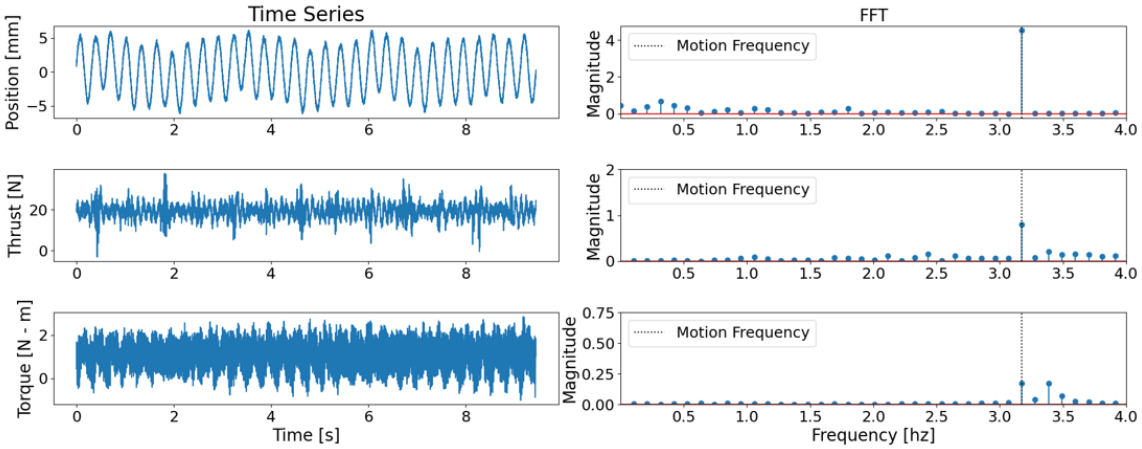

Figure 2.18: Time series (left), and frequency domain representation obtained via FFT (right) for Case 3.

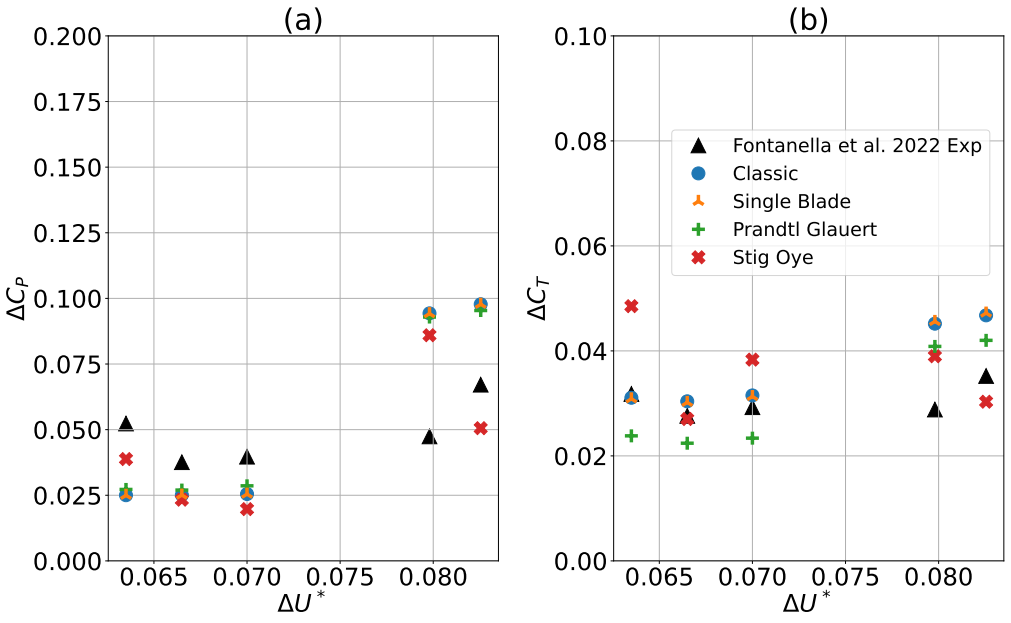

Figure 2.19: The amplitude of power (a) and thrust (b) coefficients as a function of normalized platform induced velocity for five test cases in surge motion.

For these high normalized platform induced velocities cases, the steady BEMT methods generally overpredict the experimental results. It is possible that this is due to the magnitude of the aerodynamic response from the experimental data being taken only at the excitation frequency. The actual response may leak into frequencies slightly smaller or larger than the excitation frequency, and thus the measured experimental result may be an underprediction. This can be seen in Figure 2.18, where the magnitude of the torque response at the motion frequency is equal to the magnitude at a slightly higher frequency. Additionally, we have shown that our BEMT model only matches results from experimental performance scaling for the variable that the blade geometry has been scaled to preserve. As such, the true accuracy of the experimental model's prediction of the fluctuation of power and thrust is unclear. It is important to note that the BEMT model used here is low-fidelity. As such, it is hard to make a definite conclusion about the use of experimental performance scaling. These results illustrate a possible downside to the method and comparison of these results to high-fidelity simulation, or full-scale experimental results, is recommended for future work.

2.7 Discussion and Conclusions

In order to quantify the accuracy of the BEMT method, we compute the RMSE of each parameter studied in the three validation studies for each BEMT implementation relative to the higher fidelity model. The results are shown in Table 2.9. The Pitt Peters method was not examined in validation Study 3 due to its large error in the prior two studies. Additionally, the large error in the fluctuation of power coefficient in validation Study 3 is likely due to issues in the frequency domain data processing described in the prior section. Overall, we see a range in BEMT discrepancy to higher fidelity models between 3 and 27 %.

Comparing the various BEMT implementations to each other, we see that for the prediction of the mean power and thrust coefficients the Prandtl-Glauert and the Stig Øye implementation perform the best with under 10 % RMSE. However, for the amplitude of power and thrust coefficient the addition of the Stig Øye model decreases the prediction accuracy for three of the five comparisons (ΔC_{P} Study 1, ΔC_{T} Study 1, and ΔC_{T} Study 3). The added efficacy offered by the Stig Øye model is thus uncertain. The other dynamic inflow model, the Pitt Peters method, vastly underperforms all of the other implementations.

Study	Parameter	Classic	Single Blade	Prandtl-Glauert	Stig Øye	Pitt Peters
1	C_P	14.8	12.9	8.19	6.80	36.1
1	C_T	2.78	2.78	2.89	3.18	7.83
1	ΔC_P	12.0	9.89	4.41	12.0	40.0
1	ΔC_T	3.18	3.17	8.66	23.0	8.30
2	ΔC_T	18.1	18.7	18.4	15.6	43.8
3	ΔC_P	53.1	53.1	48.4	44.0	N/A
3	ΔC_T	21.9	22.2	25.0	27.0	N/A

Table 2.9: Root mean square error, expressed as percentage, for each BEMT implementation relative to a higher fidelity model.

The poor performance of the dynamic inflow models relative to the steady BEMT methods is likely due to a fundamental difference between platform motion and the case studies these dynamic models were derived under. The Stig Øye method was validated for instantaneous changes in blade pitch or rotor speed after which the rotor was allowed to return to steady state [64, 65]. The Pitt Peters method was derived as an approximation of an instantaneous change in thrust coefficient at the rotor plane [49]. The Stig Øye and Pitt Peters methods were derived to account for instantaneous changes in induced velocity and variations in rotor axial force due to these changes. However, Snel and Schepers [66] show through experimental wind tunnel results that although the induction factor a changes with variations in free stream velocity (this fact is clear from the formulation of the induction factor shown in Equation 2.6, as a is normalized by U_∞), the induced velocity (U_0) is relatively unaffected. Dynamic inflow models were developed to account for instantaneous changes in the induced velocity U_0 and validated in experiments where U_0 was varied via blade pitch. However, low frequency, harmonic, platform motion can be thought of as a change in the free stream velocity U_∞. As such, the underlying mechanisms in dynamic inflow effects that are modeled by methods such as Øye and Pitt Peters are fundamentally different from the dynamics caused by low frequency platform motion.

These observations lead to the conclusion that there is no clear theoretical indication that dynamic inflow methods could improve the accuracy of quasi-steady BEMT methods for the case of harmonic platform motion. This is supported by the data presented here, which indicates that the benefit in accuracy from dynamic inflow modeling is uncertain. These findings are in line with the results of Papi et al. [45] and Bergua et al. [43] who find that dynamic corrections for BEMT do not increase accuracy relative to higher fidelity models for cases that do not include oscillations of blade pitch and rotor speed.

In addition to the comparison between BEMT methods, we are able to characterize the effective range of BEMT analysis based on motion frequency or platform motion induced velocity. From Section 2.5, we see a clear indication that the steady flow limit of $f_r = 0.5$ proposed by Fontanella et al. [44], does demarcate a significant decrease in BEMT accuracy relative to the experimental model. As expected, BEMT is less accurate in unsteady flow conditions. This suggests that local airfoil testing of the airfoils used in full scale turbines could be used to determine a steady flow frequency limit, under which steady BEMT can be accurately applied.

The applicability of BEMT can also be determined through the normalized platform induced velocity. As seen in both Sections 2.4 and 2.6, the accuracy of the BEMT Method 4, with Prandtl's and Glauert's corrections, decreases as ΔU^* increases. In Study 1 for a $\Delta U^* < 0.07$, the percent difference was under 10 % for ΔC_T, 12 % for ΔC_P, 5 % for C_T, and 20 % for C_P. In Study 3, the BEMT accuracy also deteriorates for $\Delta U^* > 0.07$. A limit of $\Delta U^* = 0.07$ would correspond to a 0.7 Hz motion at 1 m amplitude or a 0.07 Hz motion at 10 m amplitude for rated wind speeds. This range of motion types includes much of the range of surge motion expected in operational conditions. In addition, these validation results indicate very good accuracy in thrust and amplitude of thrust prediction, which will lead to better modeling of the induced motion of the coupled turbine, platform system.

Chapter 3

Rotor Response to Prescribed Harmonic Platform Motion

3.1 Introduction

The effect of platform motion on FOWT aerodynamics is of primary interest, as it will determine the efficacy of FOWT installations. It will also inform any variations in design between floating and fixed turbines. It is desirable to use the types of aerodynamic solvers discussed previously to predict turbine performance during rotor motion. However, as mentioned in Chapter 1, fully coupled aero-hydrodynamic models are more computationally expensive than exclusively aerodynamic models. Thus, for an initial analysis, it is common to forgo any hydrodynamic modeling, and prescribe a platform motion to the system. Typically, platform motion is approximated with a prescribed, simple harmonic oscillation.

To determine appropriate frequencies of prescribed motion for our initial analysis of turbine performance, we turn to explorations of FOWT motion response with fully coupled models. Mahfouz et al. [28] utilized NREL's OpenFast to simulate the IEA 15-MW RWT on CoreWind, WindCrete, and Activefloat platforms with OpenFast. The potential flow solver ANSYS AQWA was used to compute the frequency domain added mass and radiation damping matrices for the platforms. OpenFast then used the Cummins sea-keeping equation, the BEMT solver Aerodyn, and the mooring line model Moordyn to simulate the coupled aerodynamic - hydrodynamic system. Their results predicted significant motion responses at the wave frequency, as well as a lesser but noticeable response at the relevant natural frequency for the platform motion type under regular wave loading. Irregular wave and wind loading resulted in a large low frequency motion response near the platform's natural frequency in pitch and surge type motion. These results, and similar findings from an experimental

coupled model conducted by Ransley et al. [67], suggest that motion is most likely to occur at incoming wave frequencies, or at platform natural frequencies. As such, these frequencies are often targeted in prescribed motion studies.

The study of platform motion effects can be simplified by considering motion in a single degree of freedom. Of these, pitch and surge type motion are often considered especially important as they directly impact the relative inflow velocity at the rotor. Tran and Kim [24] utilized a BEMT algorithm with dynamic inflow correction that tracks individual blade position to determine the relative velocity oscillation for each blade in platform pitch motion. For pitch motion frequencies of 0.03 Hz and 0.05 Hz with a four degree amplitude, their model predicted a variation of power coefficient between 0.34 and 0.72 and between 0.28 and 0.78 respectively. For 0.1 Hz frequency, the power coefficient varied between 0.18 and 0.96.

As mentioned in Chapter 2, De Vaal and Moen [25] utilized BEMT with various dynamic inflow models to analyze power performance of the NREL 5 MW reference turbine during platform surge motion. For surge cases of 8 meter amplitude and varying frequency between 0.02 Hz and 0.123 Hz (representing a platform natural frequency and a typical ocean wave frequency), the authors' model predicted that the turbine thrust coefficient could vary by 0.15 for the lowest frequency and 0.85 for the highest.

Cottura and Caradonna [26] reported that in pitch motion at low wind speeds, average power output over an oscillation can be found to increase due to the cubic relation between wind speed and power. Their steady BEMT model predicted power output increases of up to 12 percent for the NREL 5 MW reference turbine experiencing platform pitch motion of 2.5-degree amplitude and 0.05 Hz frequency. This phenomenon does not apply at wind speeds near the turbine rated speed, where the "high power" portion of the oscillation would result in above rated power, which is capped by the turbine control system. In this regime, power output can decrease by up to 10 percent for the same platform oscillation.

We aim to utilize the prescribed harmonic motion methodology with our in-house BEMT method to predict FOWT performance for a large scale wind turbine representative of future FOWT installations. Specifically, we will do so over a wide range of wind speeds in order to generate a motion-adjusted power and thrust curve. Turbine power curves are frequently combined with measures of the site-specific wind resource to estimate turbine power production at a prospective installation site [68, 69]. However, this method of predicting long-term power production does not take into account

the effect of platform motion on turbine performance. We present these adjusted performance curves as a means to estimate performance during the types of platform motion most likely to occur, namely at wave or platform natural frequencies. At the time of writing, motion-adjusted power and thrust performance curves for a turbine over 10 MW rating do not exist in the literature.

3.2 Methods

To characterize the response of a representative floating wind turbine to a prescribed platform motion, we utilize the aerodynamic BEMT model presented in Chapter 2. Based on the validation results presented, we include Prandtl's hub and tip loss correction [37] and Glauert's turbulent wake method [38], but do not include either of the dynamic inflow corrections. Additionally, we do not include single blade modeling given the minimal benefit to accuracy and the increase in computational expense discussed in the previous section.

We examine the response of the IEA 15 MW Reference Wind Turbine presented by Gaertner et al. [52]. The turbine has a 240 m diameter, 150 m hub height, direct drive generator, and is designed to be representative of large-scale, offshore turbines which are likely to be installed in future offshore wind developments. The key characteristics of the IEA 15 MW RWT are discussed in more detail in Chapter 2 Section 2.6. Additionally, blade polars, geometry, and other reference materials for the turbine can be found in the open-source GitHub repository maintained by NREL [52].

We utilize the Reference Open Source Controller (ROSCO) presented by Abbas et al. [53]. ROSCO consists of a below-rated generator torque controller and an above-rated collective blade pitch controller. Both the above and below-rated modules are proportional-integral (PI) reference tracking controllers with the general form

$$y = k_{\mathrm{p}} u + k_{\mathrm{i}} \int_0^T u dt, \tag{3.1}$$

where y is the controller output, k_{p} and k_{i} are scheduled proportional and integral gain terms, and u is the controller input term. For the blade pitch controller, the output is an adjustment to the collective blade pitch $\Delta\beta$ and the input is the difference between the desired and current generator speed $-\Delta\omega_{\mathrm{g}}$. For the generator torque controller, the output is an adjustment to the generator torque $\Delta\tau_{\mathrm{g}}$ and the input is also the difference between the desired and current generator speed $-\Delta\omega_{\mathrm{g}}$. In addition to this basic formulation, additional control, filtering, and smoothing modules are

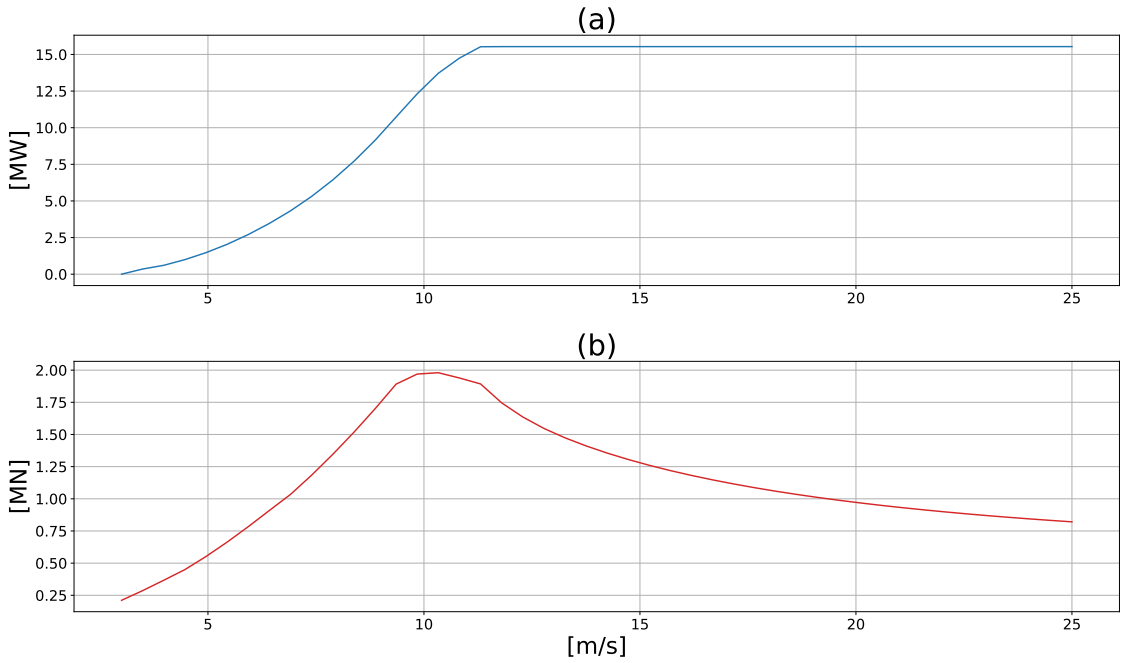

Figure 3.1: Static power (a) and thrust (b) curves as a function of wind speed for the IEA 15 MW RWT [52] as computed with the in-house BEMT method.

used to handle start-up and shut-down routines, transition between the below and above-rated control regimes near the rated wind speed, and rotor thrust peak shaving to minimize turbine loads [53].

To simulate the effect of a prescribed platform motion, the platform, tower, and rotor are assumed to be rigid. Sinusoidal functions prescribing the platform motion in surge are selected with amplitude A and frequency ω. These platform motions are converted to wind speed changes at the turbine rotor with equations 2.24 and 2.26.

To determine the performance of the turbine across its operational wind speed range, a wind speed step test is conducted. First, a step test is performed with no prescribed platform motion to simulate the performance of a static or fixed offshore wind turbine. The performance curves for this test are shown in Figure 3.1. These static values are then used to normalize the turbine performance during motion to characterize the difference between fixed and floating wind turbine performance during representative platform motion.

For the motion cases, seven periods of prescribed platform motion are simulated at wind speed steps of 0.25 m/s between 5 and 25 m/s. The last period of platform motion at each wind speed is separated, and the turbine power and thrust are measured to determine the average and fluctuating component of both. The definitions of

the average and fluctuating components of power and thrust are shown in Equations 3.2 through 3.5.

$$\Delta P = \frac{\max(P) - \min(P)}{2}, \tag{3.2}$$

$$\Delta T = \frac{\max(T) - \min(T)}{2}, \tag{3.3}$$

$$P_{\text{avg}} = \overline{P}, \tag{3.4}$$

$$T_{\text{avg}} = \overline{T}, \tag{3.5}$$

where P and T are the time series of power and thrust for the last period of prescribed platform motion. The fluctuating components of power and thrust are defined as the amplitude of the signal even though the power and thrust time series are not always harmonic. The action of the controller causes power and thrust to be non-harmonic functions, especially at and above the rated wind speed.

3.3 Response of the IEA 15 MW Reference Wind Turbine

We examine the prescribed surge motion of the platform at the natural surge frequency of the VolturnUS-S reference platform [62] (0.007 Hz), the natural surge frequency of the WindCrete Spar reference platform [70] (0.012 Hz), as well as a representative wave frequency defined by Fontanella et al. for a prospective FOWT site in the Mediterranean Sea [30] (0.111 Hz). At each frequency, the amplitude of motion is also varied between 5 and 10 m for the two low frequencies and 2 and 6 m for the wave frequency. For all test cases, a constant mean platform pitch of four degrees (backward tilt due to turbine thrust) is assumed. This angle is typical for operational conditions and slightly decreases average power capture, as the rotor plane is no longer perpendicular to the wind vector.

An example time series of the turbine's performance during motion at 0.111 Hz and 2 m amplitude at three different wind speeds is shown in Figure 3.2. In the below rated region (7.5 m/s free stream velocity) we see a harmonic response in turbine operation. The blades are set to fine pitch, and rotor speed fluctuates due to the torque controller to achieve optimal power capture as the motion induced wind speed varies. In the rated region (10.59 m/s free stream velocity) we see the generator torque capping at

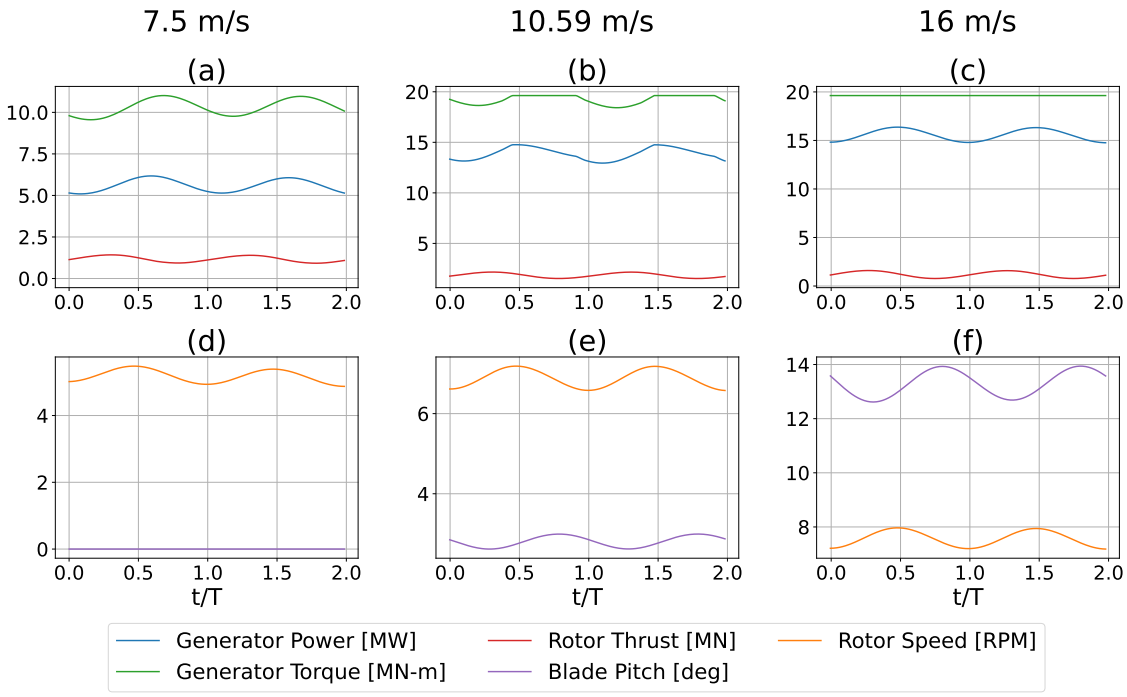

Figure 3.2: Performance of the IEA 15 MW RWT [52] at 7.5 m/s wind speed (a and d), at 10.59 m/s wind speed (b and e), and 16 m/s wind speed (c and f) during prescribed platform surge motion of 0.111 Hz frequency and 2 m amplitude. Power, generator torque, and rotor thrust are shown in a, b and c, while blade pitch and rotor speed are shown in d, e, and f.

its maximum value when upwind motion of the turbine causes the rotor experienced wind speed to exceed the rated wind speed. However, aerodynamic torque is still able to vary. The rotor speed, a function of aerodynamic and generator torque, varies, and the blade pitch controller remains active, so there is some variation in power capture. Above the rated wind speed (16.0 m/s free stream velocity), the generator torque is constant at its maximum allowed value. However, the other turbine parameters vary as the controller attempts to achieve optimal operating conditions as the platform induced wind speed varies.

The average and fluctuating components of turbine power and thrust over the entire wind speed range during surge motion at the three frequencies of interest are shown in Figures 3.3, 3.4, and 3.5. The average components of power and thrust are normalized by the static power and thrust at that wind speed, while the fluctuating components are normalized by the turbine rated values.

We find that the effect of platform motion scales with $\frac{U_{induced}}{U_\infty}$, where a larger motion-induced velocity causes a larger effect on power and thrust. The specific effect of motion varies based on the wind speed regime and resulting controller response.

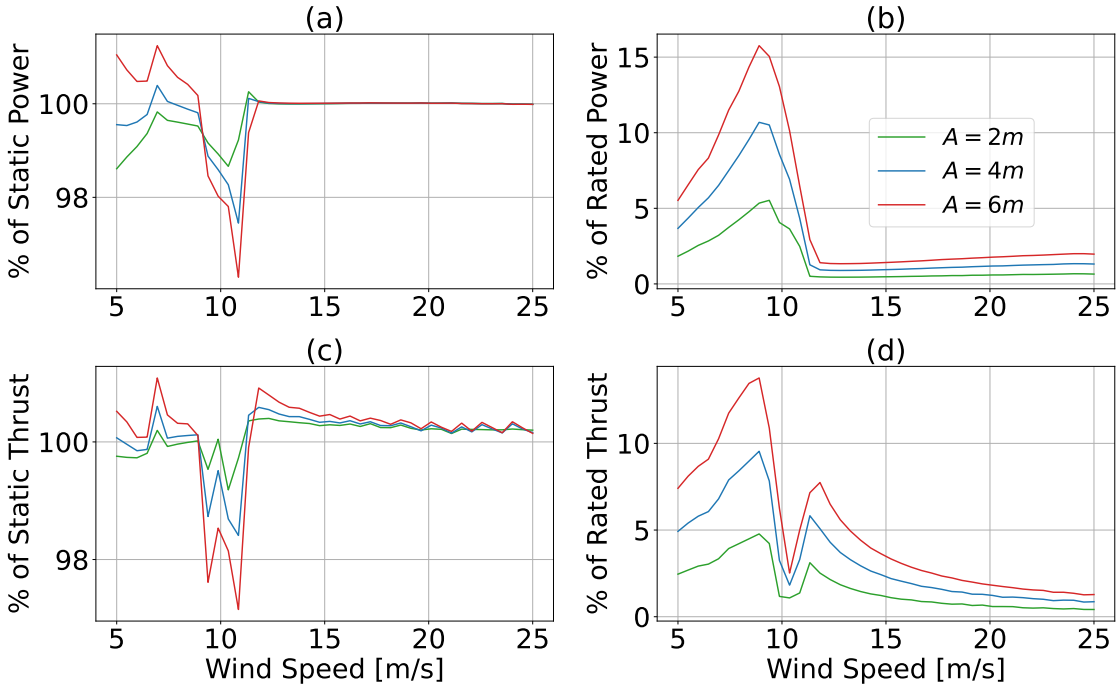

Figure 3.3: Normalized average component of power (a), fluctuating component of power (b), average component of thrust (c), and fluctuating component of thrust (d) as a function of wind speed in prescribed surge motion at 0.007 Hz (Volturn-US surge natural frequency).

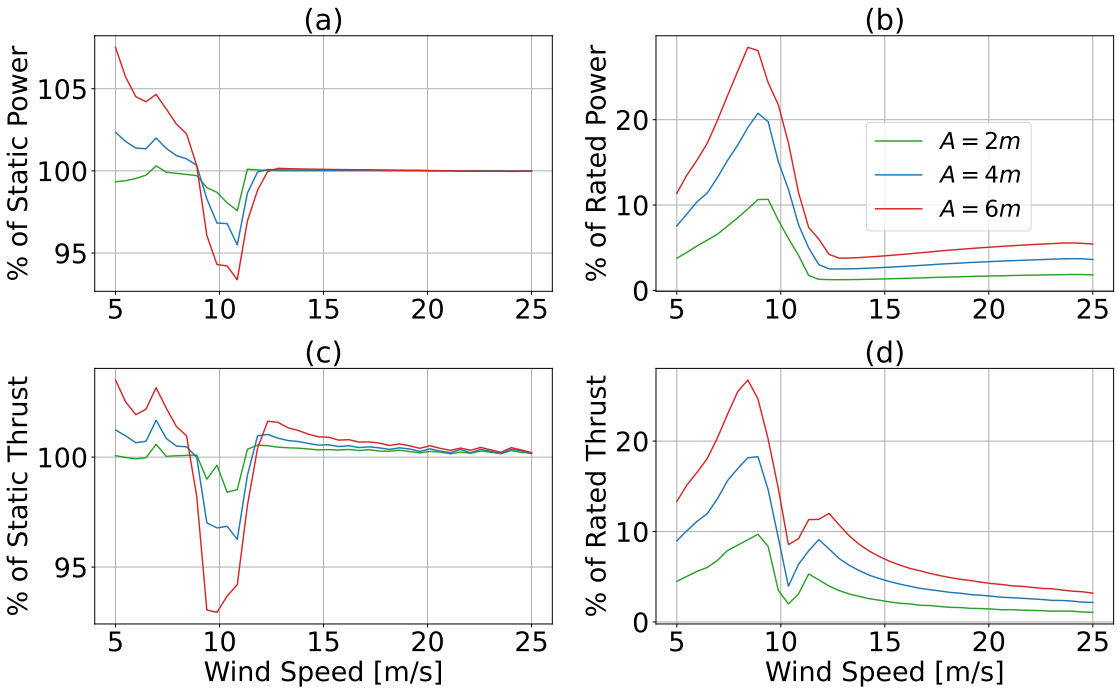

Figure 3.4: Normalized average component of power (a), fluctuating component of power (b), average component of thrust (c), and fluctuating component of thrust (d) as a function of wind speed in prescribed surge motion at 0.012 Hz (WindCrete surge natural frequency).

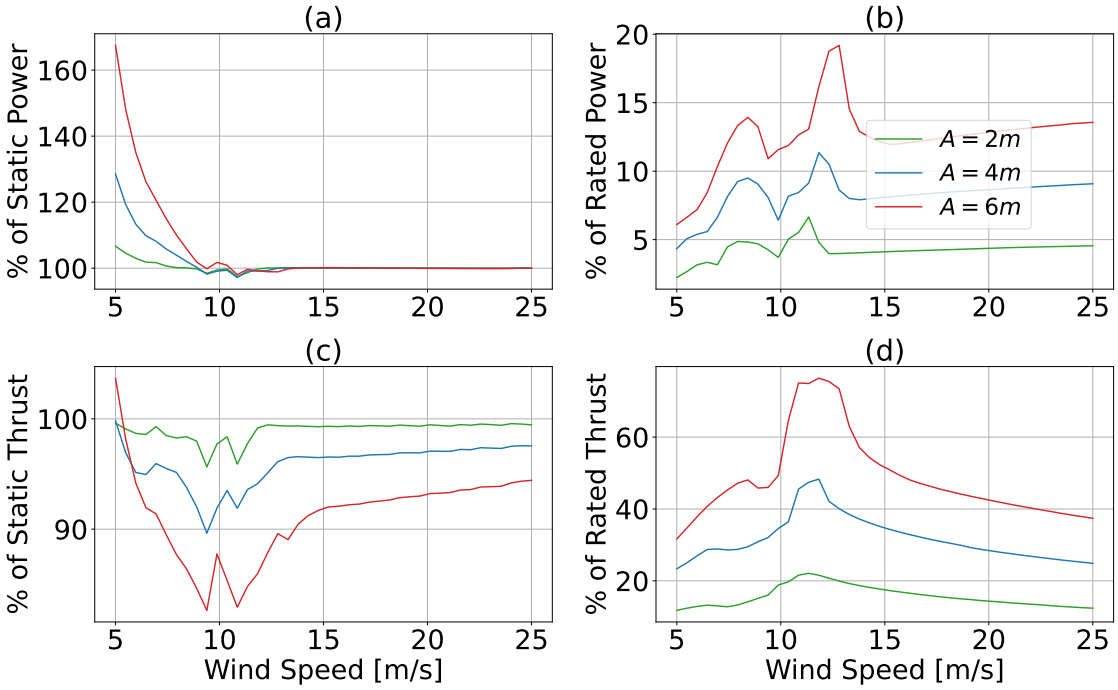

Figure 3.5: Normalized average component of power (a), fluctuating component of power (b), average component of thrust (c), and fluctuating component of thrust (d) as a function of wind speed in prescribed surge motion at 0.111 Hz (representative wave frequency).

In the below-rated region (between 3 m/s and about 9 m/s) average power capture is increased by 2 to 60% at 5 m/s and 0 to 15% at 8 m/s compared to the static turbine benchmark. This increase in average power capture over a platform motion cycle is due to the cubic relation between wind speed and power. The increase in turbine power production during the upwind motion portion of the oscillation outweighs the decrease in power production during the downwind motion portion of the oscillation due to the cubic scaling between power and wind speed. In this same region, the average thrust increases by up to 7 % difference from static. This suggests an increase in turbine performance compared to static as turbine power capture increases more than rotor thrust under a prescribed platform motion when wind speed is low. This result supports the findings of Cottura and Caradonna [26] discussed previously.

This finding is qualified by the observation that platform motion causes a variance in rotor torque and thrust, which has important implications for component loading. The amplitude of both power and thrust increases up to 30% of rated in the low frequency cases and 70% for the high frequency case. In the below rated region, the varying loads will not exceed the rated torque and thrust, so it is unlikely that an unsafe load will be encountered. However, load cycling can have significant effects on component fatigue. This is not explored further here, but must be taken into consideration in FOWT design and is left for future work.

Conversely, power capture is decreased (up to 6% difference to static) close to the rated wind speed (9 m/s to 15 m/s). In this region, thrust is also decreased by up to 8% compared to static. This decrease is due to the turbine controller which caps the power generated at its rated value. This limiting is done to avoid above rated loads when the platform motion induces a wind speed above rated. However, the turbine cannot capture the rated power when the platform motion adjusted wind speed is below rated, causing a decrease in average power capture over the motion cycle. This behavior is dependent on the specific controller used. However, ROSCO's behavior in this case is representative of the most commonly used open source control models, the NREL 5 MW controller [71] and the DTU 10 MW controller [72].

Once the wind speed increases sufficiently, the platform motion never causes motion-induced wind speed to drop below rated. At this point, power capture and thrust return to their rated, or static turbine, values. This return to static operation occurs when the free stream velocity is greater than the sum of the rated wind speed and maximum velocity induced by the platform motion. As such, it is dependent on the specific platform motion amplitude and frequency.

The effect of a prescribed platform motion on turbine performance can thus be generally categorized by the turbine's three operational regions. Motion is possibly beneficial in region one (below rated wind speed), clearly detrimental in region two (near rated wind speed), and possibly unimportant in region three (significantly above rated wind speed). These results suggest that platform motion can increase power capture in limited conditions.

3.4 Discussion and Conclusions

Static performance curves are often used to estimate the suitability of a potential wind farm and estimate long-term power production [68, 69]. However, motion's effect on performance is not accounted for, and motion-adjusted performance curves of the average and fluctuating components of power and thrust for the IEA 15 MW RWT had not been published before this project. With this low fidelity BEMT method, we demonstrate a way to account for platform motion in turbine power and thrust curves and increase the accuracy of long-term turbine performance prediction. However, it is important to note that the prescribed harmonic motions used here are only representative of possible motion responses. Through fully coupled aero-hydrodynamic modeling, we can better predict platform motion and turbine response. This is discussed further in Chapter 4.

Using the BEMT method to predict the effect of a prescribed platform motion across the operational wind speed spectrum of a turbine, we find that the effect of motion is highly dependent on wind speed region. Platform motion is shown to be the most detrimental to power capture around rated wind speed. However, the average thrust experienced by the turbine is also significantly decreased in this region. It is important to note that the turbine response near rated wind speeds is heavily influenced by controller design. The results presented here are produced with the NREL ROSCO controller which is meant to be representative of industry standard control practices, but may not be representative of all wind turbine controllers. At below rated wind speeds, platform motion enhances power capture, while it has little effect at high wind speeds.

As discussed in Chapter 2, BEMT has some inherent drawbacks and limited accuracy. As such, small differences between floating and fixed turbine performance predicted by the BEMT model should be explored with higher fidelity methods to confirm their existence. However, the prediction of large increased power capture (up to 60 % relative to static for 0.111 Hz motion) in the below rated region and large

fluctuations of rotor thrust (75 % of turbine rated thrust between 10 and 15 m/s wind speed) are significant relative to the accuracy of BEMT. The decrease in power capture around the rated wind speed has a similar magnitude to the magnitude of BEMT error discussed in Chapter 2. However, this finding has a strong grounding in accepted turbine controller behavior.

These results suggest that platform motion could be beneficial to turbine operation in certain wind regimes. This result supports the findings of Cottura et al. [26] and Dabiri [73] who found that the motion of the rotor disk, such as that of an FOWT, can increase average power capture. This raises the possibility of controller design that aims to damp motion near rated speeds, but that allows some motion at lower wind speeds. Additionally, depending on the predominant wind speeds and wave conditions of a potential turbine site, a platform or controller that decreases platform motion may be more or less important. In a site that almost always experiences very high or very low wind speeds, platform motion will not decrease turbine average power capture. This has important ramifications for any site-specific platform design or controller tuning.

Chapter 4

A Low Fidelity Coupled Aero-Hydrodynamic Model for Floating Offshore Wind Turbines

4.1 Introduction

In order to accurately model FOWT motion and performance, it is necessary to utilize a coupled, aero-hydrodynamic model which takes into account aerodynamic loading at the rotor as well as hydrodynamic loading at the floater. Coupled models have been developed with frequency domain [74, 49] implementations, as well as in the time domain by tools such as OpenFast [31]. OpenFast has been adopted as an industry standard tool, being utilized to demonstrate compliance with IEC [75] and DNV [76] design standards [77]. NREL's OpenFast is an aero-hydro-servo-elastic model incorporating potential flow-based hydrodynamic loading from input sea states, aerodynamic loading computed with BEMT or generalized dynamic wake (GDW) models, and linear elastic solid body modeling of the tower and drive train. Turbine control is simulated with the reference open source PI-based controller ROSCO [53]. Multiple authors have utilized OpenFast to study FOWT performance with varying floating platforms and in varying environmental conditions. Mahfouz et al. 2021 [28] use OpenFast to examine turbine performance and platform motion response under 14 load cases including operational and extreme conditions. The authors examine a spar type and semi-submersible platform for the IEA 15 MW RWT and conclude that for load cases where the turbine is operating, platform motion is dominated by wind forces. The work of Mahfouz et al. does not characterize turbine power performance. Fontanella et al. 2024 [30] utilize OpenFast to study the performance of the IEA 15 MW RWT in prescribed harmonic motion, under regular wave loading,

and under irregular waves defined by characterization of ERA 5 reanalysis data [78] for a representative turbine site. Their work examines a single site over the period of one year. They find that the floating turbine has an annual energy production within 1 % of a static turbine in the same site. The regular wave cases examined by Fontanella et al. include amplitudes up to 3 m and six wave frequencies. We will examine a wider range of both wave amplitude and frequency.

All of the types of aerodynamic models discussed in Chapters 1 and 2 can be coupled with a hydrodynamic solver of varying fidelity. As such, there is a wide range of coupled FOWT models which vary in accuracy and computational expense. Liu et al. [18] demonstrate a high-fidelity model, utilizing the OpenFOAM CFD toolbox. RANS-CFD is used to model air flow, and the air-water interface is captured with the volume of fluid (VOF) method to study the fully coupled NREL 5-MW reference turbine and OC4 semi-submersible floating platform system. Their analysis includes aerodynamic effects on the rotor, wave-induced effects on the floating platform, and mooring line effects. This CFD model predicted a 9.6 % maximum decrease in thrust coefficient and an 8.4 % maximum increase compared to turbine thrust with no platform motion under operational wind and sea-state conditions. This same wind and sea-state induced a maximum 15.1 % increase and a maximum 14.2 % decrease in turbine power coefficient. Only two cases were tested, and simulation length with this model was limited to 350 s due to its high computational cost.

Coupled models have also been utilized in experimental campaigns. Ransley et al. [67] utilize a 1:70th scale experimental model of the IEA 15 MW RWT with a real-time aerodynamic force emulator to explore the induced motion of the UMaine Volturn-US semi-submersible platform. Their work illustrated that the floater's motion response would largely occur at either incoming wave frequencies or at platform natural frequencies. Moreover, their results show that surge motion at the wave frequency is driven by wave loading, whereas surge motion at the surge natural frequency is dependent on aerodynamic thrust loading. In contrast, the pitch motion response at the wave frequency is dependent on aerodynamic loading. However, these types of experimental models are expensive in terms of cost and time to develop.

Lower fidelity coupled models have been applied by authors such as Cottura et al. [29] who use a first-order, potential flow hydrodynamic solver and BEMT aerodynamic solver with a single degree of freedom control model to predict the performance of the NREL 5 MW RWT in irregular waves.

Chen et al. [27] also analyze the NREL 5 MW RWT, but with a coupled wave energy converter in the floating platform. They utilized OpenFast's Aerodyn [33]

BEMT solver and conducted the hydrodynamic time domain simulation in ANSYS AQWA. They show a significant damping effect from the turbine, which reduces the motion response of the coupled FOWT wave energy converter compared to just a wave energy converter. However, these results are not extended to the effect of motion on the turbine power performance. Zilic de Arcos [79] couples the ANSYS AQWA potential flow solver with an in-house BEMT code to study the response of a floating tidal turbine.

We aim to characterize the performance difference between floating and static turbines due to wind and wave induced platform motion in realistic, operational sea-states. We are interested in trends in turbine performance that occur over long time periods, as these will be key to evaluating the economic viability of novel FOWT installations. We also focus on testing design variables that will have relatively large effects on turbine performance, such as whether to use a floating or fixed-bottom turbine base and selection between turbine sites separated by hundreds of miles. As such, we elect to utilize low-fidelity modeling which is able to predict significant trends in turbine performance over large timescales.

In Chapter 2, we demonstrated that the in-house aerodynamic model presented performed with a 2.3 % difference in thrust coefficient and a 4.4 % difference in power coefficient at the turbine rated wind speed with no platform motion relative to OpenFast, which includes flexible blade modeling. We also conclude from that verification that our assumption of a rigid turbine will cause a slight over prediction of power and thrust. However, less than a 5 % variation is considered acceptable, as we are primarily interested in large trends in turbine performance. Here we use the same ANSYS AQWA potential flow solver utilized by Zilic de Arcos and Chen et al. coupled with the in-house BEMT solver presented in Chapters 2 and 3. In this chapter, we present a coupled model for FOWT performance prediction and utilize this model to examine the power performance and thrust loading of the IEA 15 MW RWT [52] and UMaine Volturn-US semi-submersible floating platform [62] under regular wave loading with a wide range of amplitude and frequency.

4.2 Methods

The aerodynamic module used for the coupled aero-hydrodynamic model is the same as that described in Chapters 2 and 3. We use the in-house BEMT solver with Prandtl's hub and tip loss correction and Glauert's turbulent wake method. Again, as described in Chapter 3, we use the reference open-source controller ROSCO presented

by Abbas et al. [53]. As we are now utilizing a fully coupled model, we include the floating feedback functionality which is optional in the ROSCO controller. The floating feedback control module is designed to ensure turbine stability, especially in platform pitch. The floating feedback term is proportional to the nacelle acceleration in the freestream direction and added to the collective blade pitch control signal.

$$\Delta\beta = k_{\mathrm{p}}\Delta\omega_{\mathrm{g}} + k_{\mathrm{i}}\int_0^T \omega_{\mathrm{g}} dt + k_{\beta_{\mathrm{float}}}\Delta\dot{x}_t, \tag{4.1}$$

where $\Delta\beta$ is the blade pitch control signal, k_{p} and k_{i} are the proportional and integral gains, $\Delta\omega_{\mathrm{g}}$ is the generator speed error input (the difference between the generator speed and the desired generator speed), $k_{\beta_{\mathrm{float}}}$ is the proportional floating feedback gain, and $\Delta\dot{x}_t$ is the nacelle fore-aft acceleration.

The FOWT hydrostatics and hydrodynamics are simulated using ANSYS AQWA [80]. AQWA is a potential flow-based, hydrodynamic solver in the ANSYS Workbench environment, which is capable of simulating loads on floating bodies in the frequency and time domain. The solver consists of two modules: a radiation and diffraction pre-processing stage, and a time or frequency domain solver. The radiation and diffraction study meshes the floating body with triangular or quadrilateral elements and solves the potential flow problem via the panel method to determine the hydrodynamic added mass, radiation damping, and first-order wave excitation forces. Second-order forces are represented in AQWA as mean drift forces, computed via Newman's far field method, or as quadratic transfer function (QTF) matrices, which are computed in the radiation and diffraction study based on the near field integration over the mean wetted body surface. We model hull viscous drag through additional, frequency-independent damping matrices based on CFD simulation of the hull conducted by Allen et al. [62].

The hydrostatic force and moment on the partially submerged platform are expressed as follows:

$$F_{\mathrm{hys}} = -\int_{S_0} p_s n dS, \tag{4.2}$$

$$M_{\mathrm{hys}} = -\int_{S_0} p_s (r \times n) dS, \tag{4.3}$$

where $p_s = -\rho g Z$ is the hydrostatic pressure and r is the position vector of a point on the hull surface relative to the platform center of gravity. The vertical component of F_{hys} is the buoyancy of the submerged structure.

The time or frequency domain simulation module is capable of linearized frequency domain modeling or time domain modeling with non-linear excitation forces. The frequency domain model conducts a linearization at the system's equilibrium point of any non-linear forcing such as dynamic mooring line forcing or Morrison drag elements. Further detail on the linearization methods can be found in the AQWA Theory Manual [80]. At this point, the equation of motion in the frequency domain can be expressed as follows:

$$\left[-\omega^2 M - i\omega C + K\right] X = F, \tag{4.4}$$

where M, C, and K are the 6x6 mass, damping, and stiffness matrices respectively, X is the 6x1 motion response amplitude, and F is the 6x1 external force amplitude at frequency ω. M and C include added mass and damping terms, and K includes stiffness due to the hydrostatic restoring force and moment. This equation can be used to compute the system's fully coupled response amplitude operators (RAOs) when the excitation force is induced only by a regular wave of unit amplitude, and the stiffness matrix includes both hydrostatic and structural stiffness components.

For solutions in the time domain, Equation 4.4 can be directly converted to the time domain when $f(t)$ is periodic with constant amplitude.

$$M\ddot{x}(t) + C\dot{x}(t) + Kx(t) = f(t). \tag{4.5}$$

However, if $f(t)$ is not periodic with constant amplitude, as will be the case with any non-linear mooring, drag, or aerodynamic forces, then the time domain equation of motion must be expressed via a convolution integral.

$$\left[m + A_\infty\right]\ddot{x}(t) + c\dot{x}(t) + Kx(t) + \int_0^t R(t-\tau)\dot{x}(\tau)\mathrm{d}\tau = f(t), \tag{4.6}$$

where m is the structural mass matrix, A_∞ is the added mass matrix at infinite frequency, c is the damping matrix without linear radiation damping effects due to diffraction panels, K is the stiffness matrix, and R is the velocity impulse function matrix. The frequency independent damping matrix used to model viscous drag is added to the matrix c.

The forcing term $f(t)$ accounts for mooring loads in addition to external loads such as the aerodynamic loads from a floating turbine rotor. Here we use the built-in dynamic, composite, catenary mooring line model in AQWA. This cable model discretizes the catenary cables into sections along the mooring line length and models

the drag forces, inline elastic tension, bending moments, and mass of each cable element. The equations of motion of a single cable element are as follows:

$$\frac{\delta F_{\mathrm{T}}}{\delta s_e} + \frac{\delta V}{\delta s_e} + W + F_h = m\frac{\delta^2 R}{\delta t^2}, \tag{4.7}$$

$$\frac{\delta M_{\mathrm{b}}}{\delta s_3} + \frac{\delta R}{\delta s_e} \times V = -q, \tag{4.8}$$

where m is the mass per unit length, q is the moment loading per unit length, R is the position vector of the first node of the element, δs_e is the length of the element, W is the element weight, F_{h} is the hydrodynamic loading vector determined by Morrison's drag equation, and F_{T}, M_{b}, and V are the tension, bending moment, and shear force vectors at the first node of the element.

Importantly for the coupled aero-hydrodynamic model, the forcing term $f(t)$ can be modified with a user-defined force via an external force server. This server is activated by linking the AQWA executable file and an external Python script containing the in-house BEMT aerodynamic solver through a transmission control protocol (TCP) socket. The AQWA time domain solver will then send data on its computed structural motion response at each time step and receive data on the aerodynamic solver's computed additional forces, which are added to the forcing term for the next simulation time step. Documentation for the custom user force server workflow can be found in the ANSYS AQWA reference manual [81].

At each time step, AQWA sends a six degree of freedom velocity and position vector about the structure's center of gravity to the external Python server. The Python script then calculates the motion at the rotor hub due to the platform motion as well as the current position of the turbine hub. The hub velocity and platform pitch angle are used to find the adjusted wind speed due to platform motion as follows:

$$U_{\infty,\mathrm{adj}} = U_\infty \cos(\Theta) + U_{\mathrm{hub}} \cdot \hat{u}_\infty, \tag{4.9}$$

where U_∞ is the undisturbed free stream velocity vector, U_{hub} is the hub velocity, Θ is the platform pitch angle, and $\hat{u}_\infty$ is the unit vector parallel to the free stream. The BEMT solver is then used to calculate the aerodynamic forces and power capture. The aerodynamic forces are sent back to the AQWA hydrodynamic solver via the server as a six degree of freedom vector about the structure's center of gravity.

$$F_{\mathrm{aero}}(t) = \begin{bmatrix} T(t)\cos(\Theta)\cos(\Gamma)\cos(\beta) - \frac{Q_{\mathrm{gen}}(t)}{H(t)}\sin(\beta) \\ T(t)\cos(\Theta)\sin(\Gamma)\sin(\beta) + \frac{Q_{\mathrm{gen}}(t)}{H(t)}\cos(\beta) \\ T(t)\sin(\Theta) \\ T(t)H(t)\sin(\beta) \\ T(t)H(t)\cos(\beta) \\ 0 \end{bmatrix}, \tag{4.10}$$

where β is the angle of the incident wind vector, T is the rotor thrust, Q_{gen} is the generator torque, $H(t)$ is the vertical (z-axis) hub position at that time step, Θ is the current platform pitch angle, and Γ is the current platform yaw angle. In cases where the wind direction is aligned with the platform zero degree heading, this vector reduces to the following:

$$F_{\text{aero}}(t) = \begin{bmatrix} T(t)\cos(\Theta)\cos(\Gamma) \\ T(t)\cos(\Theta)\sin(\Gamma) + \frac{Q_{\text{gen}}(t)}{H(t)} \\ T(t)\sin(\Theta) \\ 0 \\ T(t)H(t) \\ 0 \end{bmatrix}, \tag{4.11}$$

Although some aerodynamic heave forcing may occur due to the platform pitch angle, which causes some rotor thrust to act along the z-axis, this term is considered to be negligible relative to the platform's hydrostatic and hydrodynamic forces.

4.3 Coupled Aero-Hydrodynamic model for the IEA 15 MW Reference Wind Turbine and UMaine Volturn-US Floater

We study the effect of wind and wave induced motion on floating offshore wind turbines through the reference case of the IEA 15 MW Reference Wind Turbine [52] with the University of Maine Volturn-US Semi-Submersible Floating Platform [62]. A rendering of the system is shown in Figure 4.1. Details of the IEA 15 MW RWT have been discussed in both Chapters 2 and 3. The NREL Reference Open Source Controller (ROSCO) presented by Abbas et al. [53] is used to simulate turbine control. The ROSCO controller employs below rated generator torque control, above rated collective blade pitch control, as well as a floating feedback module designed to prevent large platform pitch motions. The UMaine Volturn-US floater is a semi-submersible platform with three outer columns arrayed with 120 degree symmetry around a central column upon which the turbine is mounted. The columns are connected with submerged, rectangular pontoons and the platform utilizes a three cable catenary mooring system. Key characteristics of the floater are shown in Table 4.1. Exact dimensions of the floater and mooring configuration can be found in the reference document [62].

Allen et al. [62] present a viscous drag model for the Volturn-US platform in the reference document. The platform's viscous damping was calculated using the

Platform Type	Semi Submersible
Excursion (length, width, height)	90.1, 102.1, 290.0 m
Freeboard	15 m
Draft	20 m
Platform Mass	17,839 t
Total System Mass	20,093 t
Vertical C.o.G from SWL	-14.94 m
Vertical C.o.B from SWL	-13.63 m
Roll Inertia about C.o.G	1.251 E10 kg – m^2
Pitch Inertia about C.o.G	1.251 E10 kg – m^2
Yaw Inertia about C.o.G	2.367 E10 kg – m^2

Table 4.1: Key Properties of UMaine Volturn-US Semi-Sub Floater [62].

Figure 4.1: Rendering of the IEA 15 MW RWT and UMaine Volturn-US platform from the Volturn-US definition document [62].

	Surge	Sway	Heave	Roll	Pitch	Yaw
Surge	9.225 E5	0	0	0	-8.918 E6	0
Sway	0	9.225 E5	0	8.918 E6	0	0
Heave	0	0	2.296 E6	0	0	0
Roll	0	8.918 E6	0	1.676 E10	0	0
Pitch	-8.918 E6	0	0	0	1.676 E10	0
Yaw	0	0	0	0	0	4.798 E10

Table 4.2: Viscous Damping Matrix for the Volturn-US [62] (Ns^2/m^2, Ns^2/m, Nms^2).

Type	Chain Catenary
Line Type	R3 Studless Mooring Chain
Number of Lines	3
Fairlead Depth	14m
Anchor Depth	70 m
Anchor Radial Spacing	837.6 m
Nominal Chain Diameter	185 mm
Dry Line Linear Density	685 kg/m
Extensional Stiffness	3270 MN
Unstretched Length	850 m
Normal Added Mass	1
Tangential Added Mass	1
Normal Drag	2
Tangential Drag	1.15

Table 4.3: Characteristics of the Volturn-US [62] mooring system.

incompressible, steady-state solver in OpenFOAM. The net drag load was computed during 1 m/s or 1 deg/s fluid velocity about the surge, heave, roll, and yaw degrees of freedom. The resulting viscous damping matrix is shown in Table 4.2.

The platform definition mooring system is designed for 200 m water depth and is made up of three catenary mooring lines which run parallel to each of the platform legs (120 degree angle in between lines). The fairleads are located 14 m below mean sea water level (SWL), and the anchors are placed at 200 m depth and 837.6 m horizontally from the fairleads. Each cable has an unstretched length of 850 m. Key characteristics of the mooring cables are also defined in the reference document [62] and can be found in Table 4.3.

4.3.1 Mesh Convergence Study

The body meshing process only affects the run time of the radiation diffraction study, which only has to be run a single time for the platform. As such, element size does not

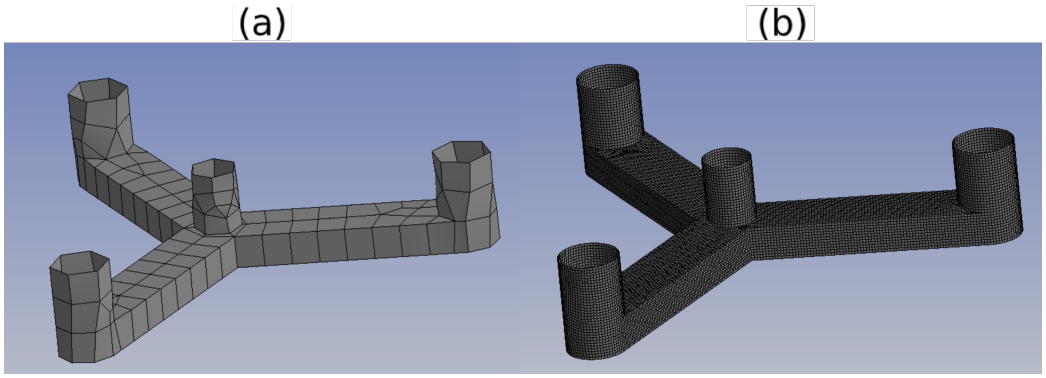

Figure 4.2: 6 m average element size mesh (a), and 0.6 m average element size mesh (b) for the floating platform.

have a large effect on the computational cost for the full time domain study. The mesh size does have a large effect on the potential flow solver. Despite this, we still present a mesh convergence study for the element sizing of the Volturn-US platform. Average element sizes between 6 m and 0.6 m were tested. These two element sizes result in 272 and 23037 total elements for the modeled Volturn-US geometry, respectively. Figure 4.2 shows meshes for both the 6 m and 0.6 m element sizes.

To determine mesh convergence, we compared the results of the first order hydrodynamics radiation and diffraction study, namely the added mass and damping matrices. The non-zero terms in the frequency dependent added mass matrix for varying mesh sizes are shown in Figure 4.3 while the same for the damping matrix is shown in Figure 4.4. We see that the 6 m average element size mesh results in larger absolute values for all terms in the added mass matrix. The A_{33} and A_{44} terms are especially sensitive, with peak values 16 % and 17 % higher for the 6 m element size versus the 0.6 m element size. The damping matrix is generally less sensitive to element size than added mass. However, damping does exhibit significant differences between the coarsest and finest meshes at peak frequencies. For example, there is a difference of 35 % for the B_{33} and B_{44} terms at 0.1 Hz between the 6 m and 0.6 m element size meshes. However, at frequencies that do not result in a local maxima or minima of damping, the effect of element size is minimal. Additionally, we can see a qualitative convergence of the meshes below an element size of about 2 m. Between the 2 m and 0.6 m element size meshes, we see a difference of 2 % and 0.5 % at 0.08 Hz for the A_{33} and A_{44} terms respectively. Again, these terms are the most sensitive to the mesh element size.

To quantitatively describe the mesh convergence, we compare the frequency dependent added mass matrix with the added mass matrix in the Volturn-US definition

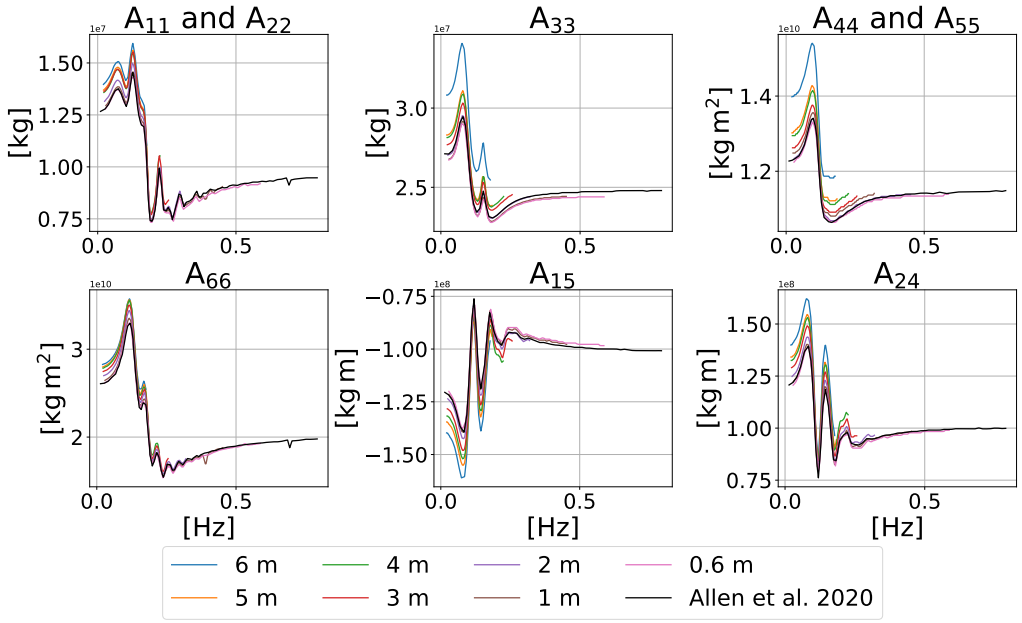

Figure 4.3: The hydrodynamic added mass computed in the radiation diffraction study by ANSYS AQWA for average mesh element sizes between 6 and 0.6 m.

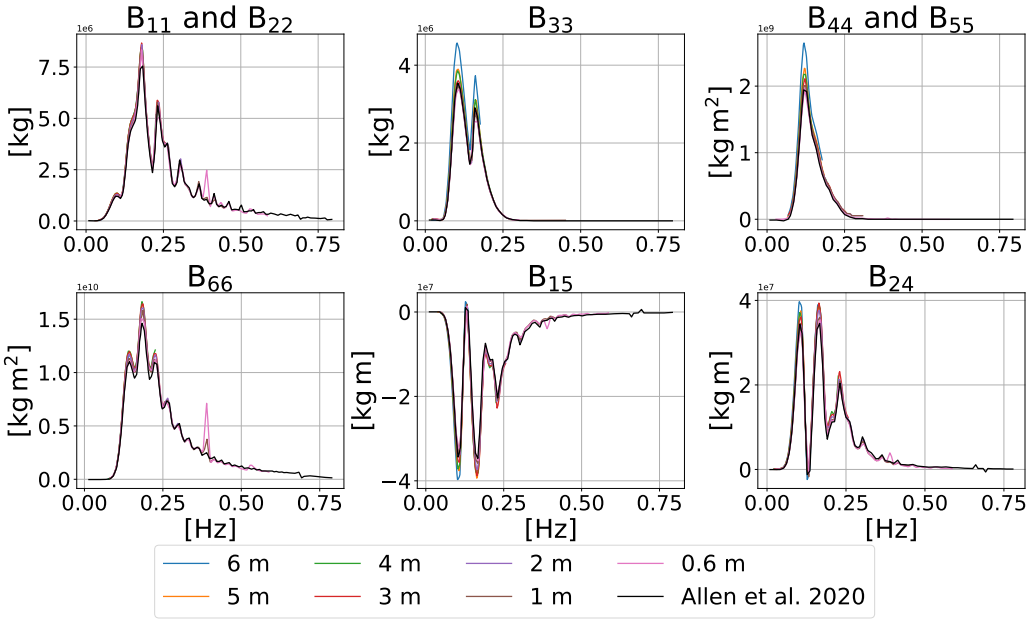

Figure 4.4: The hydrodynamic damping computed in the radiation diffraction study by ANSYS AQWA for average mesh element sizes between 6 and 0.6 m.

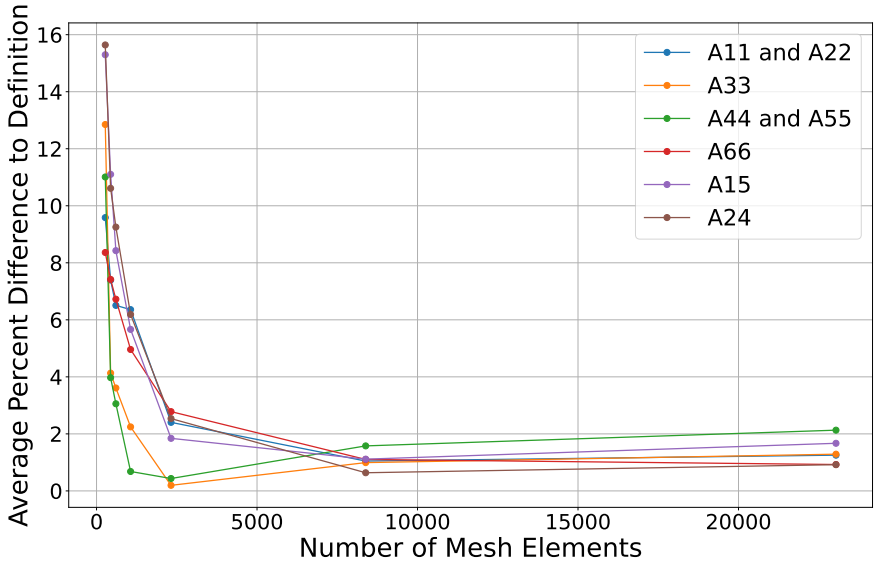

Figure 4.5: Average percent difference at all frequencies between the AQWA and definition added mass matrix for varying meshes.

document for varying mesh sizes. The definition added mass matrix is computed in WAMIT, an alternative potential flow solver to AQWA. For each mesh, the average percent difference between the definition matrix and the AQWA matrix at all frequencies is plotted. The results of this study are shown in Figure 4.5. We see a fairly constant difference of less than 3 % to the definition added mass matrix for meshes with an average element size of 2, 1, and 0.6 m, indicating good convergence at or below a 2 m element size. A convergence study of the damping terms was also conducted, yielding similar results. Given the objectives of this study, any mesh below 2 m element size is considered to be sufficient. For potential flow modeling, an element size near 2 m is desirable to minimize computational cost. For the time domain simulation presented here, using an element size significantly below 2 m is preferable, as it does not significantly contribute to computational expense.

4.3.2 First and Second Order Hydrodynamics

Due to the negligible impact on computational cost for time domain simulation, the finalized radiation and diffraction study in AQWA was conducted with a 0.6 m average element size mesh. The non-zero terms of the hydrodynamic added mass and damping matrices are shown in Figures 4.6 and 4.7 as a function of incoming wave frequency.

In addition to the first order added mass and damping coefficients, the quadratic

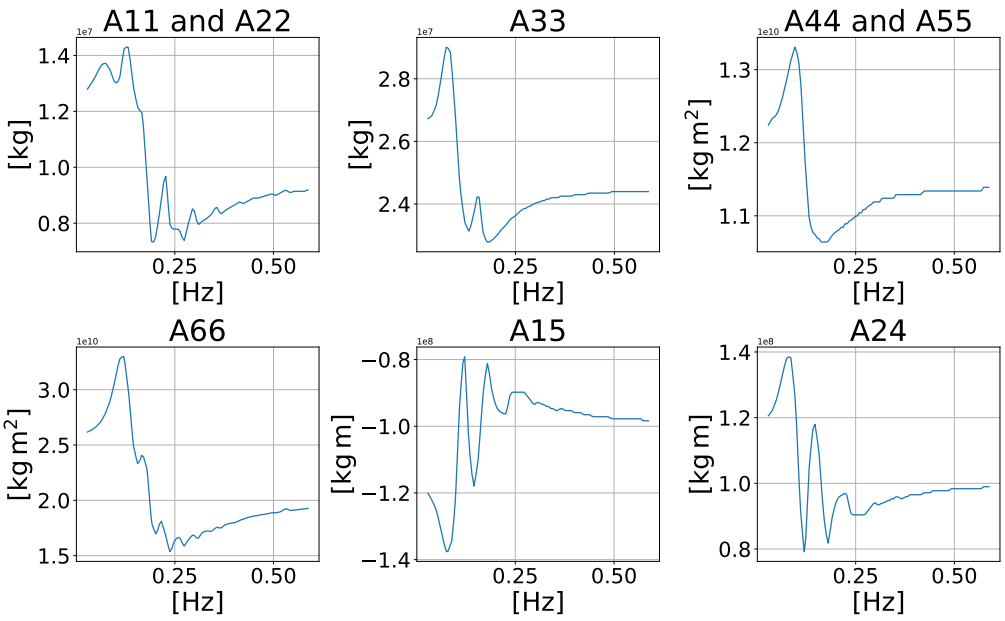

Figure 4.6: Non-zero terms of the hydrodynamic added mass matrix for the floating platform.

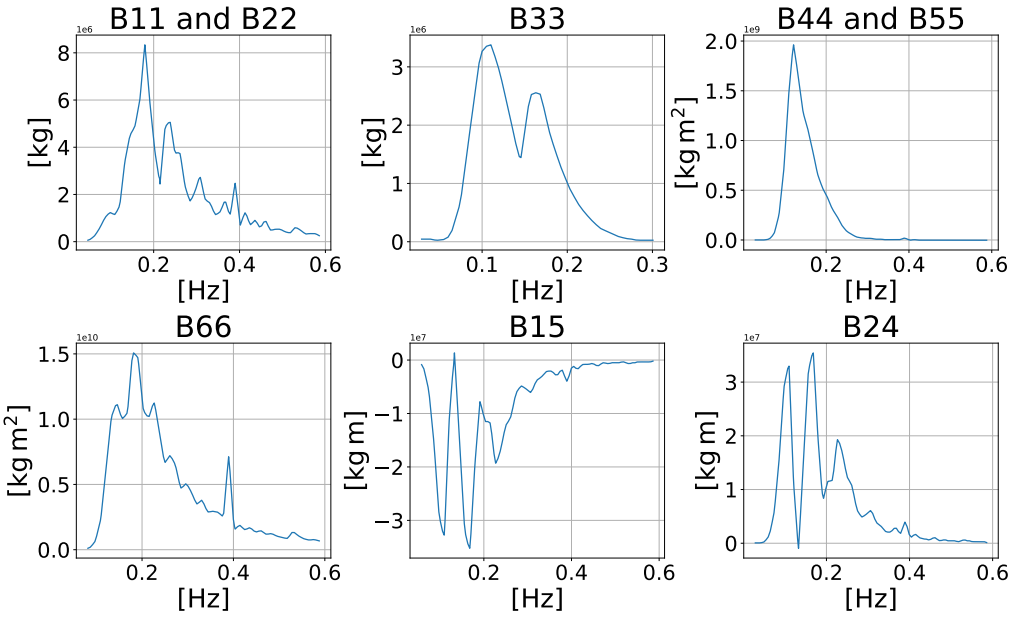

Figure 4.7: Non-zero terms of the hydrodynamic damping matrix for the floating platform.

transfer functions (QTFs) for the platform are shown in Figures 4.8. These QTFs account for second order effects (those proportional to the square of wave amplitude), improving the modeling of non-linear effects like platform slow-drift or sum and difference frequency wave loads.

4.3.3 Turbine Performance in Still Seas

The power and thrust performance of the IEA 15 MW RWT on the UMaine Volturn-US semi-submersible floater was simulated with the coupled model presented above. A wind speed step test was run across the turbine's operational wind speed range at 0.5 m/s increments. Each wind speed step was simulated for 600 seconds. No waves were applied, assuming completely still seas. Additionally, a turbulence model was applied to more accurately simulate turbine operation. A Kaimal turbulence spectrum defined in IEC standards [82] was applied at each 600 second wind speed step with turbulence intensity equal to 6 %. The Kaimal spectrum power spectral density of the streamwise turbulence is defined as:

$$S_u(f) = \frac{4\sigma_u^2 L_u}{U_\infty} \times \frac{1}{(1 + 6fL_u/U_\infty)^{\frac{5}{3}}}, \tag{4.12}$$

where $S_u(f)$ is the PSD, $L_u = 0.7 \times H_{\text{hub}}$ is the integral length scale, and $\sigma_u = I_u U_\infty$ is the standard deviation of the wind speed fluctuations, and I_u is the turbulence intensity. The turbulence modeling is discussed in more detail in Chapter 5 Section 5.2.3. In addition, the same simulation procedure was conducted with all six degrees of freedom of the floater locked, to simulate the performance of a fixed-bottom, or static, turbine. The performance curves for the floating and static turbine are shown in Figure 4.9.

In addition, the platform pitch angle during the wind speed step test used to obtain the FOWT performance curves is shown in Figure 4.10. Rotor thrust causes a platform pitch angle which peaks at an average of 2.6 degrees at the rated wind speed. At this same wind speed, the platform pitch angle varies between 2.1 and 3.1 degrees due to variations in wind speed caused by turbulence. The variation in rotor thrust due to wind speed turbulence also causes fluctuations between 1.5 and 2 m to the platform surge position at the rated wind speed. Although the average platform pitch angle is maximum at the rated wind speed, the maximum variation in platform pitch angle peaks for slightly higher wind speeds: between 11 and 14 m/s. This is due to lower nacelle fore-aft accelerations slightly above the rated wind speed as compared to at the rated wind speed. The nacelle fore-aft acceleration is

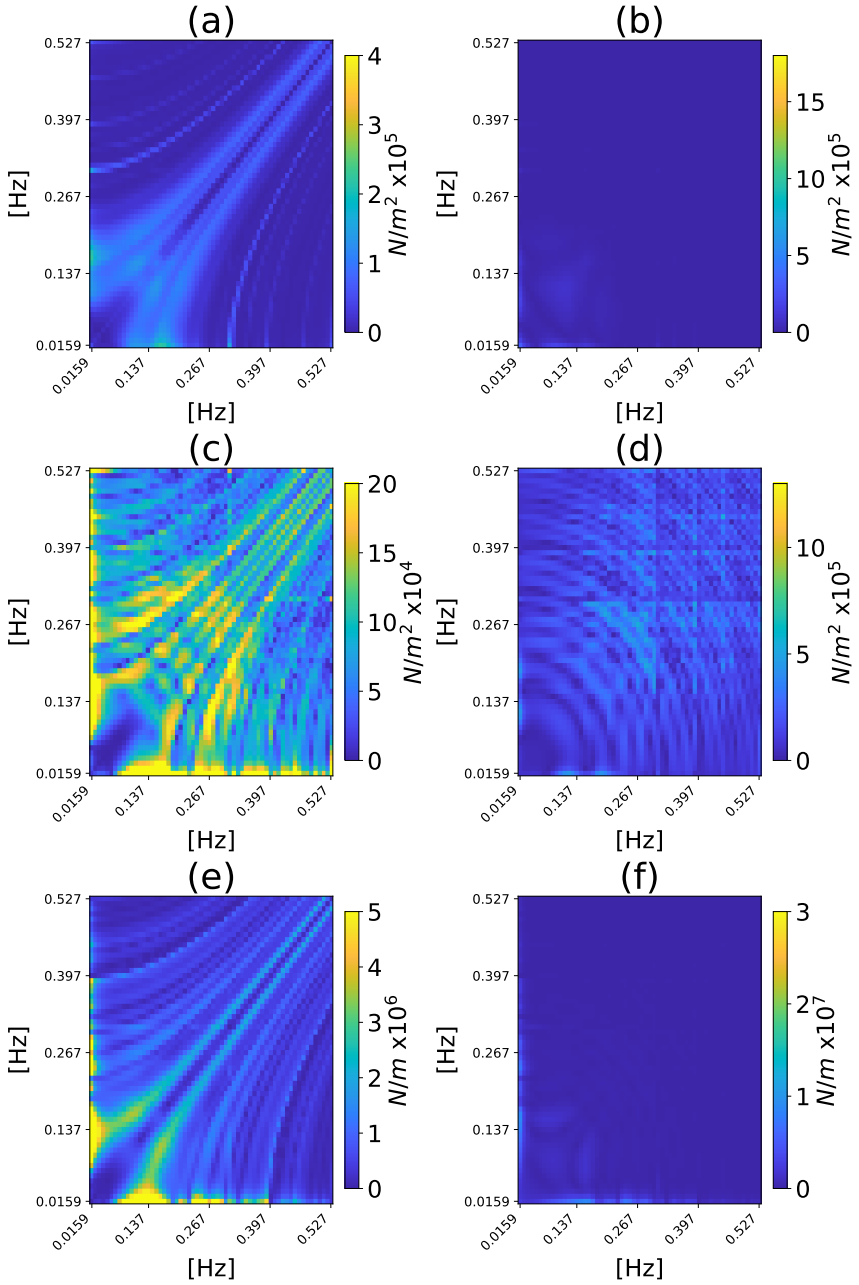

Figure 4.8: Quadratic transfer functions for the UMaine Volturn-US [62] reference platform calculated by AQWA for heave difference magnitude (a), heave sum magnitude (b), surge difference magnitude (c), surge sum magnitude (d), pitch difference magnitude (e), and pitch sum magnitude (f).

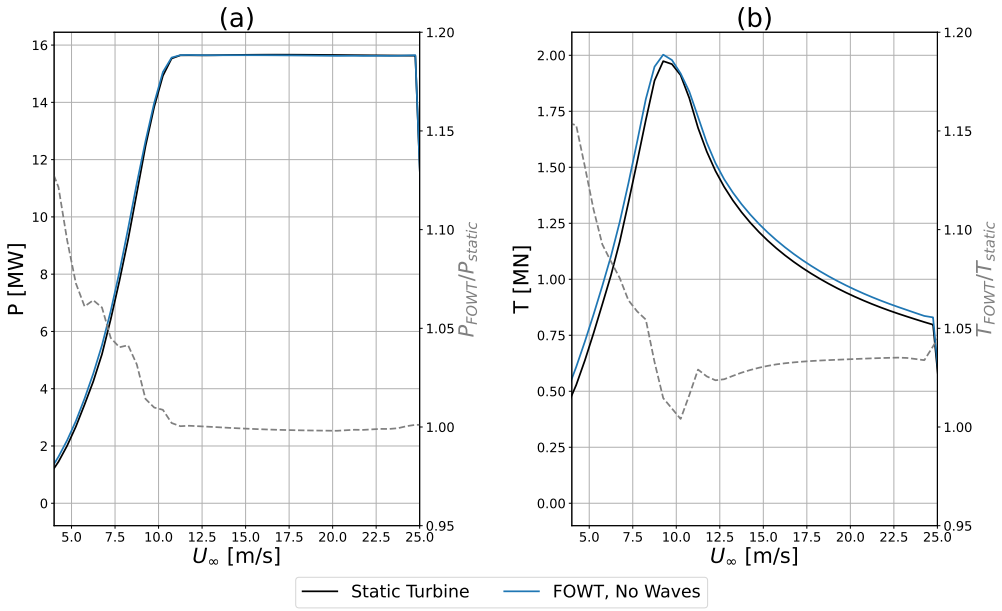

Figure 4.9: Power (a) and thrust (b) performance curves for the IEA 15 MW RWT [52] on the UMaine Volturn-US [62] semi-submersible floater with no wave loading, as well as with all degrees of freedom locked. Turbulence intensity is set to 6 %.

the feedback term used by the ROSCO controller's floating feedback module which damps platform pitch motion. As such, the lower acceleration just above rated causes a different controller behavior which allows slightly larger magnitudes of the range of platform pitch position. Even in this region, the platform pitch variation never exceeds 1.5 degrees.

We see similar power and thrust performance between the floating and static turbines. At the rated wind speed, power and thrust of the floating turbine are within 0.5 % of the static turbine. However, above and below rated wind speed, the performance of the floating turbine differs slightly. At low wind speeds, the floating turbine power capture outperforms that of the static turbine (5 % increase in power at 7 m/s). This is caused by fluctuations in wind speed due to turbulence causing some rotor motion in the freestream direction. This model predicts a beneficial effect for power capture, as shown in Chapter 3. The floating turbine also has a 5 - 15 % increased thrust relative to the static turbine across the operational wind speed regime. This additional rotor thrust is due to blade pitching to damp platform pitch motion. This blade pitching is carried out by the controller's floating feedback module, which aims to minimize nacelle fore-aft acceleration, and results in higher thrust forces that damp the pitch motion.

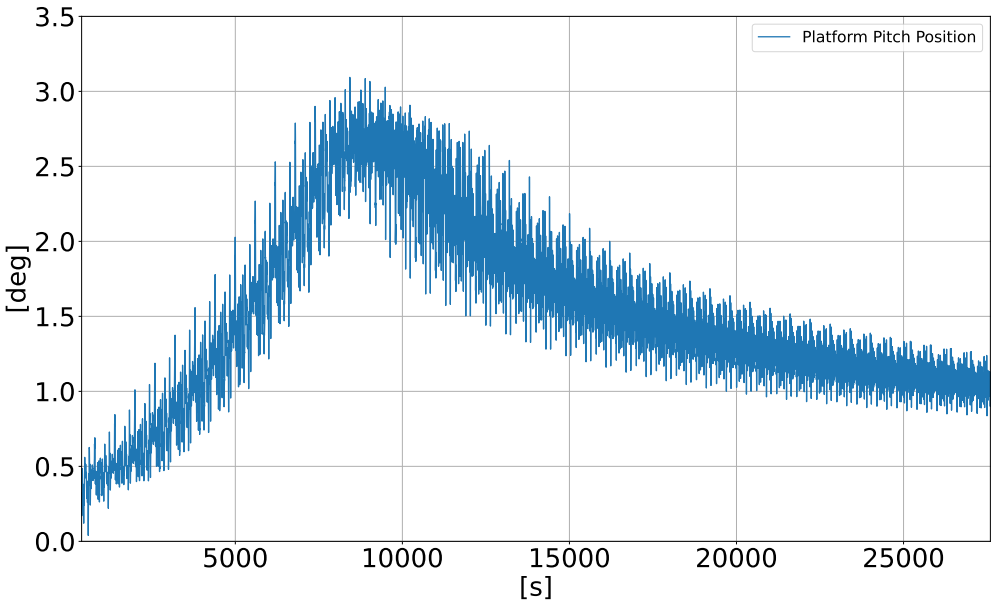

Figure 4.10: Platform pitch angle as a function of time during wind speed step test for the FOWT with no wave loading.

In addition to the average power and thrust performance, we show the fluctuation of power and thrust of both the static and floating turbine for varying turbulence intensities in Figure 4.11. We see for both the static and floating turbine that the fluctuation of power and thrust increases with turbulence intensity. Both power and thrust vary significantly due to wind speed turbulence. The 10^{th} to 90^{th} percentile range of thrust for the floating turbine at the rated wind speed is 13 % of the turbine rated thrust for a 6 % turbulence intensity and 32 % for a 14 % turbulence intensity. These values are 2 % and 5 % less than for the static turbine, respectively. The same is true at high wind speeds where the floating turbine experiences less thrust fluctuation due to wind speed turbulence. This effect is due to the platform motion of the FOWT. As wind speed increases and rotor thrust increases, the platform pitches backwards decreasing the wind speed experienced by the rotor and thus decreasing the rotor thrust. This has a small damping effect on the rotor thrust fluctuation due to turbulence.

We also see large fluctuations of turbine power. These fluctuations are bi-directional, increasing and decreasing power fairly symmetrically. As demonstrated in Figure 3.2, the turbine is not able to impose a hard cap on its generator power. The controller caps the generator torque, but aerodynamic torque is still able to vary based on wind speed and the collective blade pitch. If wind speed turbulence occurs at a time scale

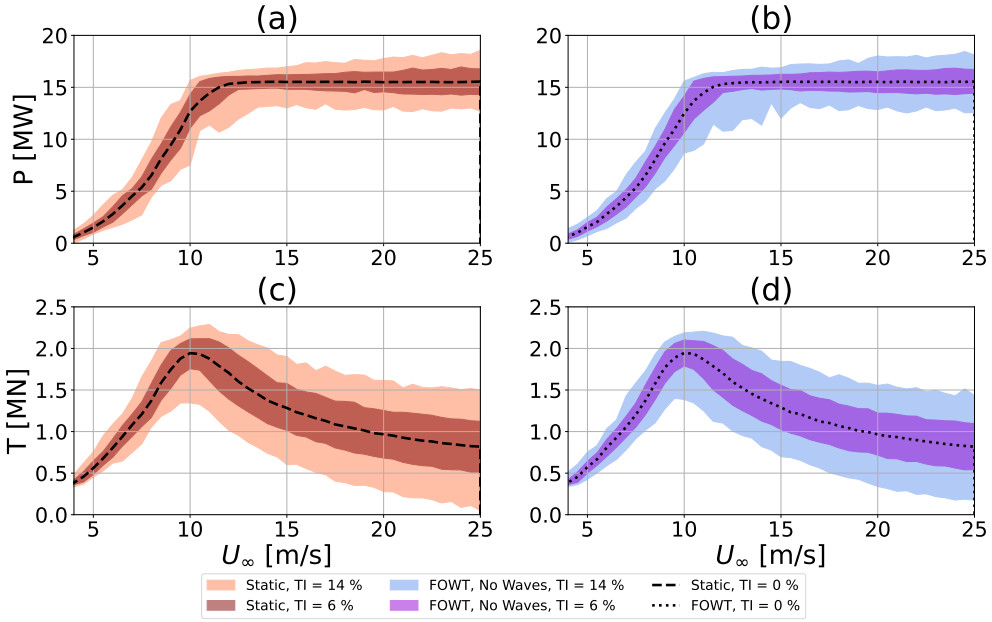

Figure 4.11: 10^{th} to 90^{th} percentile range of power (a and b), and thrust (c and d) for a static (a and c) and floating (b and d) turbine with varying turbulence intensities in still seas.

that is faster than the maximum speed of the blade pitch motors, then the aerodynamic torque will spike. The increased aerodynamic torque is not matched by the constant generator torque, so the rotor speed increases. This causes increases in generator power output beyond the rated turbine power. For the thrust fluctuations, the same can be true if the wind speed fluctuations due to turbulence are faster than the maximum speed of the blade pitch motors.

4.3.4 Turbine Response in Regular Waves

In order to assess the response of the IEA 15 MW RWT in regular waves, wind speed step tests between 5 and 24 m/s were run under a range of wave amplitudes and periods. The exact wind speeds, amplitudes, and periods simulated are shown in Table 4.4. Wave frequencies equal to 3 and 5 s were only simulated up to 1 m amplitude to satisfy the maximal average wave steepness criteria in ANSYS AQWA. The range of wind speeds was selected to cover the operational wind speed range of the reference turbine. As we are primarily interested in operational performance under regular wave loading, not turbine down time, wind speeds close to the cut-in and cut-out were omitted to avoid start-up or shut-down routines being implemented by the controller during simulation. The wave period and amplitude range were

Wind Speeds [m/s]	Wave Period [s]	Wave Frequency [Hz]	Wave Amplitude [m]
5	3	0.333	0.5
6	5	0.200	1
7	7	0.143	2
8	8	0.125	3
9	9	0.111	4
10	10	0.100	5
10.59	11	0.0909	
11	12	0.0833	
12	15	0.0667	
13	20	0.0500	
14	28	0.0357	
15	35	0.0286	
16			
20			
24			

Table 4.4: Range of wind and wave conditions simulated in regular wave analysis.

selected to cover the range of realistic operating conditions in representative turbine sites as proposed by Fontanella et al. 2024 [30] and Ahn and Shin 2020 [83]. This range was later confirmed to cover the range of operational conditions through the characterization of wind and wave conditions at four potential FOWT installation sites. This characterization is discussed in detail in Chapter 5. Additionally, a wave period of 28 s was included, as this period is close to the natural pitch frequency of the UMaine Volturn-US reference floater.

The motion response of the turbine can be characterized via response amplitude operators (RAOs) for the turbine - platform system. The system RAOs are computed via time domain simulation at a range of wave periods with a wave amplitude of 1 m. We compute the RAOs with no aerodynamic forcing, with aerodynamic forcing but no active control, and with full ROSCO control at the turbine rated wind speed. The RAOs, and RAOs computed with OpenFast as reported in the platform reference document [62], are shown in Figure 4.12. The reference RAOs are computed with a wind speed of zero and the blades pitched to feather to minimize any aerodynamic force, as opposed to our model which simply assumes all aerodynamic forces are zero. Additionally, OpenFast includes flexible blade modeling, where our model assumes that all turbine structures are rigid. However, as the wind speed is zero and rotor thrust is small, flexible blade versus rigid turbine modeling should not result in significant differences.

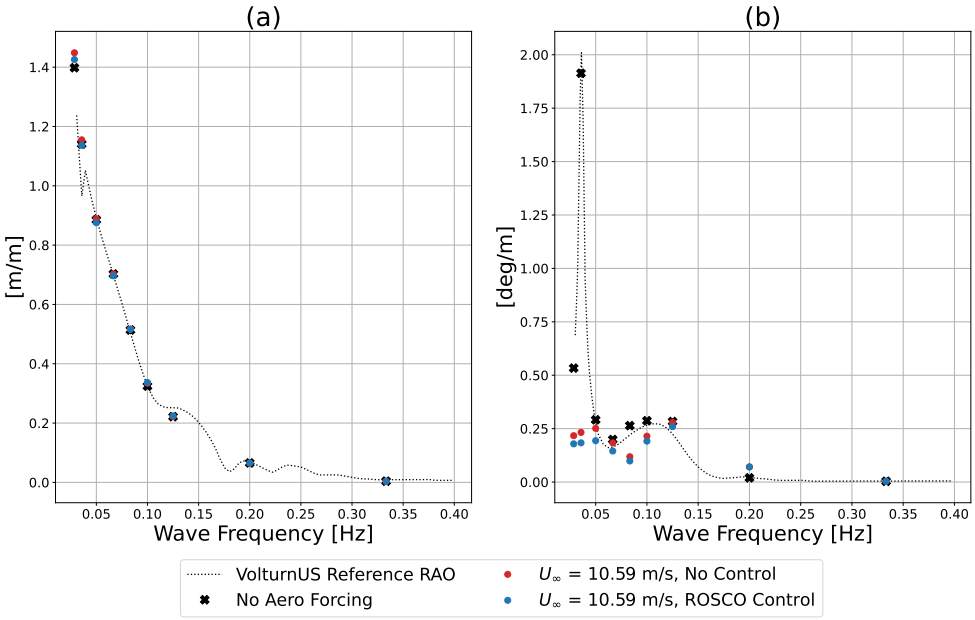

Figure 4.12: Response amplitude operators in surge (a) and pitch (b) motion for the IEA 15 MW RWT [52] coupled with the UMaine Volturn-US [62] floater. The reference RAOs for the floater, the RAOs with no aerodynamic forcing, with aerodynamic forcing and no active control, and with aerodynamic forcing with the ROSCO controller are shown.

We see good agreement between the RAOs without aerodynamic forcing computed by our coupled model and by OpenFast. At the pitch natural frequency of 0.0357 Hz, there is a 1.3 % difference between the two models in the pitch RAO. The inclusion of aerodynamic forcing has a significant damping effect on the pitch RAO (88 % reduction at the pitch natural frequency of 0.0357 Hz and 25 % reduction at 0.1 Hz), but a minimal effect on the surge RAO (1 % increase and 3 % increase at those same frequencies). This is due to the amplitude of surge motion being largely due to the wave forcing and platform mooring. The pitch motion is significantly affected by the turbine aerodynamic forcing. The inclusion of active control further damps the turbine pitch motion by 21 % at 0.0357 Hz and 11 % at 0.1 Hz. This is expected, as the ROSCO controller includes a floating feedback module which is designed to minimize platform pitch motions through collective blade pitch control.

Similar to the RAOs, we measure the amplitude of the relative velocity of the hub due to platform motion. The hub velocity due to surge motion is equal to the surge velocity of the platform center of gravity, while the hub velocity due to pitch is equal to the product of the platform pitch velocity and the distance between the center of gravity and the turbine hub. The hub velocity amplitude due to surge and pitch

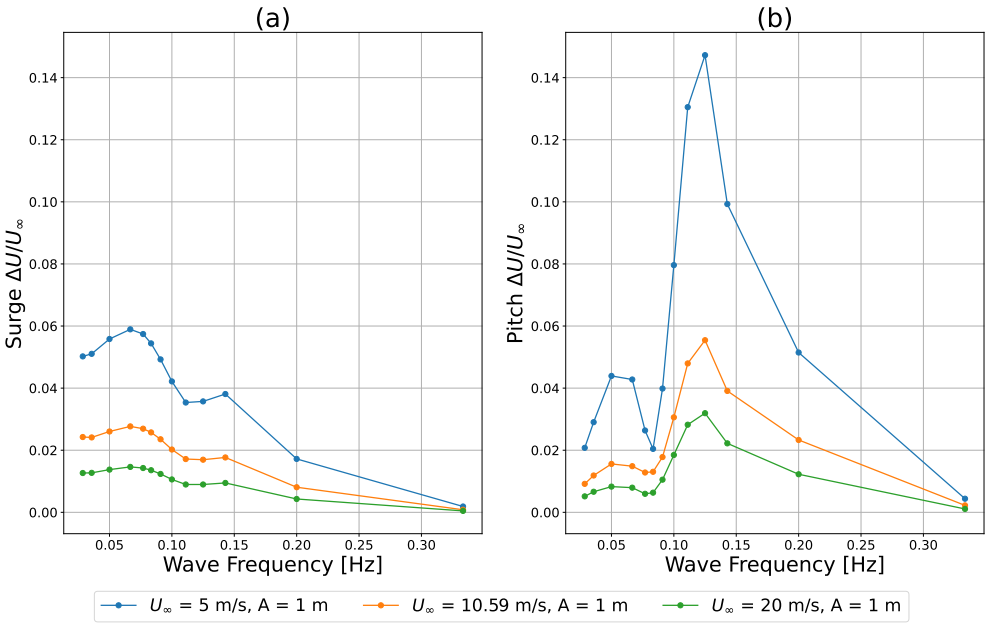

Figure 4.13: Amplitude of the velocity due to platform motion over one wave period in surge (a) and pitch (b) as a function of incoming wave frequency for a 1 m amplitude wave. All values are normalized by the freestream wind speed.

platform motion is shown in Figure 4.13.

The peak, normalized hub velocity caused by pitch motion is between two and two and a half times larger than that caused by surge motion, depending on wind speed. The maximum hub velocity due to surge occurs at 0.0667 Hz (15 s period) for all wind speeds. This peak occurs at a relatively low frequency where the motion amplitude due to surge is high. However, unlike the surge position RAO, the surge velocity RAO does not increase as the frequency approaches zero. Once wave frequency becomes sufficiently low, the speed of surge motion, and thus hub velocity, decreases. The hub velocity due to pitch peaks for 0.125 Hz wave frequency (8 s period). This coincides with a local maxima in the pitch RAO. There is a secondary peak in the hub velocity due to pitch motion near the pitch natural frequency of the platform (0.0357 Hz frequency or 28 s period). However, aerodynamic damping, and the slow velocity of pitch at the lower frequency decrease the hub velocity relative to the maximum at 0.125 Hz. As the platform velocity responses are normalized by the freestream wind velocity, the response signals are larger for lower wind speeds. When the response is not normalized by wind velocity, the platform surge velocities across the three wind speeds are within 7 % of each other, and the platform pitch velocities are within 30 %. This suggests that surge motion velocity is largely unaffected by wind speed, and

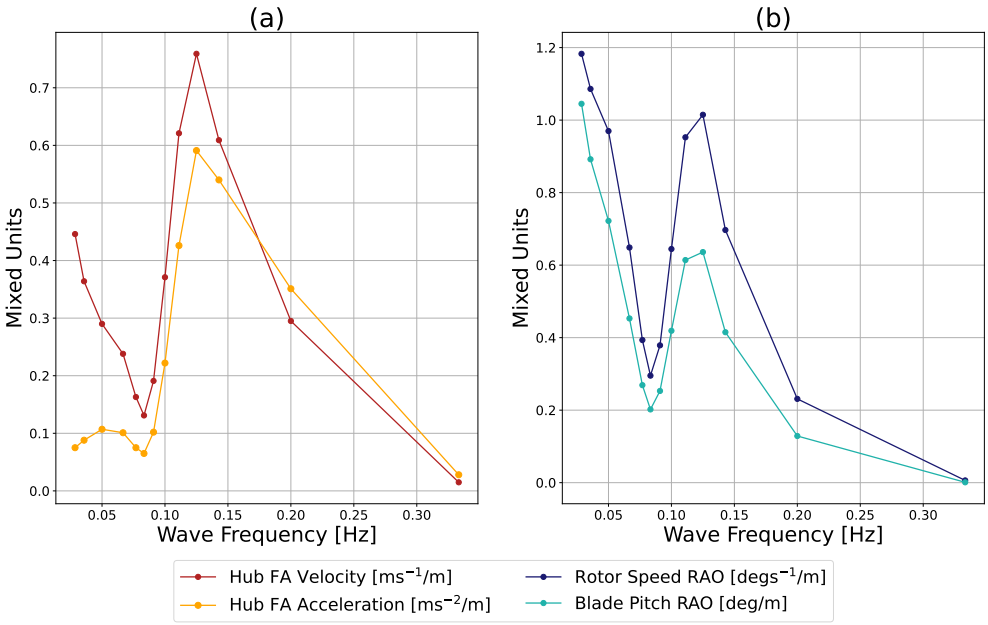

Figure 4.14: Response amplitude operators of the hub fore-aft velocity and acceleration (a) and turbine blade pitch and rotor speed (b).

largely due to wave loading, while pitch motion velocity is a function of both wind and wave loading.

In addition to the platform surge and pitch motion RAOs, we show the motion response of the turbine hub in the streamwise, or fore-aft, direction as well as the turbine collective blade pitch and rotor speed responses in Figure 4.14. These are obtained via time domain simulation of turbine performance at the rated wind speed, with full control, with incident regular waves of 1 m amplitude and varying frequency. The turbine hub fore-aft velocity is the additional wind speed added to the free stream velocity by platform motion. The hub velocity amplitude peaks at 0.125 Hz, the frequency of the maximum platform pitch motion response. There is also a secondary peak for low frequencies where the platform surge RAO is large. The hub acceleration peaks strongly at the frequency of the maximum platform pitch response. Hub fore-aft acceleration is used as a proportional feedback term by the ROSCO floating feedback controller, indicating that the controller will strongly actuate the blade pitch at this frequency. Both the turbine rotor speed and blade pitch amplitudes closely follow the hub velocity response.

The average and fluctuating components of turbine thrust and generator power as a function of the incoming regular wave frequency are shown in Figure 4.15. The results are normalized by static turbine performance. We show turbine performance

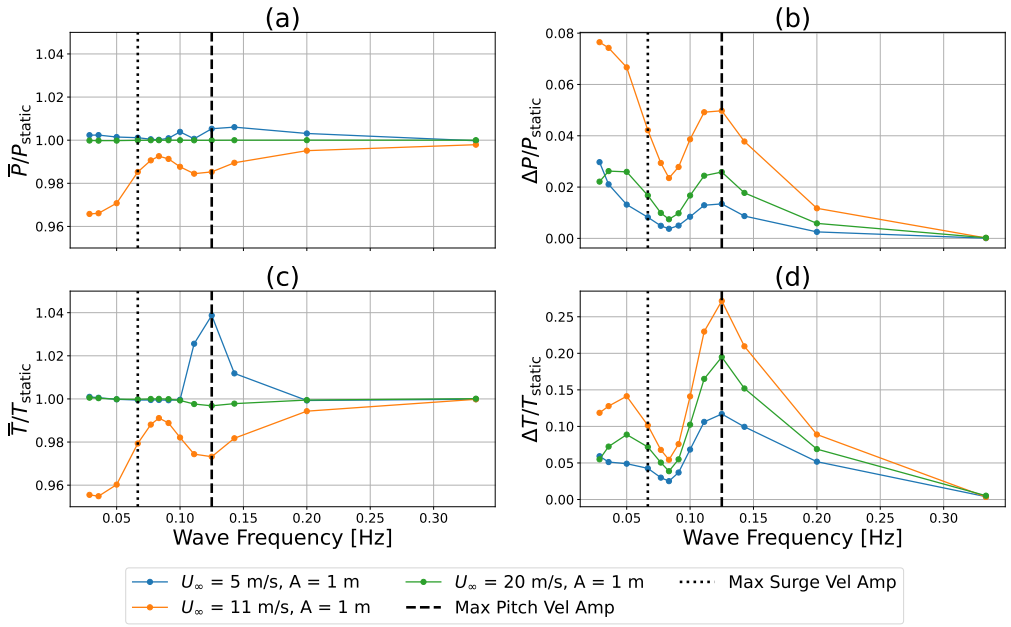

Figure 4.15: Average power (a), the amplitude of power (b), average thrust (c), and the amplitude of thrust (d) over one wave period at below rated, rated, and above rated wind speeds as a function of incoming wave frequency. All values are normalized by the static turbine power or thrust at that wind speed.

across the range of wave frequencies for three representative wind speeds. A similar trend as that seen in Chapter 3 arises where average power capture is increased at below-rated wind speeds and decreased around rated wind speeds relative to a static turbine. Also similar to the results of Chapter 3, the average power and thrust above the rated wind speed return to the static turbine values.

Unlike the prescribed harmonic motion results obtained with no hydrodynamic modeling, there is a frequency dependence for both average and fluctuating components of power and thrust. The average power capture at 5 m/s wind speed peaks for 0.143 Hz (7 s period). This frequency is slightly larger than the frequency at which the maximum pitch velocity is induced. This is due to the influence of the controller's floating feedback module which limits nacelle fore-aft acceleration caused by large platform pitch motions. The floating feedback module varies the collective blade pitch angle, damping platform pitch motion but decreasing power capture and increasing thrust. As such, the maximum average power capture does not coincide with the maximum hub velocity due to platform motion. In contrast, the maximum increase in average thrust does coincide with the maximum platform pitch velocity. The average power capture at the near-rated wind speed of 11 m/s reaches the same minima value near both the maximum platform pitch velocity and maximum platform

surge velocity. Power capture at this wind speed is minimum for very low frequency waves, corresponding to regions of large surge motion excitation as seen in the platform surge RAO. At the above rated wind speed, power capture and thrust are close to the fixed-bottom turbine baseline for all wave frequencies.

The fluctuating components of power and thrust for all wind speeds have peaks at the frequency of maximum platform pitch velocity, as well as in the low-frequency, surge motion dominated, region. Average and fluctuating components of power and thrust for the FOWT vary the most relative to the static baseline in regions where the RAO including aerodynamic forcing predicts maximal response amplitudes. Both the low frequency region where the surge RAO is maximal, and the peak in the pitch RAO near 0.125 Hz, are seen to affect FOWT performance significantly.

In order to demonstrate the effect of wave amplitude on turbine performance, the average and fluctuating components of turbine power and thrust for a representative wave frequency of 11 s and varying amplitude waves are shown in Figure 4.16. The fluctuating components of power and thrust increase close to linearly with wave amplitude. Notably, the fluctuating component of thrust reaches over 70 % of the static turbine thrust for a 5 m wave at the rated wind speed. As the rated wind speed is where the highest turbine thrust occurs, this represents a large magnitude of thrust fluctuation. This type of large thrust fluctuation will have serious implications for blade fatigue, and thus effective component life. The fluctuation of power capture varies up to 14 % of the static value. The average components of power and thrust are non-linear with amplitude, due to the turbine controller, which maximizes power and limits thrust. The relationship between average power and incoming wave amplitude at the below rated wind speed can be approximated with a cubic relationship to a value of the coefficient of determination $R^2 = 0.996$, signifying a very good fit. The decrease in power capture at the rated wind speed decreases roughly linearly with wave amplitude. The decrease in power capture at rated is due to the controller, which limits the turbine to its maximum generator torque when platform motion causes the wind speed at the rotor to increase above the rated wind speed. As the amplitude of the power response increases, more power is lost in the below rated region, while power is capped in the above rated region. As such, the loss of average power scales closely with the fluctuation of power. At the above-rated wind speed, average power capture is close to the static turbine baseline for all wave amplitudes. Average thrust is decreased relative to the static baseline by up to 2 % at the 5 m wave amplitude.

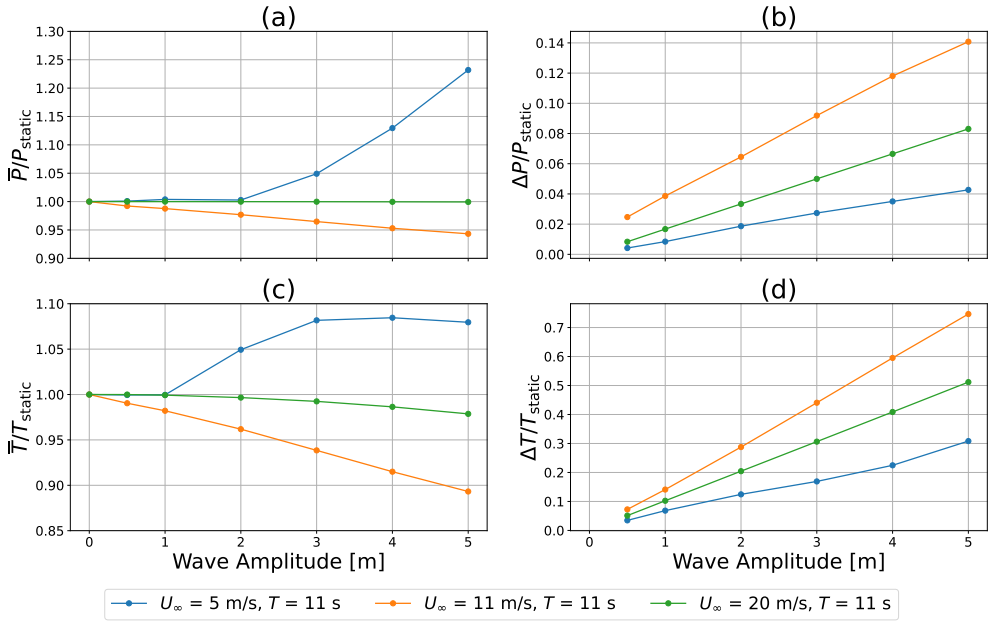

Figure 4.16: Average power (a), the amplitude of power (b), average thrust (c), and the amplitude of thrust (d) over one wave period at below rated, rated, and above rated wind speeds as a function of incoming wave amplitude. All values are normalized by the static turbine power or thrust at that wind speed.

We also considered a subset of cases in which the incident wave angle and incident wind directions were varied to examine the effect of misaligned wind and waves on the reference platform. Fontanella et al. [30] identified 90-degree incident waves as being deleterious to power capture in the below rated region, as wave-induced platform motion does not cause rotor motion in the free stream wind direction. We also identify 15-degree incident waves as being of interest as that angle results in asymmetry of the distance of the platform's three columns to the line of incident waves. This asymmetry may cause some variable hydrostatic and hydrodynamic forces compared to the symmetric zero-degree heading case.

Turbine performance with zero degree heading wind and 1 m amplitude regular waves of varying frequency at zero, 15, and 90 degree heading at 5 m/s is shown in Figure 4.17. Turbine performance under the same wave loading and 11 m/s wind speed is shown in Figure 4.18. Performance at high wind speeds is not presented as the average turbine power and thrust are approximately the same as the static turbine baseline. As discussed previously, regular wave loading at zero-degree heading and 5 m/s wind speed generally increases turbine power capture and rotor thrust compared to a static turbine baseline. As the incident wave angle is varied, the effects of wave-induced platform motion are effectively damped. The 15-degree heading waves

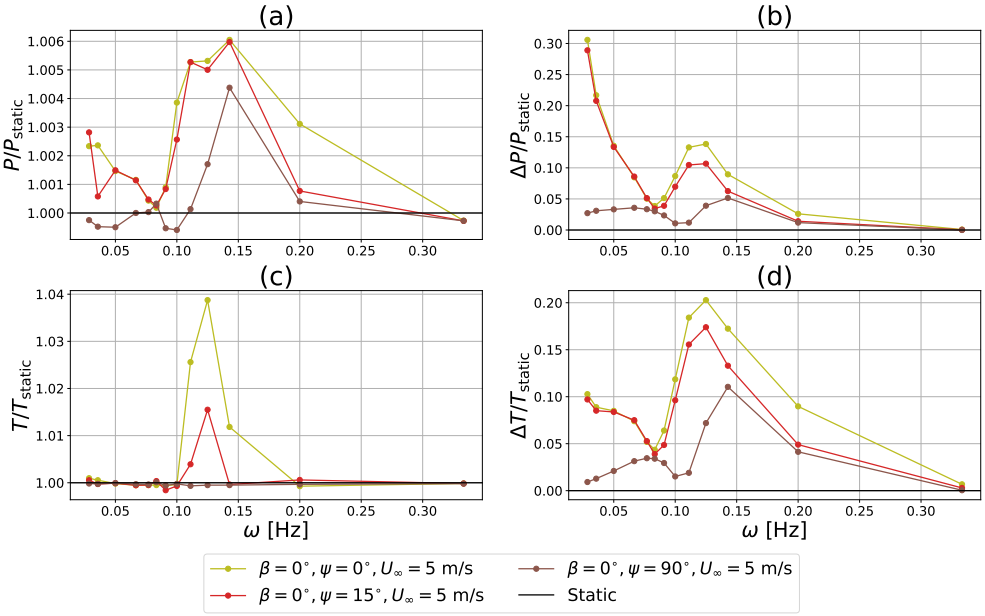

Figure 4.17: Average power (a), the amplitude of power (b), average thrust (c), and the amplitude of thrust (d) over one wave period at 5 m/s wind speed with 1 m amplitude regular waves of varying frequency and heading. β and ψ are the angles of incident wind and waves respectively.

have a slightly smaller effect than the zero-degree heading. 90-degree heading waves induce significantly less motion effect. As proposed by Fontanella et al., as waves induce platform motion that does not cause streamwise rotor motion, the effect on rotor performance is minimized. However, even for 90-degree incident waves there is some effect on average power, power amplitude, and thrust amplitude. This is due to wind forces inducing some platform pitch and surge motion, an effect described in the simulation of the FOWT in still seas presented in Section 4.3.3.

At the 11 m/s wind speed, average turbine power capture and rotor thrust is generally decreased by regular waves compared to the static turbine baseline. Similar to the 5 m/s wind speed, variation of the incident wave angle from zero to 90 degrees decreases the effect of regular wave loading. In the fluctuating component of power and rotor thrust, the peak frequency is shifted. The amplitude of power and thrust is correlated to the platform motion response. The platform sway and roll response have different peak frequencies in their RAOs than pitch and surge. As the waves induce more sway and roll motion, the frequencies of peak turbine power and thrust amplitude shift.

In order to assess the effect of both wind and wave misalignment from the zero-degree heading, we show the effect on power capture of varying wind and wave head-

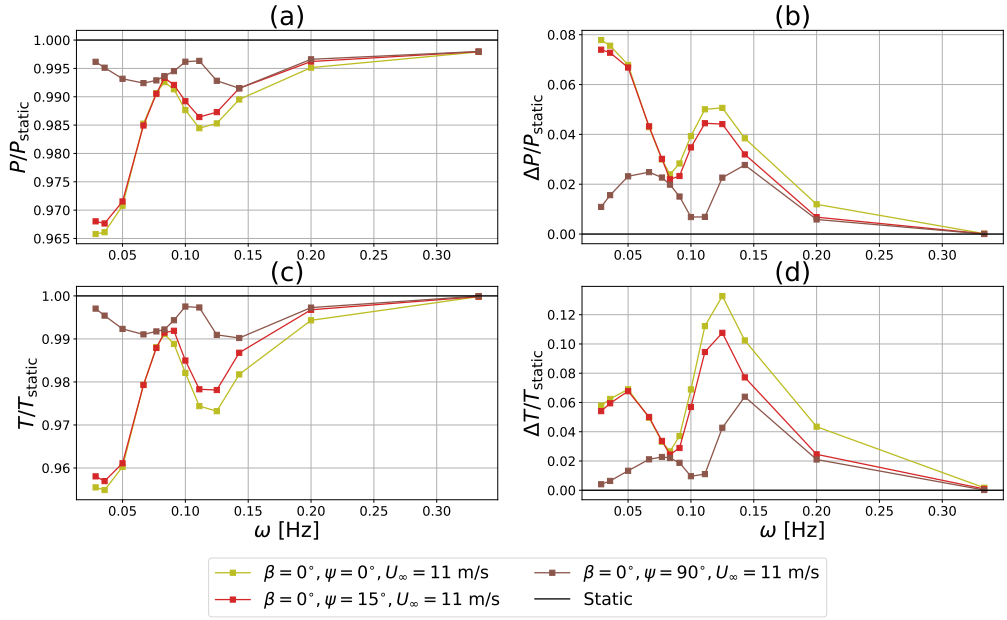

Figure 4.18: Average power (a), the amplitude of power (b), average thrust (c), and the amplitude of thrust (d) over one wave period at 11 m/s wind speed with 1 m amplitude regular waves of varying frequency and heading. β and ψ are the angles of incident wind and waves respectively.

ings at 5 and 11 m/s wind speed in Figure 4.19. As discussed above, increased misalignment between the wind and wave heading results in the effect of motion on turbine power capture being decreased. This result supports the findings presented by Fontanella et al. [30]. As the wind direction is varied to match the wave direction, we see a return towards the increased power capture at the below-rated wind speed. At the near-rated wind speed, aligned wind and waves from 15 and 90 degree headings decrease turbine performance more than aligned wind and waves at zero degree heading. This is due to increased platform rotational motion in the streamwise direction for 90 degree wave heading relative to zero degree wave heading. We believe this is an attribute of the mooring system, but any design variation of the mooring to minimize this effect is not explored here. These findings emphasize the importance of choosing a correct mooring orientation that takes into account the most prevalent incident wave angles. Additionally, we do not see a strong effect of the platform asymmetry theorized for 15-degree wave heading.

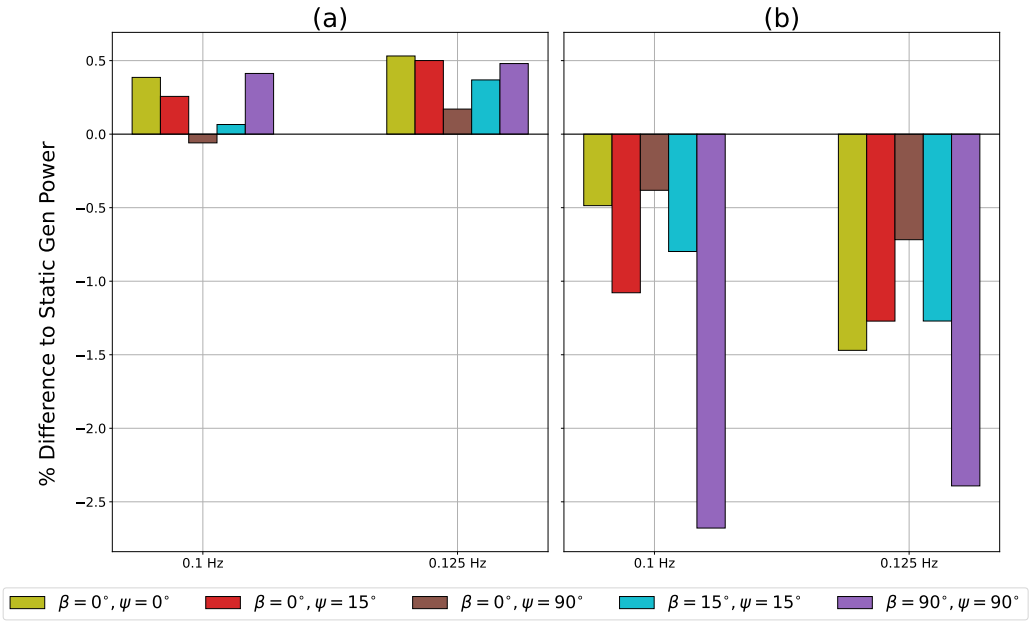

Figure 4.19: Power capture relative to the static turbine baseline under 1 m amplitude regular wave loading at two frequencies with varying wind and wave direction at 5 m/s (a) and 11 m/s (b) wind speed. β and ψ are the angles of incident wind and waves respectively.

4.4 Discussion and Conclusions

With the coupled aero-hydrodynamic model presented, we examined the performance of a representative, large FOWT under regular wave loading. Our coupled model predicts that wind and wave aligned loading at a zero-degree heading will increase average power capture when the wind speed is below rated, decrease average power capture when the wind speed is near rated, and have a small effect on average power capture when the wind speed is significantly above rated. These general trends are the same as those presented in Chapter 3 which modeled prescribed harmonic motion.

Additionally, we find that turbine performance is dependent on the regular wave frequency, with frequencies corresponding to the local maxima in the floating platform RAO causing a greater change in turbine performance. 0.125 Hz is identified as causing maximal fluctuations in turbine power and thrust as well as being a local maxima for regular wave loading's effect on average power and thrust for this specific floating platform and turbine. We also show that the amplitude of turbine power and thrust scales linearly with regular wave amplitude. In contrast, average power capture and average thrust can exhibit non-linear behavior driven by the turbine controller. Average power capture in the below rated region is shown to scale close to cubically

with wave amplitude.

Examining the effect of wind and wave misalignment on turbine performance, we found through regular wave testing that wind and wave aligned conditions at zero degree heading at below-rated wind speeds enhance FOWT power capture. However, if wind and waves are misaligned relative to each other, this decreases the observed power enhancement effect. Additionally, wind and waves coming from a 90-degree heading relative to the platform induced greater decreases in power capture at the rated wind speed relative to waves coming from a zero degree heading. We conclude that misalignment between wind and waves is detrimental to turbine average power capture in the below rated wind speed region, and wind-wave misalignment from the zero degree heading can be detrimental to turbine average power capture in the near rated wind speed region.

These results provide a framework through which we will study FOWT performance in more realistic sea-states. By identifying wave frequencies at which the platform and turbine response will be the largest, and characterizing trends in turbine performance according to wave amplitude, we will be able to analyze and understand turbine performance in irregular wave loading. We also connect the turbine performance response in regular waves to the platform, and coupled platform-turbine, response amplitude operators. This correlation of peaks in the turbine performance response with peaks in the platform RAO confirms that FOWT performance is strongly dependent on platform motion. Finally, our identification of regular wave frequencies that induce strong turbine performance effects will aid in further exploration of platform and turbine design around those key wave frequencies.

Chapter 5

Comparison of FOWT Performance in Four Case Study Locations in the United States and United Kingdom

5.1 Introduction

A key design variable in offshore wind energy is site selection. There has been significant effort to develop a methodology for optimizing wind farm site selection for FOWT or offshore wind turbine installation. Many of these rely on Geographic Information Systems (GIS) which consider the wind resource, protected areas, other coastal resources, and transmission costs as a function of location. Optimal sites for wind farm placement are identified by comparing maps or distributions of these criteria to minimize the levelized cost of energy (LCOE) within the existing geographical constraints [69, 68]. Power generation from a potential wind turbine is estimated by combining the rated power curve and the local wind speed distribution. This methodology does not take into account the effect of varying floating platform decisions, or the possibility of loss of operating time due to wave-induced motion.

Another class of site selection methods utilizes decision-making algorithms which incorporate data such as depth, distance from ports and substations, tides, and typical sea state conditions [84]. Finally, there exist combinations of these two methods which leverage both GIS and decision-making models [85]. Despite this, there does not exist a comprehensive methodology with which to understand the effects on power production due to wave-induced motion in FOWTs versus fixed turbines. With the coupled model presented in Chapter 4 we aim to predict FOWT performance over a

long time scale as the installation site is varied and to compare that to static turbine performance.

It is common to use coupled models, such as the model presented in Chapter 4, to evaluate turbine performance at a specific site location. Cottura et al [29] present a coupled potential flow and BEMT model. The authors used this model to determine power output and LCOE of the NREL 5MW reference turbine in the Mediterranean sea. Characterizing wind and wave conditions with a bucket sort algorithm and ERA 5 reanalysis data of three years, and assuming wind and waves at zero-degree heading, they predict a capacity factor of around 45 percent and a LCOE of roughly 130 euros per MWh. This work examines a single site, and the assumption of aligned wind and waves with a zero-degree heading will likely significantly alter results compared to a full, misaligned sea state.

Also discussed in Chapter 4, Fontanella et al. 2024 [30] utilize OpenFast to simulate the IEA 15 MW RWT and NREL 5 MW RWT in the Mediterranean Sea. Wind and wave data are extracted from ERA 5 reanalysis data of one year and characterized via a K-means algorithm. The K-means algorithm sorts the data set into clusters which are each described by a single data point which is the geometric centroid of the cluster. Wind and wave heading, wind shear, and turbulence are all taken into account. The authors generate site-specific power curves and predict AEP of the turbines coupled with both a spar and semi-submersible platform. The AEP of the 15 MW RWT is predicted to decrease by 0.62 % and 1.17 % compared to a static turbine for the semi-sub and spar platform respectively. Their work examines a single site, so comparisons of the effect of site-specific sea states are not possible.

In addition to predicting floating turbine power performance relative to a fixed-bottom turbine, we will also characterize turbine loading and the fluctuation of turbine loads. Fatigue damage has been identified as a failure mechanism in wind turbine blades [86]. Ravikumar et al. [87] also identify fatigue damage induced crack growth as a common cause of wind turbine blade failure. Furthermore, Ravikumar et al. identify fluctuations in wind speed at the rotor, and thus fluctuating loads on the rotor, as a contributor to increased fatigue damage.

Saenz-Aguirre et al. [88] simulated the loads on a floating 5 MW turbine at the Hywind Scotland floating wind farm site. The authors used a rainflow counting algorithm to determine the number of load cycles the turbine was exposed to, and the S-N curve for the turbine tower to determine 30-year fatigue damage loads. Their model found that the tower base was exposed to 145 to 148 % larger fatigue damage equivalent loads under wave loading compared to without the load fluctuations caused

by wave-induced platform motion. In this work, we do not present fatigue damage loads for the reference wind turbine or platform. However, we consider turbine load fluctuations to be a proxy for fatigue damage.

Our aim is to predict FOWT performance relative to that of a static turbine over a range of possible installation sites. Different installation sites could have significantly different typical combined wind and sea state conditions, resulting in varying floating turbine performance. We will also isolate and examine the effect of wind-wave misalignment in irregular seas. We aim to examine and quantify the effect of wind and wave induced motion on turbine performance. As such, we compare FOWT performance to static performance in sites which could conceivably host either technology. Lopez et al. 2022 [89] identify regions of FOWT and fixed turbine viability on the east coast of the United States. Multiple regions identified for floating or fixed development directly border one another. We aim to examine the intermediate zones that exist in these regions where either technology would be feasible. Cavazzi and Dutton 2016 [90] identify sites of low potential LCOE around the British Isles for FOWT deployment. Additionally, they present estimation of turbine foundation cost as a function of water depth. The cost of floating foundations and jacket type fixed foundations are found to be roughly equivalent at depths of 60-80 m. We identify regions highlighted by both Lopez et al. and Cavazzi and Dutton which have a water depth of 60-80 m. Additionally, we preference regions in which the US or UK government have conducted leasing activities for wind farm development. Through this methodology we identify four case study regions, two in the United States and two in the United Kingdom. The UK sites are located at the ScotWind Ossian FOWT lease site and the Celtic Sea PDA 1 lease site. The US sites are located at the New York OCS-A 0537 lease site and off the coast of North Carolina. The Carolina Coast site has not been identified for wind energy leasing activities, but meets the other requirements of our search.

5.2 Methods

The coupled model described in Chapter 4 is utilized to conduct four case studies examining the performance of the IEA 15 MW RWT in two locations in the United Kingdom and two locations in the United States.

Type	Chain Catenary
Line Type	R3 Studless Mooring Chain
Number of Lines	3
Fairlead Depth	14m
Anchor Depth	70 m
Anchor Radial Spacing	330 m
Nominal Chain Diameter	185 mm
Dry Line Linear Density	685 kg/m
Extensional Stiffness	3270 MN
Unstretched Length	300.68 m
Normal Added Mass	1
Tangential Added Mass	1
Normal Drag	2
Tangential Drag	1.15

Table 5.1: Characteristics of the adjusted Volturn-US [62] mooring system from Pillai et al. [91].

5.2.1 Adjusted Mooring Model

The model is unchanged from the previous section, apart from a modification to the mooring configuration. We aim to examine case study locations in which the mean water depth is at an intermediate range feasible for either fixed bottom or floating turbine application. For the case studies conducted, we targeted an average water depth of 70 m, so the original mooring system designed for the UMaine VolturnUS platform and 200 m water depth is unsuitable. As such, we modify the mooring system model described in Chapter 4 Table 4.3. Pillai et al. 2022 [91] test three mooring systems with varying mooring line length and anchor radius for the UMaine VolturnUS floater in 70 m water depth using a coupled aero-hydro-servo-elastic model in OrcaFlex. Based on the results of Pillai et al. we select the intermediate sized mooring design. The intermediate mooring footprint was shown to limit platform excursion to under 25 m as required for the turbine umbilical line [62], and to limit line tension to 60 % of the chain minimum breaking load as suggested by the American Petroleum Institute standards for floating offshore structures [92], while minimizing chain length, and therefore cost of the system. The characteristics of the adjusted mooring system are shown in Table 5.1.

u_{100}	100 m u-component of wind
v_{100}	100 m v-component of wind
ψ	mean wave direction
H_s	significant height of combined wind waves and swell
T	mean wave period

Table 5.2: Description of environmental variables extracted from ERA 5 [78] reanalysis data set to characterize conditions in case study locations.

5.2.2 Characterization of Environmental Conditions

To characterize the conditions at the four case study locations, we utilize the ERA 5 reanalysis data set [93] available from the Copernicus Climate Change Service Climate Data Store. Data from 2024 (the most recent full calendar year of reanalysis data) was taken at hourly time points. In order to characterize the conditions in each case study location, both wind and wave data were extracted. A summary of the variables examined is shown in Table 5.2.

From these variables, a five-dimensional vector is created that describes the environmental conditions at each hourly time step.

$$x_i = [U_\infty, \beta, \psi, T, H_\mathrm{s}]. \tag{5.1}$$

i represents the specific data point, U_∞ and β are the mean wind speed and the mean wind speed direction at the turbine hub height computed from the u and v components of wind. ψ is the mean wave direction, T is the mean wave period, and H_s is the significant wave height. The environmental parameters in relation to the reference platform are shown in Figure 5.1. Although the low-fidelity coupled model presented here is significantly more computationally efficient than high-fidelity coupled models, direct simulation of the entire year of data is still impractical. We utilize the SKLearns python tool kit [94] to conduct an Expectation-Maximization (EM) algorithm [95] to achieve a Gaussian Mixture Model (GMM) clustering which characterizes the most common combinations of our five environmental parameters. A similar technique is utilized by Marcille et al. [96] and Ricciotti et al. [97] to characterize sea state and wind resource data sets.

The GMM clustering technique models the data set as a mixture of a discrete number of Gaussian distributions. A data set $\mathcal{D}$ can thus be represented as follows:

$$\mathcal{D} = \Sigma_{k=1}^{K} \pi_k \times \mathcal{N}(x_i \mid \mu_k, \Sigma_k), \tag{5.2}$$

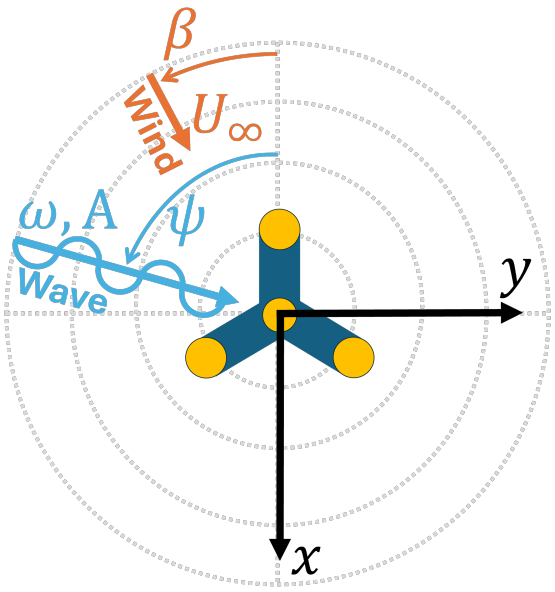

Figure 5.1: Wind direction (β) and wave direction (ψ) in relation to the floating reference platform and global x and y axes. Platform diagram is not to scale.

where K is a discrete number representing the number of distributions, π_k is the mixing probability of the k^{th} Gaussian, and $\mathcal{N}(x_i \mid \mu_k, \Sigma_k)$ is the k^{th} Gaussian distribution with mean μ_k and covariance Σ_k. The probability of an individual data point x_i belonging to the cluster C_k is expressed as:

$$P\left(x_i \in C_k\right) = \frac{\pi_k \times \mathcal{N}(x_i \mid \mu_k, \Sigma_k)}{\Sigma_{k=1}^{K} \mathcal{N}(x_i \mid \mu_k, \Sigma_k)}. \tag{5.3}$$

This technique offers some advantages to other clustering techniques, such as K-Means utilized by Fontanella et al. [30]. The GMM model allows for soft clustering, so that a single data point can be contained within the probabilistic cluster of two different distributions. Additionally, Euclidean clustering models like K-means assume spherical clusters. Environmental variables such as wind speed, wave height, and wave period are better represented by Gaussian distributions, as opposed to a distribution where points far away from the mean are equally likely to occur as those close to the mean.

To determine the optimal number of clusters K to characterize the data set for each case study location, we use the Bayesian Information Criteria (BIC) [98] expressed as

$$BIC = -2\ln(L) + c\ln(n), \tag{5.4}$$

where c is the number of free parameters, n is the number of data points, and L is the maximum likelihood of the model. The maximum likelihood L is expressed as

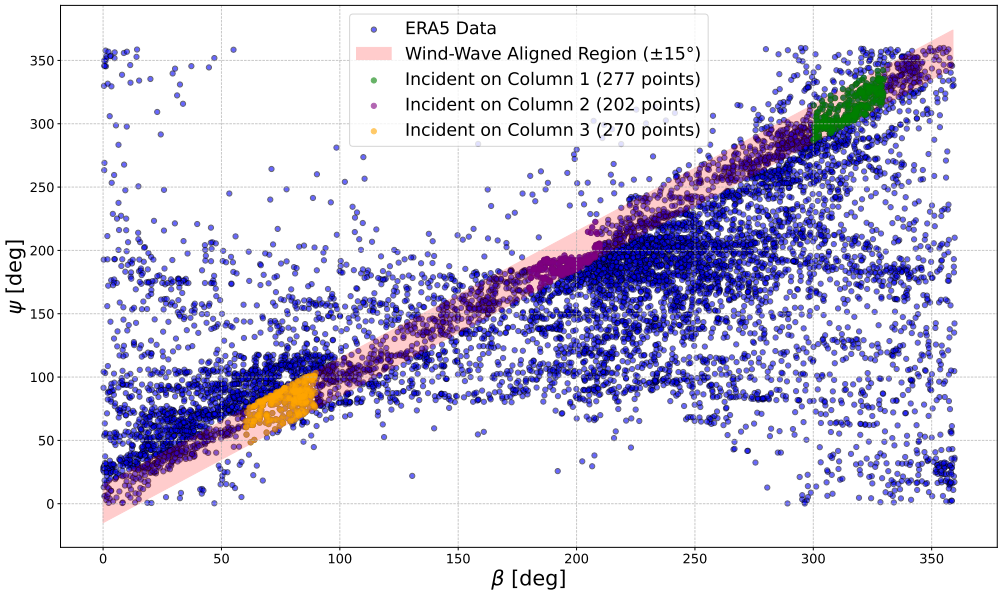

Figure 5.2: Wind direction (β) versus wave direction (ψ) for the ScotWind Ossian lease site. Wind and wave aligned conditions, as well as wind wave aligned conditions which are incident within +/- 15 degrees towards the three platform columns are highlighted.

follows:

$$\ln(L) = \sum_{i=1}^{n} \ln \left(\sum_{k=1}^{K} \pi_k \cdot \mathcal{N}(x_i \mid \mu_k, \Sigma_k) \right), \tag{5.5}$$

where K is the number of clusters. The BIC rewards better fit of the data set represented by $\ln(L)$ while penalizing model complexity represented by $c \ln(n)$.

A subset of the ERA 5 data set, as well as the entire set, is analyzed. First, we select for the simplest modeling case, in which both the wind and wave direction are aligned with one of the three platform radial columns within 15 degrees to either side. For our first set of simulations, we assume that these data points can be modeled as wind and wave aligned conditions at zero degree heading. This assumption is possible based on the platform's 120 degree rotational symmetry and an assumption that the turbine is able to perfectly yaw for each hourly data point. As an example, the subset of data extracted for these wind and wave aligned simulations for the ScotWind Ossian case study site is plotted in Figure 5.2. Data points within the "aligned region" are wind and wave aligned within 15 degrees, and those that fall into the three highlighted subregions are wind and wave aligned as well as incident upon a platform column. As wind and waves are aligned and assumed to be coming from a single heading, we are able to flatten our data set to three dimensions, omitting wind and wave direction.

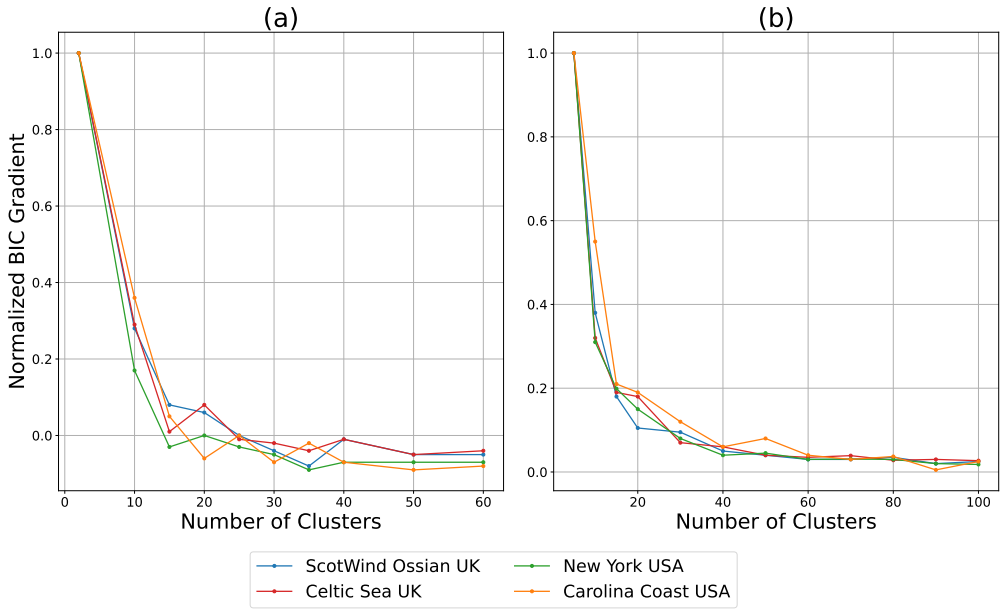

Figure 5.3: Bayesian information criteria (BIC) versus number of clusters for the flattened three dimensional data set (a), and for the full five dimensional data set (b).

The second set of simulations allows wind and wave direction to vary independently and includes the entire data set. By comparing the wind and wave aligned subset to the full data set, we are able to isolate and analyze the effects of misaligned wind and wave conditions. As such, the entire five-dimensional data set is clustered, and the aero-hydrodynamic model allows for any wave direction or wind direction, although we still assume ideal turbine yaw control. The BIC for each of the four case study locations versus the number of clusters for both the flattened and full five-dimensional data set is shown in Figure 5.3. Based on the convergence of the BIC indicating good fit without unnecessary computational expense, a final number of 35 clusters for the aligned cases and 50 clusters for the misaligned cases was selected. The exact clusters and cluster center coordinates are shown in Sections 5.3 through 5.6.

5.2.3 Simulation Procedure

Once clusters for each case study location data set were generated, the conditions described by each cluster center were simulated with the coupled, aero-hydrodynamic model. A JONSWAP spectrum with $\gamma = 3.3$, a representative value for mixed wind-sea and swell driven conditions [99], [100], and significant wave height and peak wave

frequency set to the cluster center values is used to simulate irregular ocean wave conditions.

The mean wind speed is set to the mean wind speed of the cluster center U_∞. Wind turbulence is modeled with a Kaimal spectrum, as outlined by IEC guidelines IEC 61400-1 [82]. The Kaimal spectrum power spectral density of the streamwise turbulence is defined in Equation 4.12. For the purpose of this study, we set the turbulence intensity $I_u = 0.06$ as a reasonable benchmark value [101, 102, 103]. In reality, turbulence intensity varies between close to zero and 0.15 on diurnal and monthly cycles. However, our primary aim is to model the effect of wind and wave induced platform motion on performance, so we only include a simple turbulence model. In addition, we keep turbulence intensity constant between the case study locations to better compare the effects of the varying steady-wind and wave conditions. In order to obtain a realistic time series of turbulent wind from the Kaimal spectrum, we first generate a wind speed spectrum in the frequency domain. For a time series of length T and time step Δt, we discretize our frequency domain with the frequency vector f_n expressed as follows:

$$f_n = n\Delta f \quad \text{for} \quad n = 1, 2, ..., \frac{N}{2}, \tag{5.6}$$

where $N = T/\Delta t$, and $\Delta f = 1/T$. We then define the spectral amplitude A_n at each frequency as follows:

$$A_n = \sqrt{2S_u(f_n)\Delta f}, \tag{5.7}$$

where S_u is the Kaimal turbulence power spectral density. We then assign a random phase ϕ_n between 0 and 2π to each frequency and generate the complex Fourier coefficients for our spectrum

$$\hat{u}_n = A_n e^{i\phi_n}. \tag{5.8}$$

Finally, the fluctuating component of the wind speed is converted into the time domain with an inverse fast Fourier transform (IFFT) function, and added to the mean wind speed $\overline{U}$ to generate the turbulent time series $U_\infty(t)$:

$$U_\infty(t) = \overline{U} + \mathrm{Re}\left[\mathrm{IFFT}(\hat{u})\right]. \tag{5.9}$$

This method of turbulence modeling does not account for variations in turbulence across the rotor. Instead, the streamwise turbulence model is meant to approximate the likely variation in quasi-steady inflow velocity at the hub over a representative 10-minute sample. The low-fidelity aerodynamic model presented in this work does

not include individual blade modeling or variations in velocity due to platform motion along the length of the blade. As such, it is not designed to model turbulence variation across the rotor. Despite this, it is clear that the freestream velocity will vary significantly within a 10-minute sample at a representative FOWT site. The variation in freestream velocity will have important implications for platform motion and may interact differently with varying sea states between turbine sites. As such, we include this simplified turbulence model to approximate the likely variation in quasi-steady inflow velocity at our case study locations.

For each cluster, a 10-minute time series of turbulent wind about the cluster's mean wind speed is generated and then repeated to generate the three-hour wind speed time series. Each cluster center condition was simulated for three hours after an additional 3600 s of initial simulation time to remove any startup transients. This duration is set out in the IEC guidelines [16], and was also used by Fontanella et al. [30].

5.2.4 Site Specific Performance Curves

Inter-site comparisons between the four case study locations are made via two metrics: site-specific performance curves and annual energy production (AEP). Site-specific performance curves were generated via the method outlined in IEC guideline 61400-12 [104]. Time domain simulations of one cluster center condition are split into ten-minute segments. The average power and thrust during these ten-minute segments are calculated and stored. The fluctuation of power and thrust is measured within each ten-minute segment as the value two standard deviations above and below the mean.

From this point a site-specific power and thrust curve can be constructed. The operational wind speed range is split into 0.5 m/s wide bins. Average and fluctuating components of power and thrust from each individual ten-minute segment are sorted into their respective wind speed bin based on average free stream velocity. The mean values of the average and fluctuating components of power and thrust in each wind speed bin are then taken. Wind speed bins with no data are filled via linear interpolation from adjacent bins. Values can then be plotted versus wind speed to obtain turbine performance curves.

To compute site AEP, the best fit Weibull distribution of wind speed over the year of ERA 5 wind speed data is found. This distribution is then multiplied by the site-specific power curve.

5.3 Location 1: ScotWind Ossian Lease Site

The first case study location is located approximately 84 km off the east coast of Scotland in the North Sea. The exact coordinates used to define the site location for ERA 5 data extraction are 56.687 N, 0.393 W. The average water depth of the site is 72 m, and it has been leased for floating turbine development.

Clusters for the ScotWind site in wind and wave aligned conditions are shown in Figure 5.4, while clusters for the site including all conditions are shown in Figure 5.5. In the full five-dimensional data set, we see a tendency towards wind and wave alignment, with two thirds of cluster centers being wave and wind aligned within 25 degrees. Less than 30 % of cluster centers are misaligned by more than 45 degrees. The direction of aligned wind and waves varies significantly between zero and 360 degrees. In both 3D and 5D data sets, cluster centers vary from 3.5 to 9.5 s mean wave period, 0.5 to 5 m significant wave height, and 4 to 20 m/s wind speed. The ideal, aligned data set places cluster centers closer to outliers in significant wave height and mean wave period. As additional parameter dimensions are added, the cluster centers tend to group towards average values, and move farther from outlier points. Despite this, the five-dimensional GMM clusters still range between 3.5 and 20 m/s, covering the first cut-in wind speed bucket to significantly above the turbine rated wind speed.

In order to characterize the performance of the reference turbine at the ScotWind Ossian site under ideal, aligned conditions, power and thrust performance curves are shown in Figure 5.6. The floating turbine curves end at the wind speed of the cluster with the highest wind speed center within the operational range. For operational wind speeds beyond this point, we do not have simulated data to compare between the FOWT and static curves. In the low wind speed region (below 10 m/s), we see that the model predicts that the FOWT is able to outperform its static counterpart, capturing 45 % more power at 5 m/s and 8 % more power at 10 m/s. In part, the large percentage difference at low wind speeds is due to the static captured power approaching zero. However, this increase in power performance is still significant. A 10 to 20 % benefit in power capture between 7.5 and 9 m/s is noteworthy, as the best-fit Weibull wind speed distribution from the one year of data for this site peaks for around 9 m/s wind speeds, suggesting a significant increase in power capture at the most common wind speeds. The model predicts that the floating turbine also generates a non-zero power as wind speed approaches the cut-in speed. Unlike the static turbine, the FOWT is able to convert wave-induced motion at wind speeds at

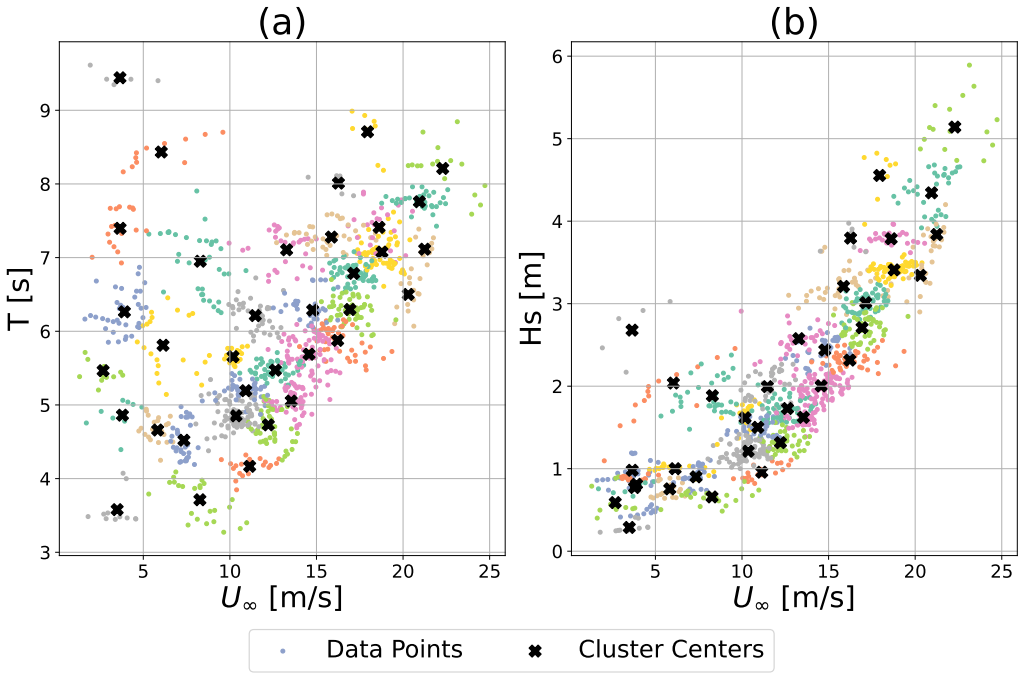

Figure 5.4: GMM cluster centers for ScotWind Ossian Lease Site in wind and wave aligned conditions.

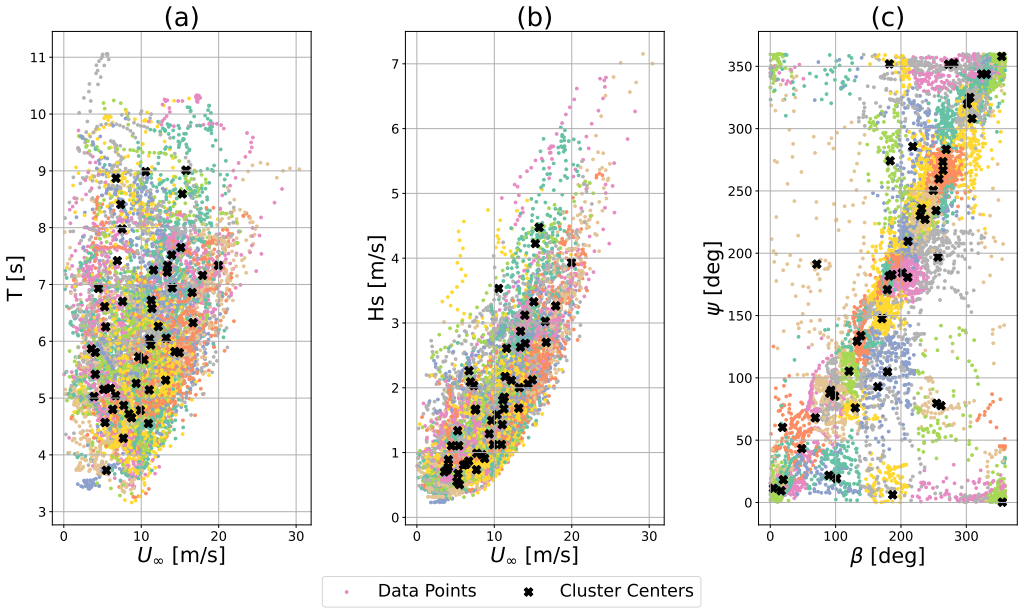

Figure 5.5: GMM cluster centers for ScotWind Ossian Lease Site in all conditions.

or below cut-in into power capture. This greater than static power capture in the below rated region is coupled with greater than static rotor thrust, peaking at 130 % of the static thrust around 5 m/s wind speed.

Near the rated wind speed, the FOWT decreases in mean power capture and rotor thrust relative to the static turbine. The normalized decrease in power capture in this region is smaller than the increase in power in the low wind speed region, due to the larger magnitude of the static power and thrust. The power capture and rotor thrust return to close to the static turbine values as wind speed increases above rated. The trends in average power capture and rotor thrust in all three wind speed regimes mirror those identified in Chapter 3 obtained with prescribed harmonic motion at the representative wave frequency.

As discussed in Chapter 4 Section 4.3.3, there is significant fluctuation of rotor thrust due to wind speed turbulence. The 10^{th} to 90^{th} percentile range of power and thrust due to turbulence for the static turbine generally increases with increasing wind speed. There are also large fluctuations of power, comparable to those at the highest wind speeds, near the rated wind speed. We see additional fluctuation beyond that of the static turbine for the FOWT. This additional fluctuation is due to platform motion, which further varies the freestream velocity variations experienced by the turbine rotor.

To examine the fluctuations of power and rotor thrust, box plots of the power and thrust obtained from each cluster center simulation for the ideal, wind-wave aligned case are shown in Figure 5.7. Significant fluctuations of power and thrust can be seen across all wind speeds. Fluctuation of generator power reaches a maximum around 9 and 23 m/s with a range over 33 % of the turbine rated power at both wind speeds. The range of rotor thrust generally increases with wind speed, reaching 57 % of the turbine rated thrust at 23 m/s and 59 % at 16 m/s. These fluctuations are due to combinations of wind speed turbulence and streamwise hub velocity caused by irregular wave loading on the platform which can cause extreme low or high wind speeds at the rotor. Additionally, these conditions can occur quickly enough that the turbine controller is not able to optimize the blade pitch or rotor speed to achieve the ideal turbine operating state. As such, large spikes and variations in power and thrust can occur. These large fluctuations of power and thrust will have significant effects on turbine component fatigue.

The power and thrust performance of the turbine under the full set of environmental conditions, including misaligned wind and waves, is shown in Figure 5.8. The inclusion of misaligned waves has a small, but significant effect on power capture at

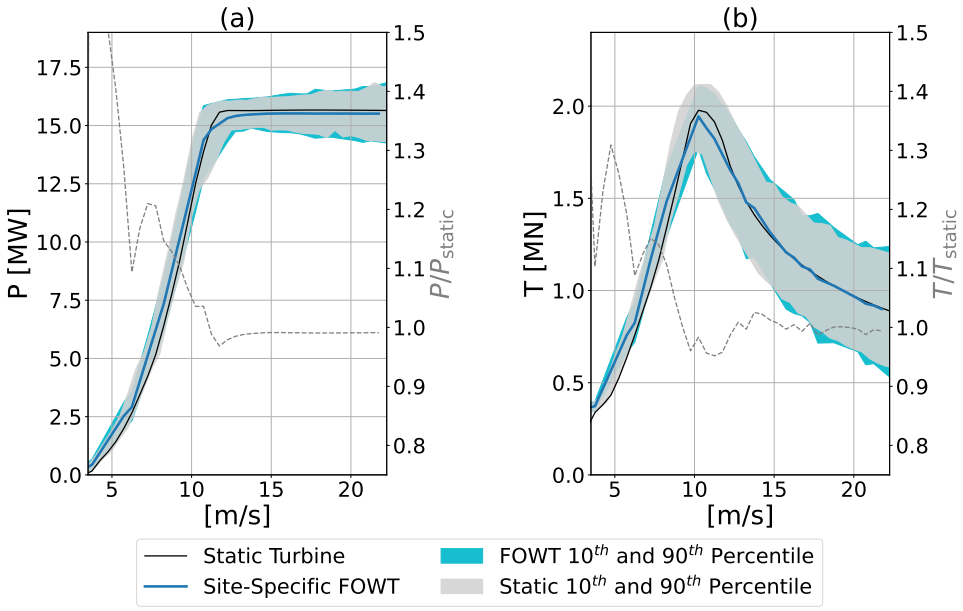

Figure 5.6: Absolute and normalized power (a) and thrust (b) curves for the 15 MW turbine at the ScotWind Ossian case study site in ideal wind-wave aligned conditions. Solid and dashed lines represent averages, while the shaded region shows the 10^{th} and 90^{th} percentile of power and thrust for the static and floating turbines.

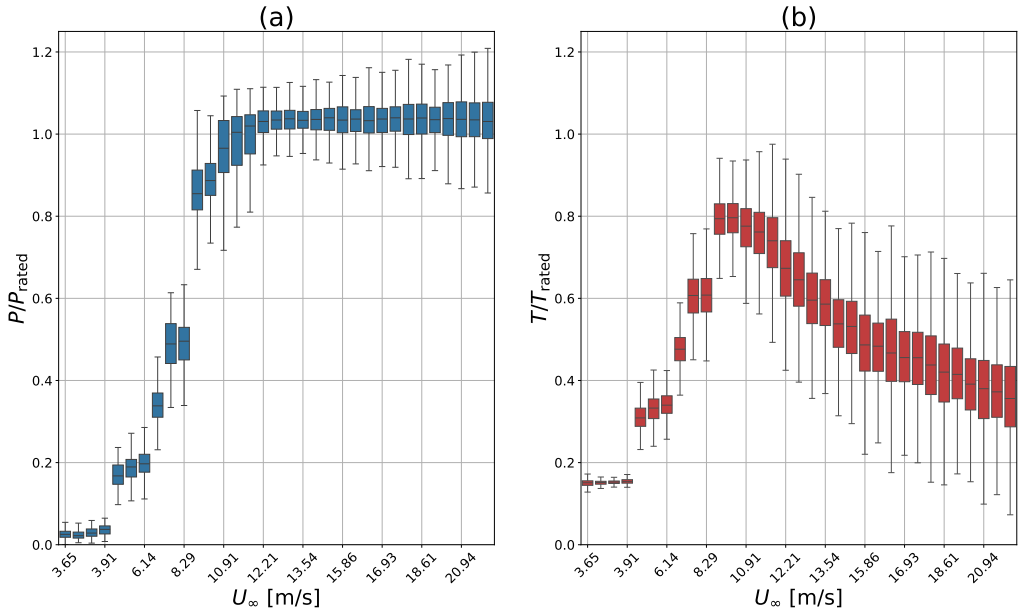

Figure 5.7: Box plot at each cluster center of the minimum, 25^{th} percentile, mean, 75^{th} percentile, and maximum of power (a) and thrust (b) for the ScotWind Ossian case study site in ideal wind-wave aligned conditions.

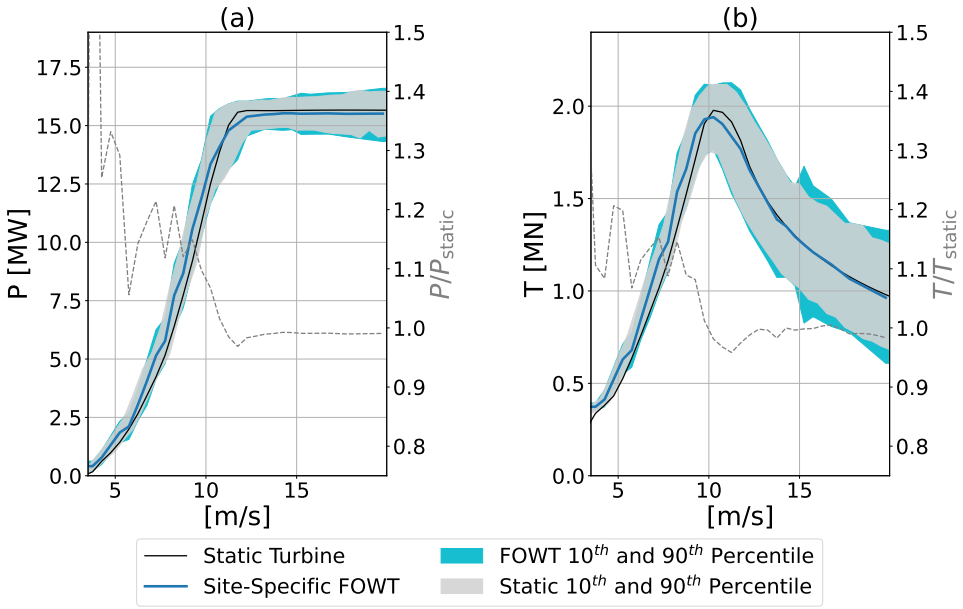

Figure 5.8: Absolute and normalized power (a) and thrust (b) curves for the 15 MW turbine at the ScotWind Ossian case study site. Solid and dashed lines represent averages, while the shaded region shows the 10^{th} and 90^{th} percentile of power and thrust for the static and floating turbines.

low wind speeds relative to the static baseline. Misaligned conditions at this site are relatively infrequent, so the difference to the ideal, aligned case is small. Again, we see a 10 to 20 % increase in average power capture between 7.5 and 9 m/s, and a 1 to 3 % decrease in average power capture around the rated wind speed. The rotor thrust also behaves similarly to the fully aligned case, with a 10 to 20 % increase in average thrust relative to static at those same wind speeds. Relative to the static turbine, the FOWT experiences higher fluctuations of both power and rotor thrust. These fluctuations are the largest for high wind speeds. At 15 m/s wind speed, the inclusion of floating platform motion increases the 10^{th} to 90^{th} percentile range of rotor thrust by over 40 %. The additional fluctuation caused by platform motion is larger than for the ideal, aligned subset of the data.

The fluctuation of power and thrust as characterized by box plots of each cluster center for all environmental conditions, including misaligned waves, are shown in Figure 5.9. In cases which include misaligned wind and waves, we see increased fluctuation in both power and thrust relative to the ideal, aligned case. The maximum recorded thrust for all wind speeds is increased by 0.3 MN, or 12 % of turbine rated thrust, versus the ideal case. The maximum range of thrust increases up to 80 % of the turbine rated thrust at 16 m/s and 65 % at 12 m/s. The range of power is

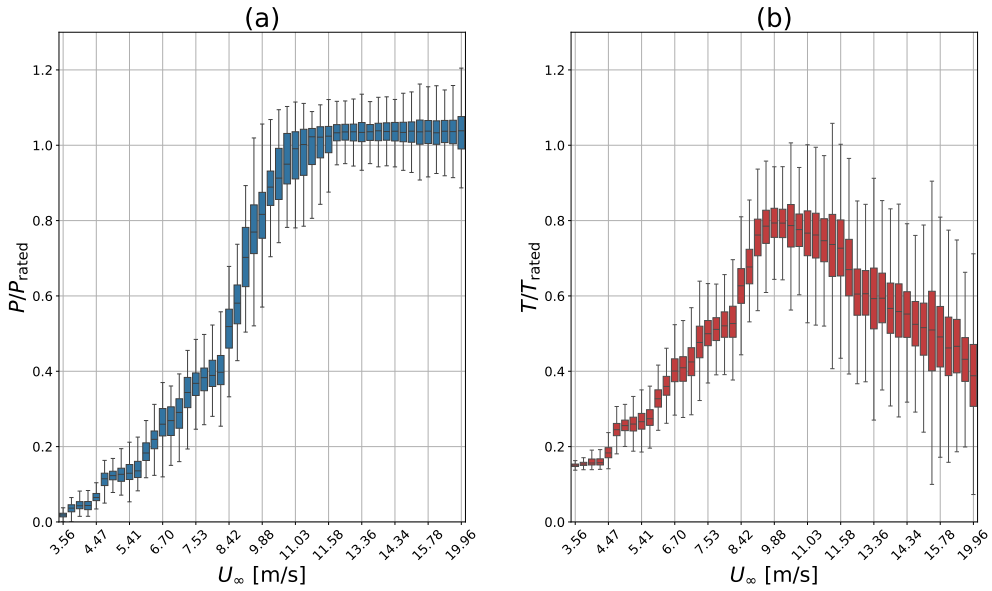

Figure 5.9: Box plot at each cluster center of the minimum, 25^{th} percentile, mean, 75^{th} percentile, and maximum of power (a) and thrust (b) for the ScotWind Ossian case study site.

similarly increased, reaching 48 % of the turbine rated power at 10 m/s. The location of the maximum range of power is shifted for the misaligned case to the near-rated wind speed region, although the magnitude of power fluctuation in the near-rated and high wind speed regions are similar. These larger turbine load ranges suggest that misaligned wind and waves increase turbine load fluctuation. From Figure 5.8 we saw that the floating turbine will experience somewhat larger load fluctuations relative to a static turbine. Saenz-Aguirre et al. [88] show that larger load fluctuation due to wave-induced platform motion will increase fatigue damage to turbine components. This fatigue damage will result in a reduced life span and increased maintenance cost of floating versus fixed turbines. We do not go further in depth towards calculating fatigue damage based on this load fluctuation. Instead, we use fluctuation as a proxy for fatigue damage, assuming that greater load fluctuation will induce greater fatigue damage over the turbine life span.

The maximal thrust force measured during simulation occurs at a wind speed above the turbine rated wind speed. In general, wind turbine design processes assume that the highest thrust loading will occur at the rated wind speed. The ROSCO controller thrust-shaving module is tuned to minimize thrust around the turbine rated wind speed [53]. The discrepancy between the true wind speed of the maximum thrust load and the assumed wind speed of maximal thrust loading could cause over-

conservative controller tuning at the rated wind speed, and unsafe controller tuning above the rated wind speed. For example, most PI wind turbine controllers schedule proportional gains across wind speed. As the thrust at above rated wind speeds is higher than expected, the scheduled proportional gain may not be sufficient to quickly pitch the blades to avoid excessive thrust loading.

Finally, in order to relate specific variations in environmental conditions to turbine performance, we show the normalized difference of the FOWT power and thrust relative to static mapped onto the cluster centers for the full data set in Figure 5.10. The two standard deviation fluctuation of the FOWT power and thrust mapped onto cluster centers is shown in Figure 5.11. The difference of average power and thrust to static is normalized by the rated power and thrust at each wind speed. The fluctuation of power and thrust is normalized by the turbine power and thrust at the rated wind speed. In both the average and the fluctuation of FOWT power and thrust, we see a strong dependence on wind speed. In fact, wind speed dominates mean wave period in determining both metrics. In Chapter 4, the coupled model predicted that regular wave amplitude would have a large effect on the average and fluctuating components of turbine power and thrust. As such, we expect significant wave height will also have a significant effect on performance. However, the effect of wave height in this data set is complicated by the strong correlation between wind speed and significant wave height. As such, it is difficult to isolate the effect of each parameter on turbine performance from this data. A similar issue occurs for the effects of wind and wave direction. Centers with greater misalignment have a larger performance discrepancy to static. However, misaligned conditions in this data set are much more likely to occur in low wind speeds. As such, we see a conflation of the two variables. In general, the wind speed regime plays a greater role in determining a FOWT's performance relative to static than mean wave period, at least within the limited range of mean wave periods considered in this case study.

We do see correlations with wind speed. Low wind speeds induce the greatest difference between the static and floating turbine models for both average power and thrust. This discrepancy decreases as wind speed increases. The fluctuation of turbine power is the greatest for near-rated wind speeds. The largest fluctuation of turbine thrust occurs for larger wind speeds. This suggests that low wind speeds will play an important role in determining turbine average power capture and component loading due to average thrust and the average components of rotor torque. Near-rated wind speeds will cause the largest fluctuations of power. High wind speeds will be

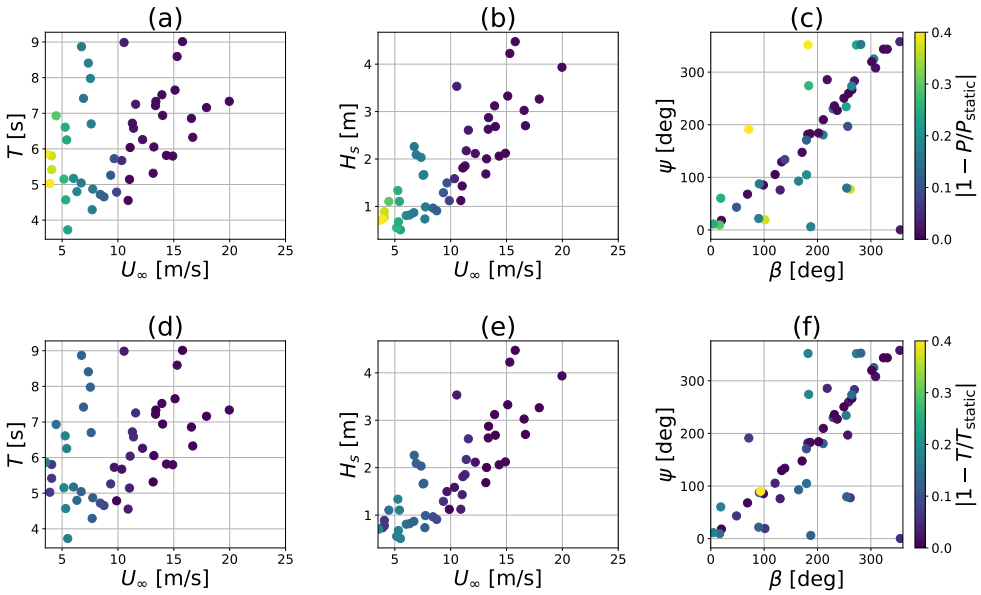

Figure 5.10: Normalized difference between FOWT power (a - c) and thrust (d - f) versus a static turbine mapped onto GMM cluster centers for the ScotWind Ossian case study site.

important for the fluctuating component of rotor thrust and blade and tower fatigue damage due to fluctuating rotor thrust.

5.4 Location 2: Celtic Sea PDA 1 Lease Site

The second case study location is located in the Celtic Sea between England and Wales. The exact coordinates used for ERA 5 data extraction are 51.302 N, -5.244 W. The site's average water depth is 71 m and it has been leased by the UK Crown Estate for FOWT development.

Clusters for the Celtic Sea site in ideal, wind and wave aligned conditions are shown in Figure 5.12, and for the full five-dimensional data set including misalignment in Figure 5.13. Similar to the ScotWind site, there is a tendency towards wind and wave alignment with only 14 of the 50 cluster centers in the full data set having a wind wave misalignment of greater than 45 degrees. However, the wind and waves are more likely to come from headings between 200 and 300 degrees. This heading corresponds to westerly wind and waves coming from more open waters to the west of the site. Cluster centers vary between 4 and 10 s mean wave period. The ideal, aligned data set contains cluster centers with significant wave height up to 7 m and wind speeds up to 32 m/s. The full data set does not contain cluster centers at these

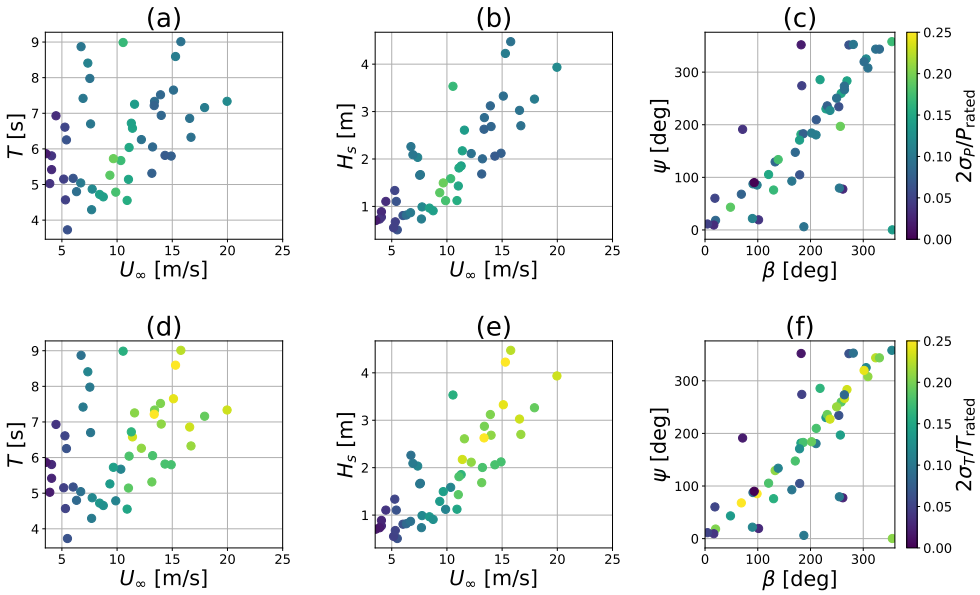

Figure 5.11: Two standard deviations of power (a - c) and thrust (d - f) normalized by rated turbine values mapped onto GMM cluster centers for the ScotWind Ossian case study site.

extremes with wave heights between 0.5 and 4.5 m and wind speeds between 4 and 19 m/s. However, the data set does include a full range of operational wind speeds from cut-in to above rated. As significant wave height is strongly correlated with wind speed, this indicates that operational wave heights are also represented.

The power and thrust performance curves for the IEA 15 MW RWT at the Celtic Sea case study site in ideal, aligned wind-wave conditions are shown in Figure 5.14. At low wind speeds, the FOWT outperforms the static turbine. The FOWT power capture is increased by 31 % at 6 m/s and between 7 and 18 % between 7.5 and 9 m/s. The increased power capture around 8 m/s is slightly less than that for the ScotWind Ossian site, due to lower significant wave heights and lower mean wave periods at this wind speed. As seen in the regular wave cases in Chapter 4, wave periods below 6 s have a smaller effect on power capture than those in the 8 to 12 s range. Additionally, power capture is found to scale with wave amplitude, so smaller significant wave heights will induce less power capture at below rated wind speeds. Rotor thrust relative to the static turbine is increased by 23 to 5 % between 5 and 9 m/s wind speeds, with the difference decreasing as wind speed increases. Near rated, the power capture and rotor thrust dip below the static turbine values. The FOWT power at rated is 98 % of static and rotor thrust is 93 % of static. Similar to the

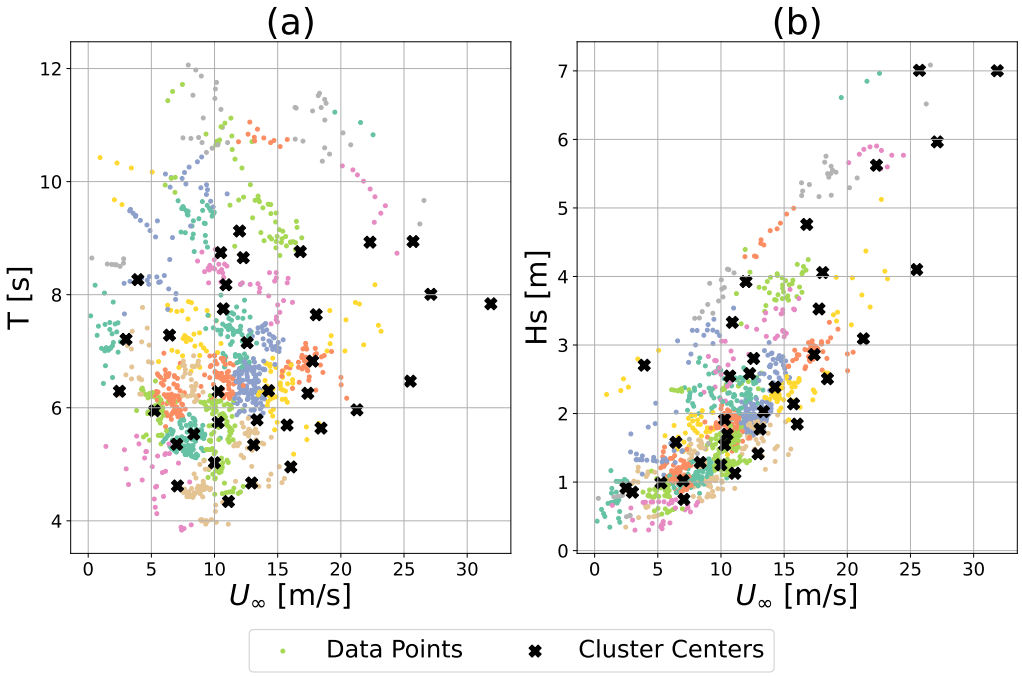

Figure 5.12: GMM cluster centers for Celtic Sea PDA 1 Lease Site in wind and wave aligned conditions.

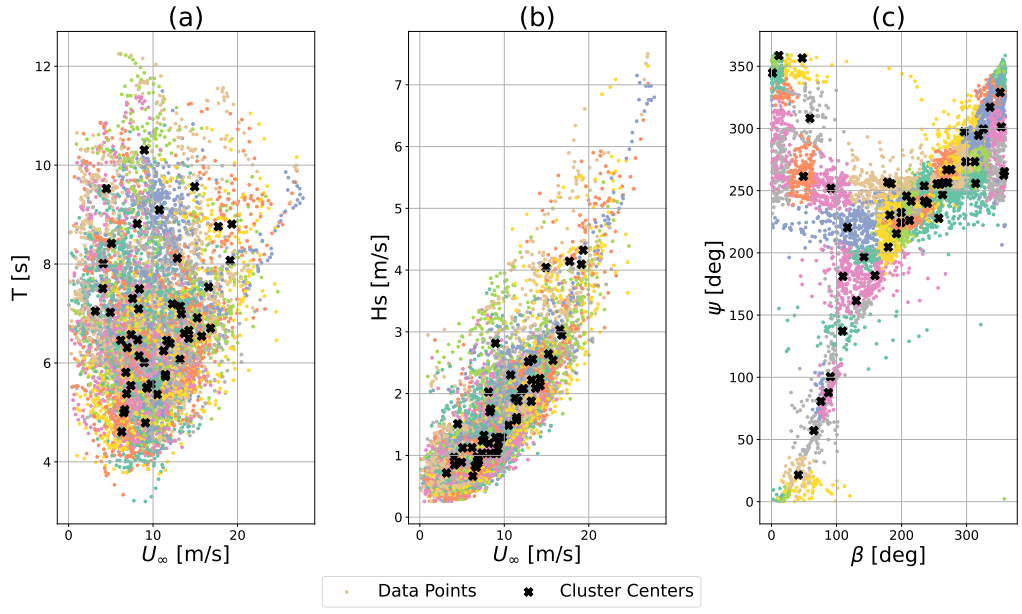

Figure 5.13: GMM cluster centers for Celtic Sea PDA 1 Lease Site in all conditions

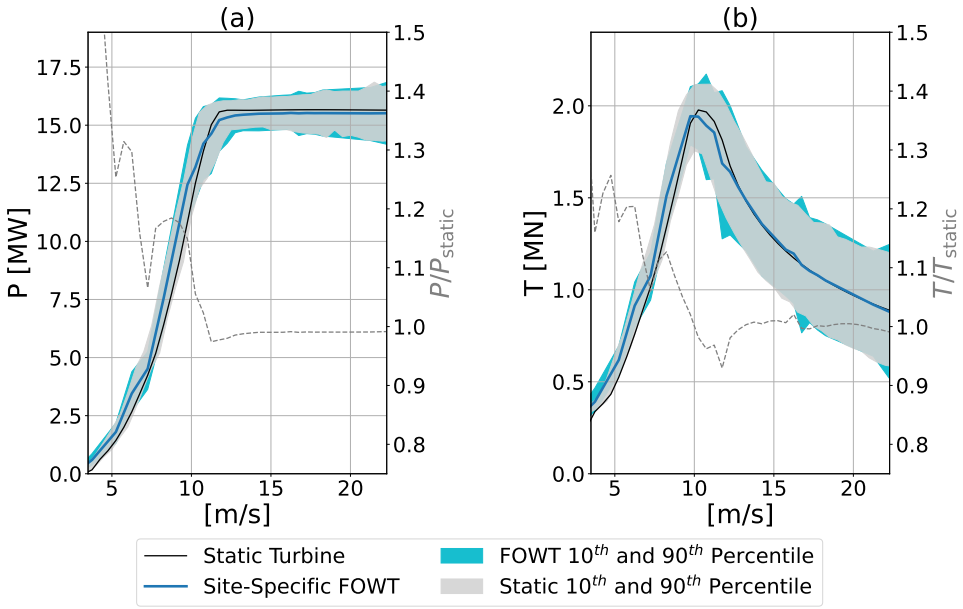

Figure 5.14: Absolute and normalized power (a) and thrust (b) curves for the 15 MW turbine at the Celtic Sea case study site in ideal wind-wave aligned conditions. Solid and dashed lines represent averages, while the shaded region shows the 10^{th} and 90^{th} percentile of power and thrust for the static and floating turbines.

ScotWind Ossian site, we see a small increase in power and rotor thrust fluctuations for the FOWT versus the static turbine baseline.

Fluctuations of generator power and rotor thrust are shown in box plots for each cluster center for the ideal, aligned data set in Figure 5.15. Fluctuations of 30 to 40 % of the rated generator power occur for the cluster centers between 10 and 11 m/s. A fluctuation equal to 36 % of the rated power occurs for the highest wind speed cluster center at 22 m/s. Large thrust fluctuations of up to 69 % of rated occur for cluster centers between 11 and 13 m/s, and above 21 m/s. Similar to the ScotWind site, the largest fluctuations of power and thrust occur for centers in the near-rated or high wind speed regime. Fluctuations below 10 m/s are smaller, between 5 and 29 % of rated for power and 12 and 20 % of rated for thrust. Again, these fluctuations will have significant effects on component fatigue.

Power and thrust performance curves for the Celtic Sea site and the full data set including misalignment are shown in Figure 5.16. Power capture in the full data set is slightly decreased relative to the aligned data set. However, the effect is fairly small. Power capture is 125 % of static around 5 m/s and 110 % of static at 10 m/s wind speed. Rotor thrust is also similar between the aligned and full data set at wind speeds below rated. Power capture and rotor thrust for the FOWT are lower than

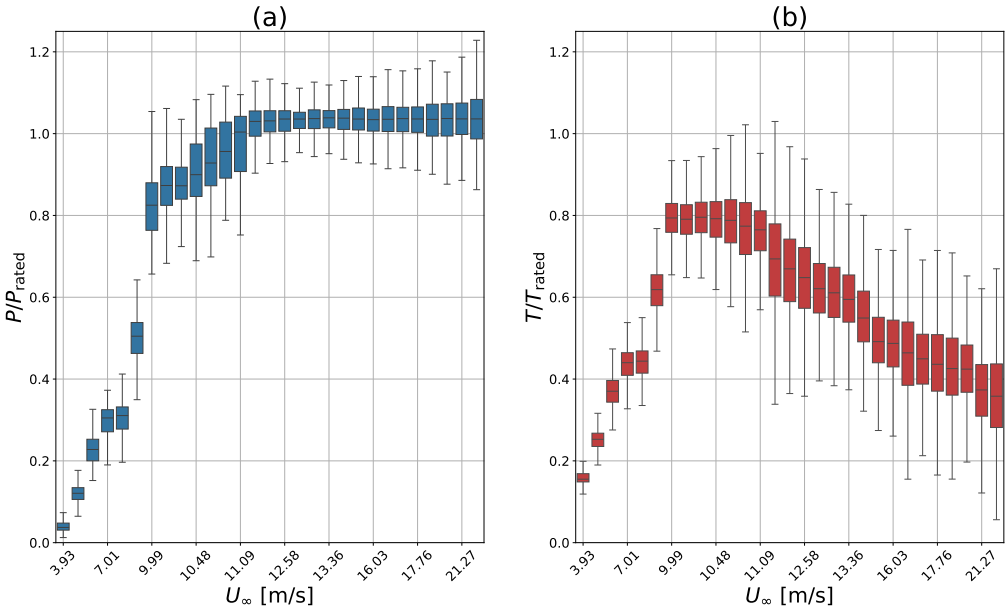

Figure 5.15: Box plot at each cluster center of the minimum, 25^{th} percentile, mean, 75^{th} percentile, and maximum of power (a) and thrust (b) for the Celtic Sea case study site in ideal wind-wave aligned conditions.

for static near the rated wind speed, and return to close to static values for large wind speeds. The 10^{th} to 90^{th} percentile fluctuation of rotor thrust for the FOWT, including misaligned cases, is large for high wind speeds.

Fluctuation of power and thrust for the full data set including misaligned wind and waves is shown in Figure 5.17. The fluctuation of power is greatest for centers with wind speed between 9 and 10 m/s. In this wind speed range, power fluctuation reaches up to 50 % of the turbine rated power. At high wind speeds up to 18 m/s, power fluctuates by up to 32 % of rated. This is larger than that for the aligned data set at those same wind speeds, again illustrating wind-wave misalignment's tendency to increase power fluctuation. The same is true for the thrust fluctuation, which has a maximum range of 78 % of the turbine rated thrust at the center with 14.5 m/s wind speed. Thrust fluctuation also increases as wind speed increases. The magnitude of power and thrust range for the Celtic Sea case study site is in line with that for the ScotWind Ossian case study site. Again, we see that floating turbines will experience significant load fluctuation, especially at near-rated and high wind speeds.

The normalized difference of the FOWT power and thrust relative to static and two standard deviation fluctuation of power and thrust mapped onto the cluster centers for the Celtic Sea case study site are shown in Figures 5.18 and 5.19. Similar to the ScotWind Ossian site, wind speed can be used to determine trends in the difference

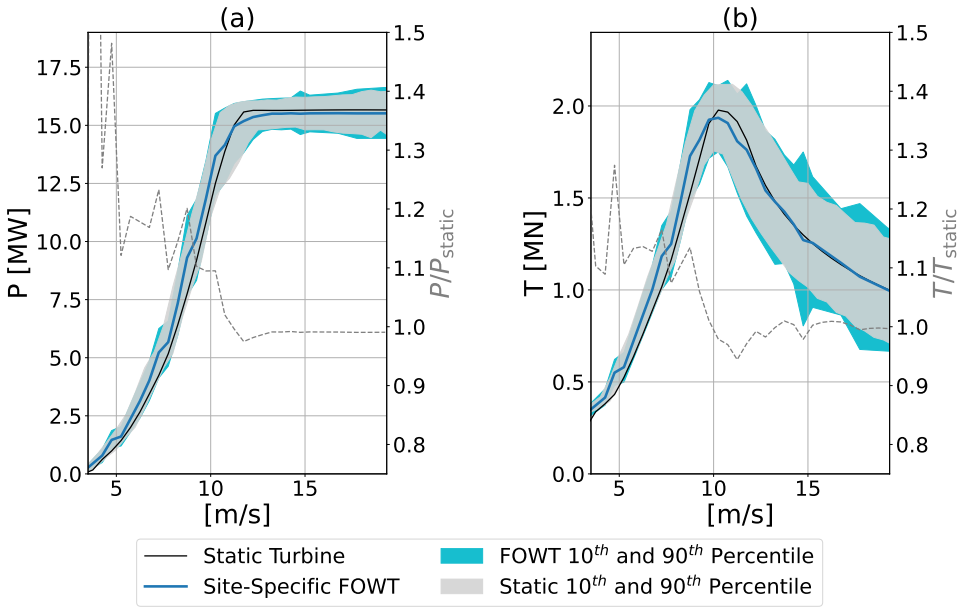

Figure 5.16: Absolute and normalized power (a) and thrust (b) curves for the 15 MW turbine at the Celtic Sea case study site. Solid and dashed lines represent averages, while the shaded region shows the 10^{th} and 90^{th} percentile of power and thrust for the static and floating turbines.

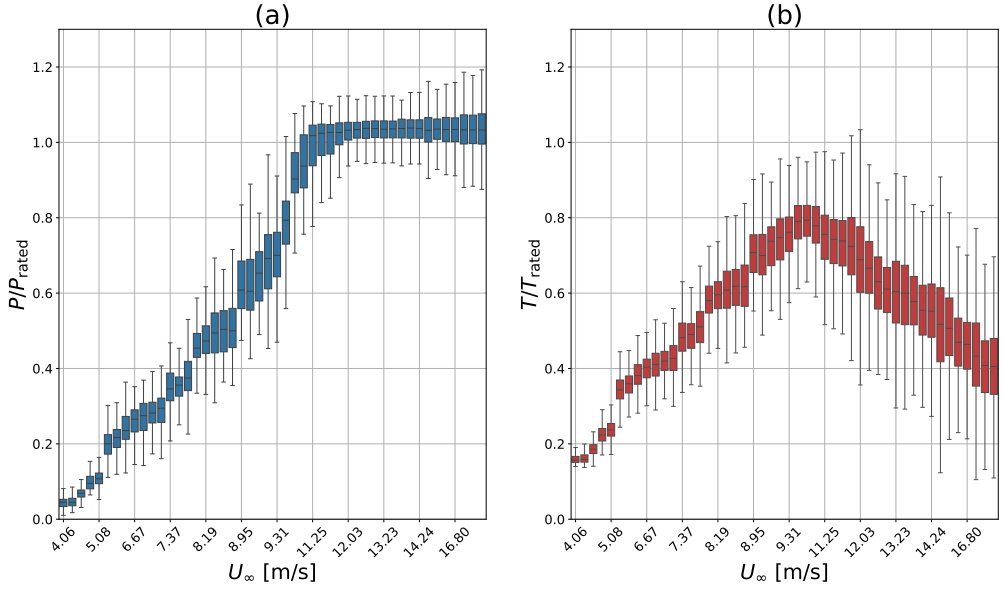

Figure 5.17: Box plot at each cluster center of the minimum, 25^{th} percentile, mean, 75^{th} percentile, and maximum of power (a) and thrust (b) for the Celtic Sea case study site.

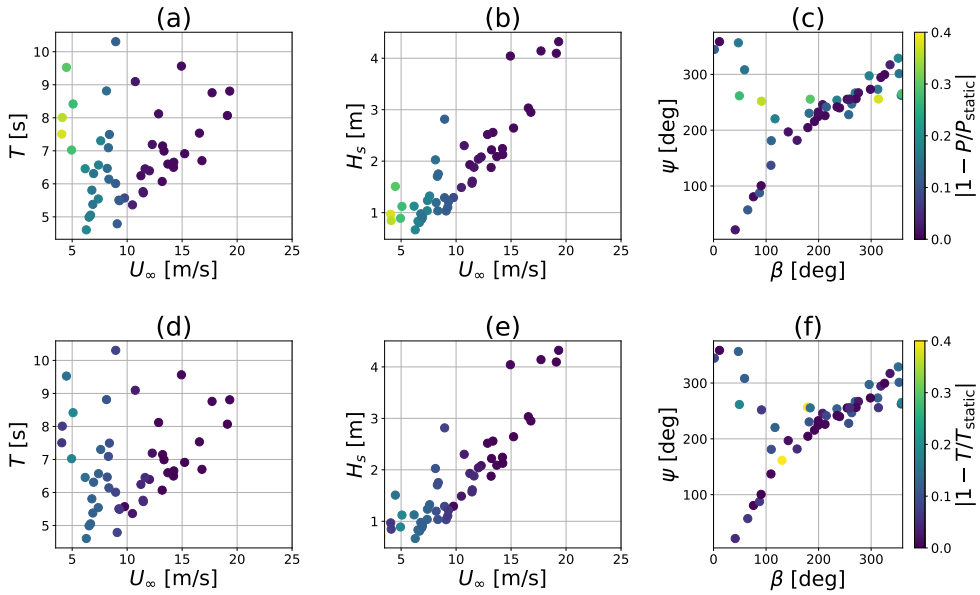

Figure 5.18: Normalized difference between FOWT power (a - c) and thrust (d - f) versus a static turbine mapped onto GMM cluster centers for the Celtic Sea case study site.

between the floating and fixed turbine performance. At all wind speeds, the difference between the floating and static turbine is largely independent of variations in mean wave period. Wind speed also dominates the normalized fluctuation of power and thrust. There is some variation in centers with similar wind speeds between 8 and 10 m/s due to differences in wind and wave alignment relative to each other and to the platform. However, this difference is less significant than differences across wind speed regimes. Again, low wind speeds see the largest difference in average power capture and average rotor thrust, while near-rated wind speeds see the largest fluctuation of power, and high wind speeds see the largest variation of rotor thrust.

5.5 Location 3: New York OCS-A 0537 Lease Site

The third case study location considered is the OCS-A 0537 lease site located 38 miles off the coast of lower New York, USA, near Block Canyon. The exact coordinates used for ERA 5 data extraction are 40.103 N, -71.801 W. The average water depth at this site is 75 m. The site has been leased by the US Bureau of Ocean Energy Management to Bluepoint Wind LLC for fixed offshore wind development.

Clusters for the New York site in wind and wave aligned conditions are shown in Figure 5.20 and for the full five-dimensional data set in Figure 5.21. The site

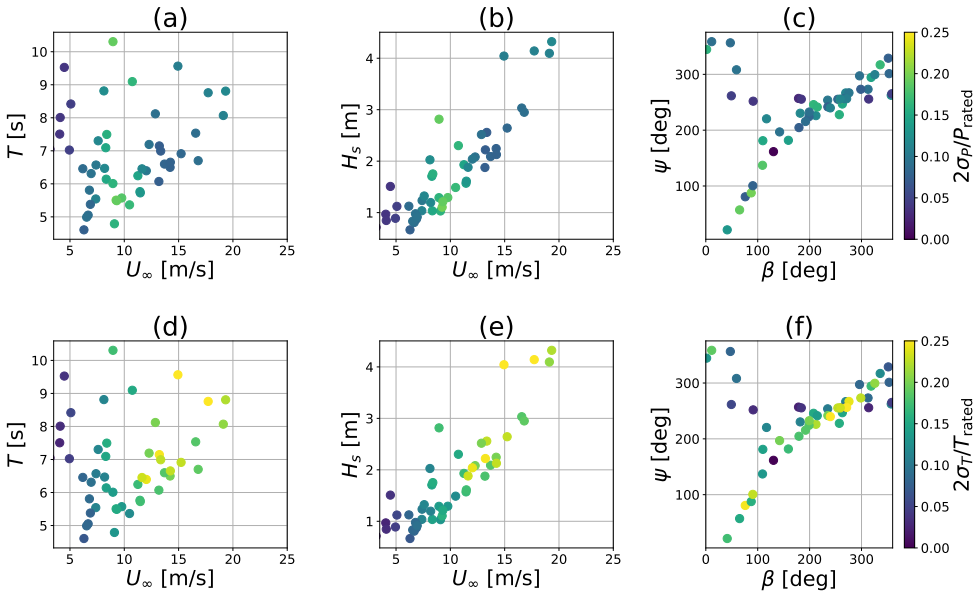

Figure 5.19: Two standard deviations of power (a - c) and thrust (d - f) normalized by rated turbine values mapped onto GMM cluster centers for the Celtic Sea case study site.

exhibits slightly less strong wind-wave alignment than the UK sites, with 17 of 50 cluster centers more than 45 degrees misaligned. The mean wave periods of the New York site are larger than the two UK sites. For the five-dimensional data set, cluster centers range from 5 to 11.5 s. Significant wave heights are between 0.5 and 4.5 m, except for one outlier at 7.5 m. The ideal, aligned data set exhibits a more even spread of significant wave heights between 0.5 and 6 m and a smaller range of mean wave periods between 4 and 9.5 s.

Power and thrust performance curves for the New York case study location under ideal, aligned conditions are shown in Figure 5.22. The overall trends for the wind and wave aligned power and thrust curves are highly similar to those for the previous two case study locations. The increase in power capture relative to static in the below rated region ranges from 25 to 10 % at 5 and 10 m/s wind speed respectively. The decrease in power capture is 3 %, and thrust is 6 % below static at the rated wind speed. The 10^{th} to 90^{th} percentile variation in thrust is small below the rated wind speed and increases significantly as wind speed rises.

Fluctuation in power and thrust for the wind and wave aligned data set is shown in Figure 5.23. The largest variations in generator power occur for cluster centers just below the rated wind speed and for the maximum wind speed. The range of power is 44 % of rated power at 10 m/s and 33 % at 23 m/s. The maximum thrust

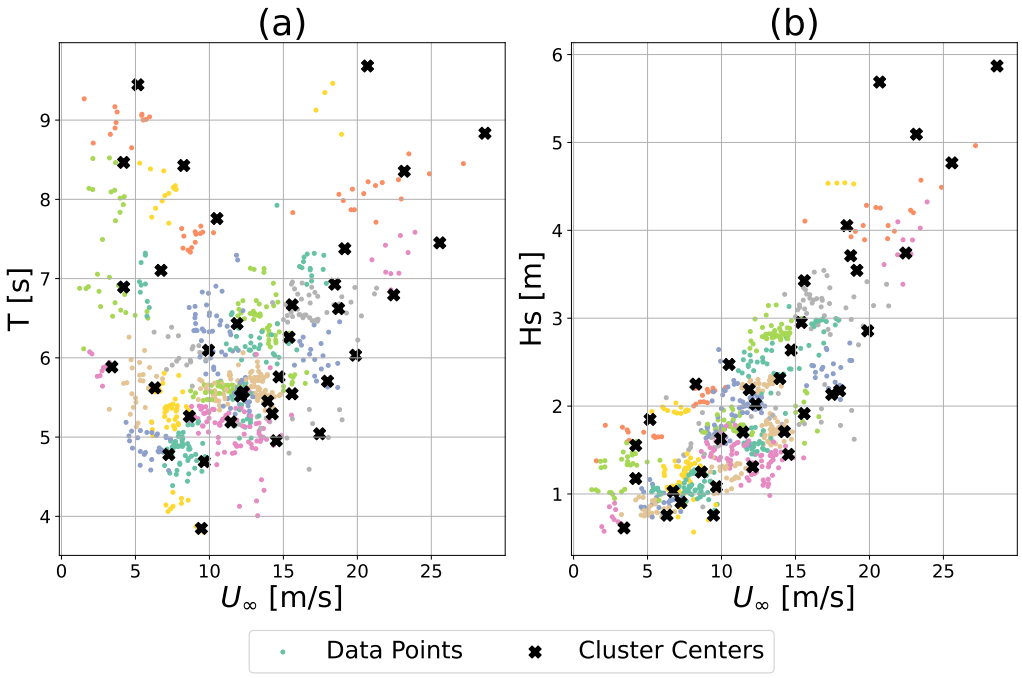

Figure 5.20: GMM cluster centers for New York OCS-A 0537 Lease Site in wind and wave aligned conditions.

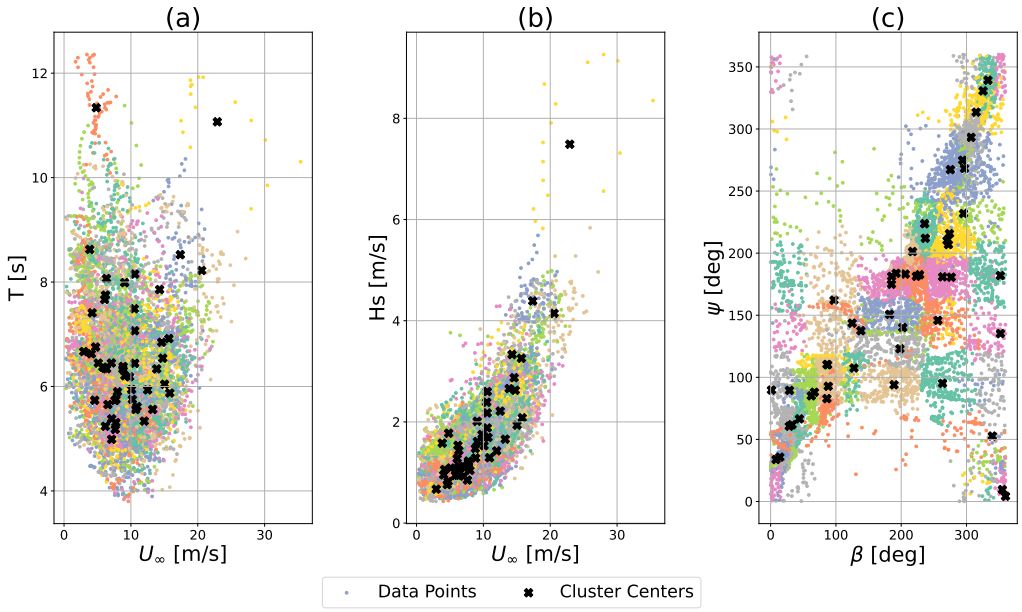

Figure 5.21: GMM cluster centers for New York OCS-A 0537 Lease Site in all conditions.

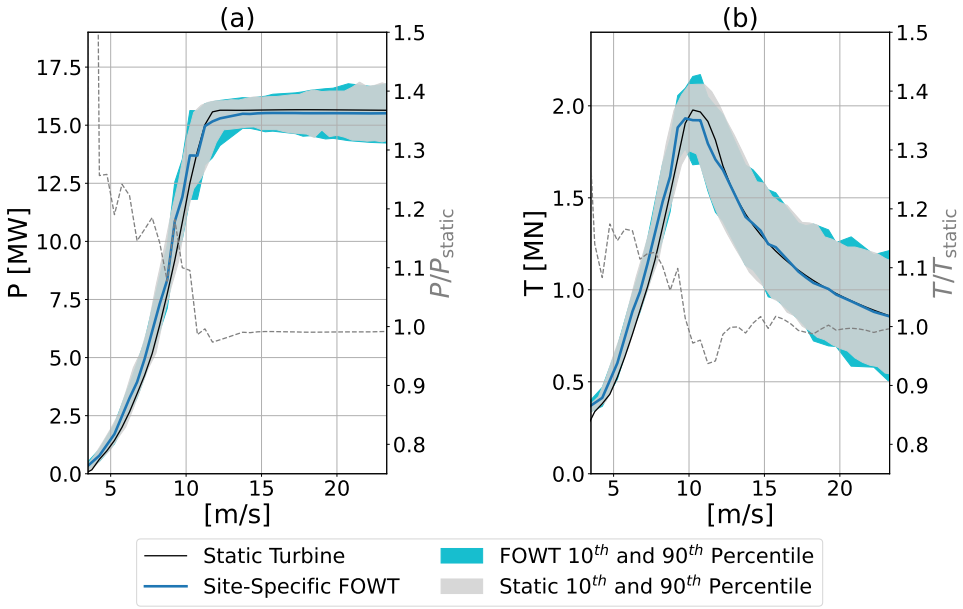

Figure 5.22: Absolute and normalized power (a) and thrust (b) curves for the 15 MW turbine at the New York case study site in ideal wind-wave aligned conditions. Solid and dashed lines represent averages, while the shaded region shows the 10^{th} and 90^{th} percentile of power and thrust for the static and floating turbines.

fluctuations occur for the cluster centers with the highest wind speed. The thrust range at 22.5 m/s wind speed is 60 % of the rated thrust. The thrust range near the rated wind speed is slightly less, 50 % of rated at 11.5 m/s. In general, the power and thrust fluctuation is small for low wind speeds. The total ranges for power and thrust at 4.2 m/s are 7 and 9 % of rated respectively.

Performance curves and the fluctuation of power and thrust for the full data set including misalignment are shown in Figures 5.24 and 5.25. Power capture in the below rated region varies between 20 and 9 % greater than static at 5 and 10 m/s wind speed respectively. This behavior is the same as seen in ideal, aligned conditions, albeit slightly reduced. In this below rated wind speed range, the thrust is increased by between 17 and 1 %, mirroring the results for aligned conditions. As seen for all case study locations, power is decreased slightly at the rated wind speed and returns to a near static value as wind speed increases above rated. The two standard deviation fluctuation of both power and thrust increases with wind speed in the above rated region.

As identified for each of the previous case study locations, inclusion of wind and wave misalignment increases the range of power and thrust fluctuations. Also mirroring the other locations, we see that power fluctuation is largest for cluster centers

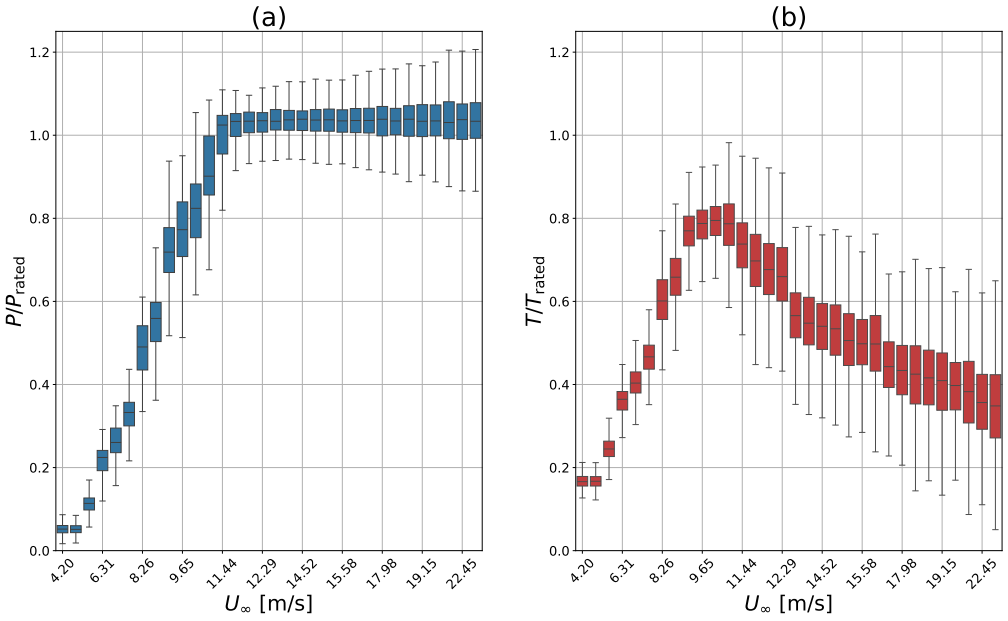

Figure 5.23: Box plot at each cluster center of the minimum, 25^{th} percentile, mean, 75^{th} percentile, and maximum of power (a) and thrust (b) for the New York case study site in ideal wind-wave aligned conditions.

with near rated or maximal wind speed. The range of power is 40 % of the rated power at 10.57 m/s wind speed and 33 % for 17.5 m/s wind speed. Thrust fluctuation is the largest in the high wind speed regime with a range of 70 % of rated at 17.4 m/s wind speed. Based on the trends seen in the 10^{th} to 90^{th} percentile fluctuation and maximal fluctuation, we expect the range of power and thrust to continue to increase up to the cut-out wind speed of 25 m/s. The fluctuations near cut-out speed are predicted to be very large, greater than 6 MW for power and 2 MN for thrust, or 40 and 82 % of the turbine's rated values. These extreme high wind speed fluctuations will have significant implications for component fatigue damage.

The normalized difference of the FOWT power and thrust relative to static and two standard deviation fluctuation of power and thrust mapped onto the cluster centers for the New York case study site are shown in Figures 5.26 and 5.27. The trends discussed for the prior two case study locations hold true for the New York site.

5.6 Location 4: North Carolina Coast

The fourth and final case study location is off the coast of North Carolina, USA. This location has coordinates 34.6 N, -75.9 W. The average water depth at this location is

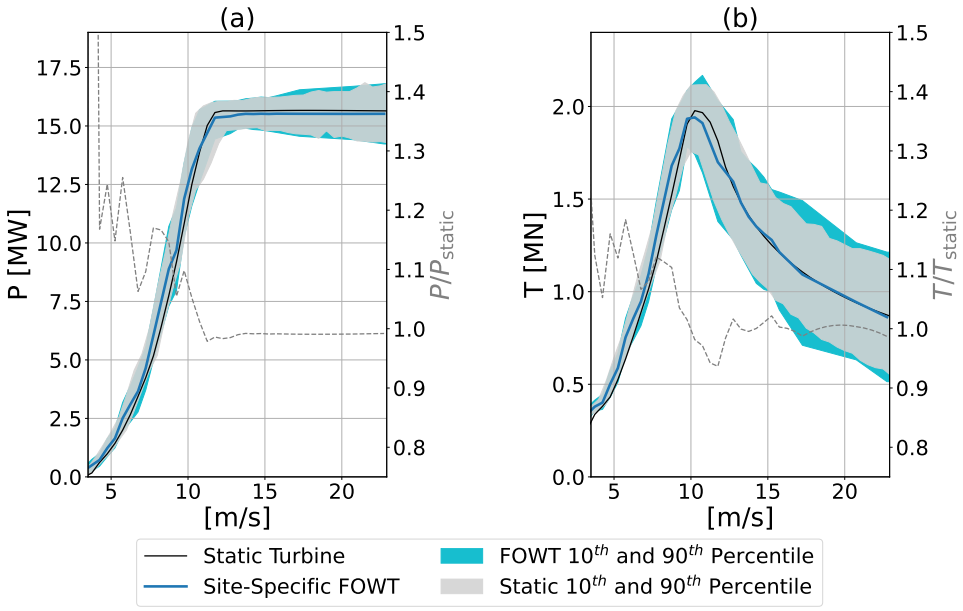

Figure 5.24: Absolute and normalized power (a) and thrust (b) curves for the 15 MW turbine at the New York case study site. Solid and dashed lines represent averages, while the shaded region shows the 10^{th} and 90^{th} percentile of power and thrust for the static and floating turbines.

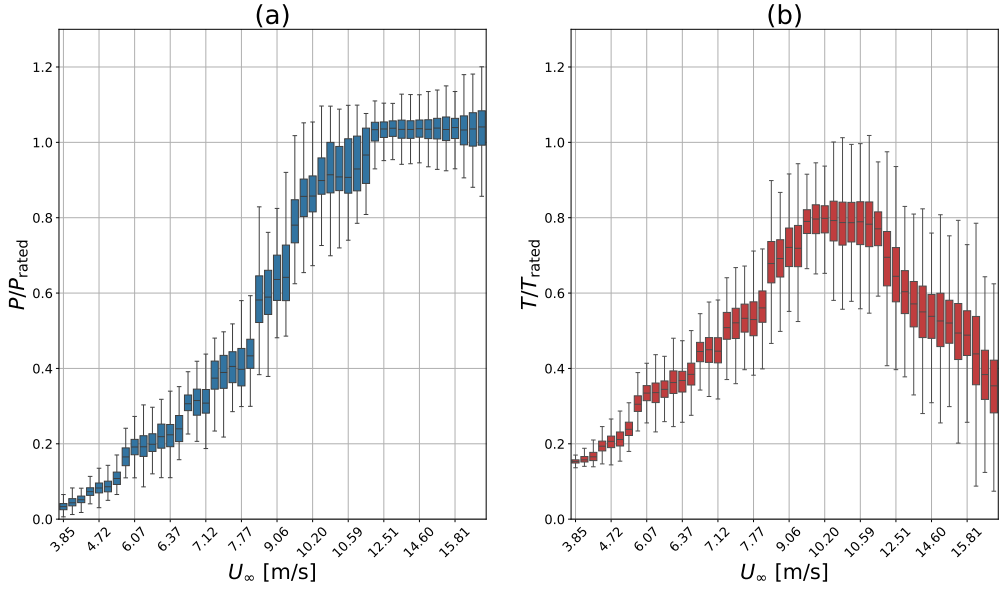

Figure 5.25: Box plot at each cluster center of the minimum, 25^{th} percentile, mean, 75^{th} percentile, and maximum of power (a) and thrust (b) for the New York case study site.

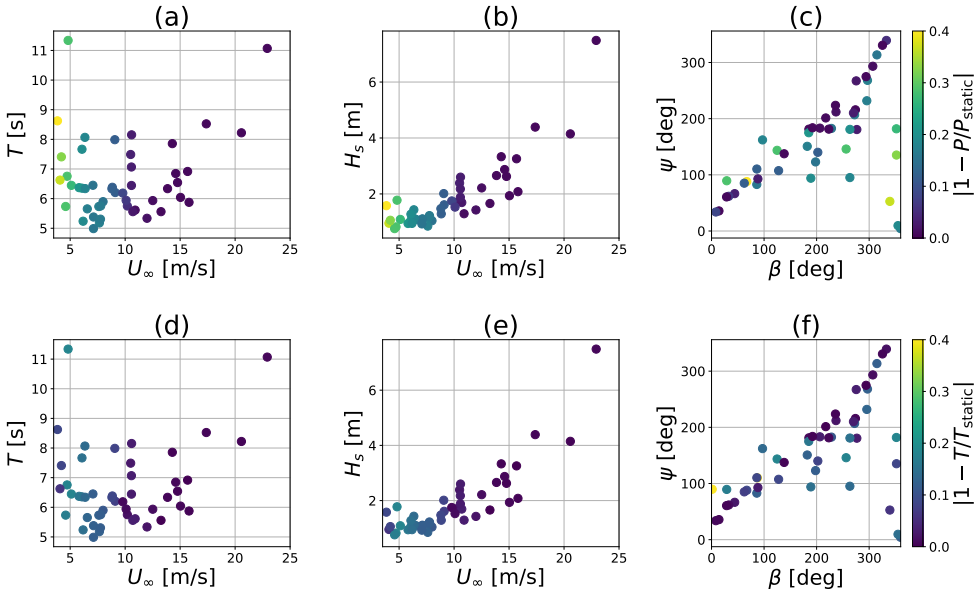

Figure 5.26: Normalized difference between FOWT power (a - c) and thrust (d - f) versus a static turbine mapped onto GMM cluster centers for the New York case study site.

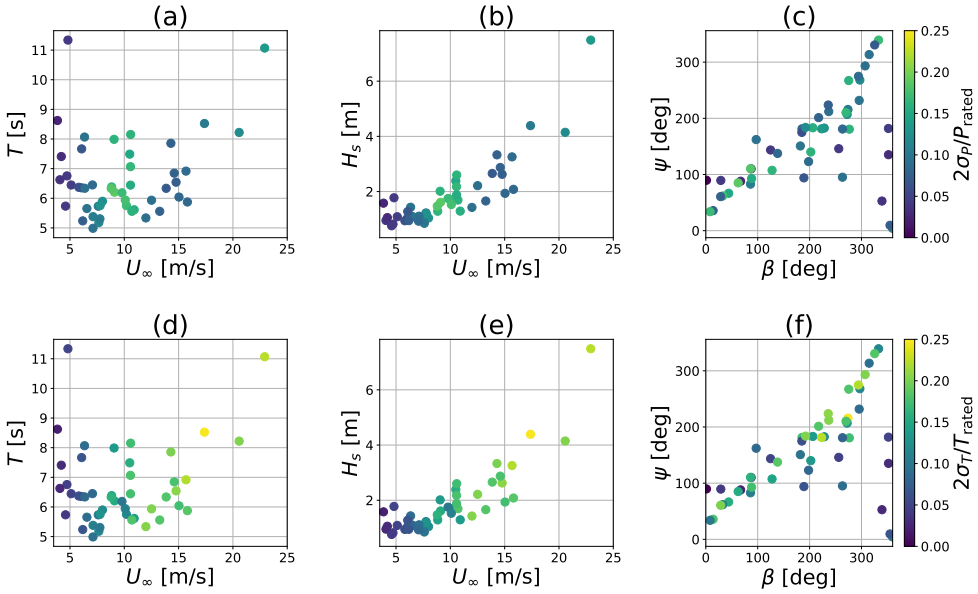

Figure 5.27: Two standard deviations of power (a - c) and thrust (d - f) normalized by rated turbine values mapped onto GMM cluster centers for the New York case study site.

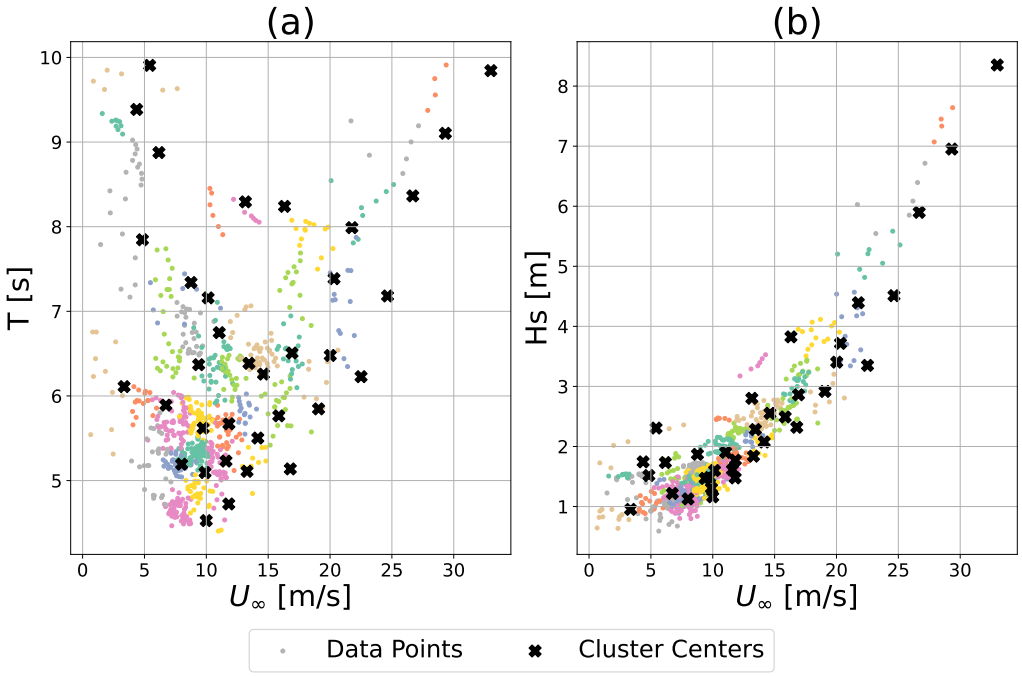

Figure 5.28: GMM cluster centers for Carolina Coast Site in wind and wave aligned conditions.

75 m. Unlike the other three case study sites, this location has not been identified for any wind energy leasing. However, it meets the other criteria outlined for case study selection in Section 5.1.

Clusters for the Carolina Coast site in wind and wave aligned conditions are shown in Figure 5.28 and for the full data set of environmental conditions in Figure 5.29. The cluster centers for the aligned data set are evenly spread across the parameter space with wind speeds between 4 and 33 m/s, significant wave heights between 1 and 8.5 m, and mean wave periods between 2.5 and 10 s. The five-dimensional data set cluster centers are more tightly spaced. Mean wave periods are between 4 and 8 s with the exception of an outlier at 11 s. Significant wave heights are between 1 and 5 m. The five-dimensional data set is the least wind and wave aligned of the four case study locations, with 20 of 50 cluster centers having a misalignment greater than 45 degrees.

Power and thrust performance curves for the Carolina Coast case study location under ideal, aligned conditions are shown in Figure 5.30, and the fluctuation in power and thrust for the wind and wave aligned data set is shown in Figure 5.31. In ideal, aligned conditions, the Carolina Coast site FOWT exhibits high power capture relative to static. FOWT power capture at 5 m/s wind speed is 38 % higher than

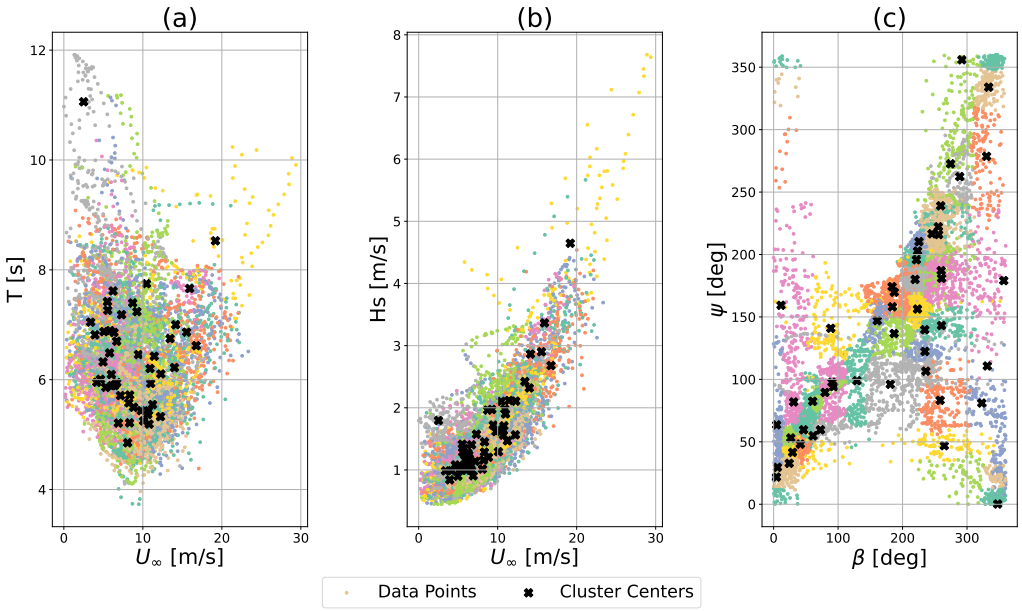

Figure 5.29: GMM cluster centers for Carolina Coast Site in all conditions.

the static baseline. This increased power generation decreases steeply to 10 % above static at 7.5 m/s. Throughout the below-rated region, the power capture varies from very close to static to far from static. This is likely due to variations in mean wave period from 3 to 10 s for cluster centers between 5 and 10 m/s. As seen in regular wave testing in Chapter 4, high frequency waves with periods under 5 s have a minimal effect on power capture at low wind speeds, where larger periods around 8 to 10 s can have a significant effect due to larger responses in the platform RAO. The power performance dip at the rated wind speed is in line with the previous case study locations, a 3 % decrease relative to static. In the below-rated region, mean rotor thrust is seen to vary from 23 % to 1 % above static turbine thrust. At the rated wind speed, FOWT mean rotor thrust is 96 % of static. The 10^{th} to 90^{th} percentile fluctuation of rotor thrust is also seen to increase with wind speed across the turbine operational wind speed range. However, the fluctuation of the FOWT is only slightly larger than that for the static turbine.

In ideal, wind-wave aligned conditions at the Carolina Coast case study site, power fluctuation is maximal near the rated wind speed with a range of 47 % of rated power at 9.5 m/s. The range at 24.6 m/s is 34 % of rated power. Thrust fluctuation peaks for high wind speeds with a range of 45 % of rated at 11.5 m/s and 58 % at 21 m/s.

Power and thrust performance curves and the fluctuation of power and thrust for the full data set at the Carolina Coast site are shown in Figures 5.32 and 5.33

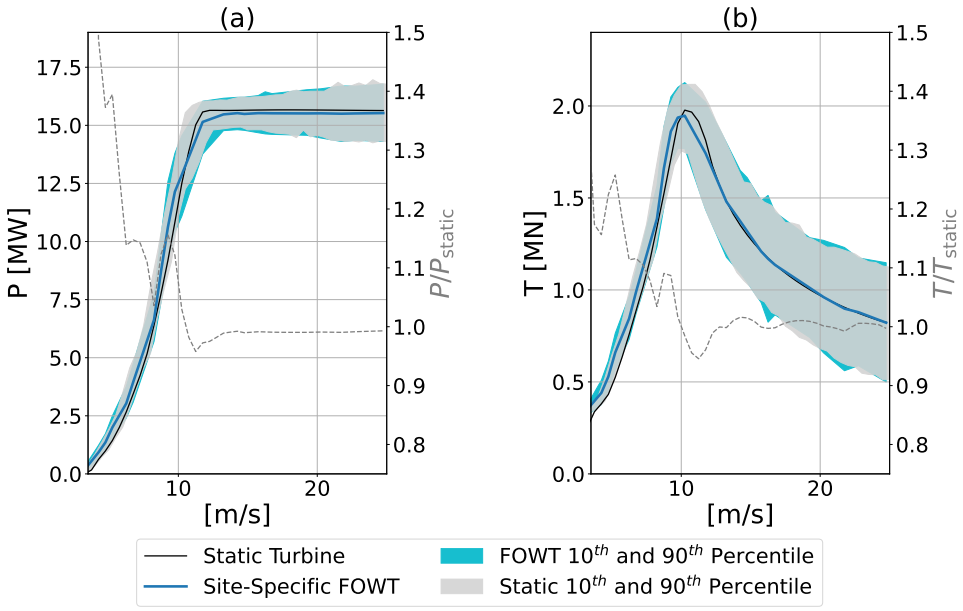

Figure 5.30: Absolute and normalized power (a) and thrust (b) curves for the 15 MW turbine at the Carolina Coast case study site in ideal wind-wave aligned conditions. Solid and dashed lines represent averages, while the shaded region shows the 10^{th} and 90^{th} percentile of power and thrust for the static and floating turbines.

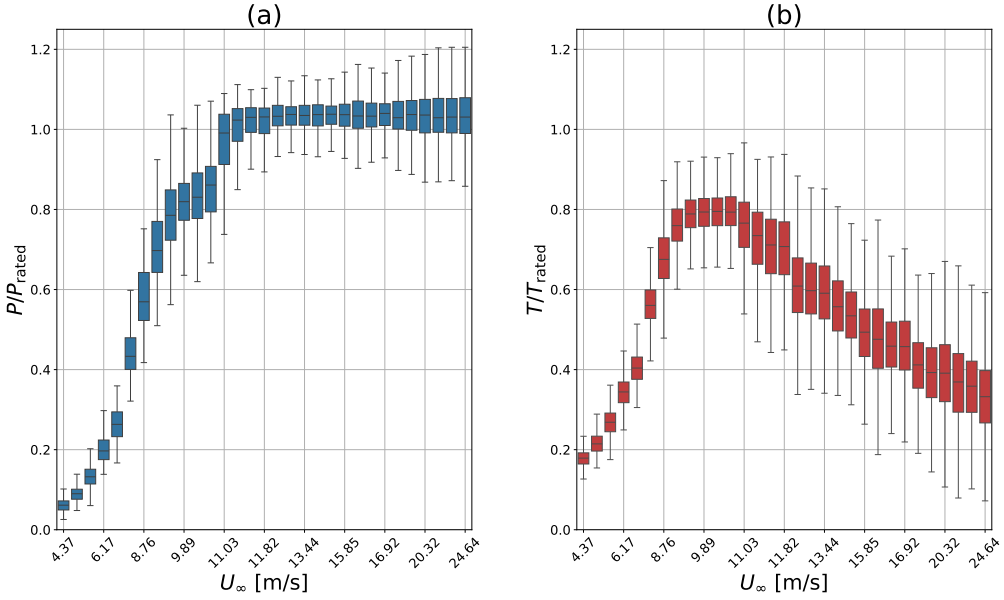

Figure 5.31: Box plot at each cluster center of the minimum, 25^{th} percentile, mean, 75^{th} percentile, and maximum of power (a) and thrust (b) for the Carolina Coast case study site in ideal wind-wave aligned conditions.

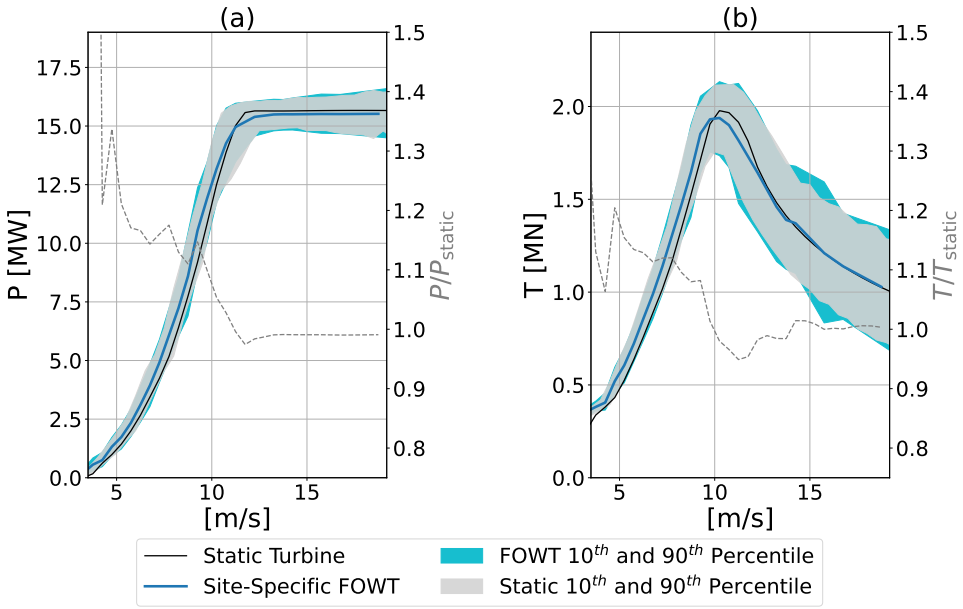

Figure 5.32: Absolute and normalized power (a) and thrust (b) curves for the 15 MW turbine at the Carolina Coast case study site. Solid and dashed lines represent averages, while the shaded region shows the 10^{th} and 90^{th} percentile of power and thrust for the static and floating turbines.

respectively. The below rated power capture of the turbine is decreased in the full data set compared to the ideal, aligned conditions. FOWT power capture compared to the static baseline is increased by 28 % at 5 m/s and 8 % at 10 m/s, compared to 38 and 9 % for the ideal conditions. Power capture at rated is also slightly decreased relative to the ideal, aligned conditions, with the FOWT capturing 3 % less power than the static turbine. Average thrust in this region varies from 17 % above static to 2 % below static at 5 and 10 m/s. The fluctuation of power is 49 % of rated at 9 m/s and 30 % at 20 m/s, while the fluctuation of thrust is 65 % of the rated turbine thrust at 11.5 m/s and 80 % at 15.5 m/s.

Finally, the normalized difference of FOWT performance relative to the static turbine baseline and the two standard deviation fluctuation of power and thrust mapped onto cluster centers for this site are shown in Figures 5.34 and 5.35. Trends discussed previously for the other case study locations remain true for the Carolina Coast site. The FOWT average power and thrust performance difference to the static baseline is the largest for low wind speeds. The fluctuation of power is large near the turbine rated wind speed, while the fluctuation of thrust increases with increasing wind speed.

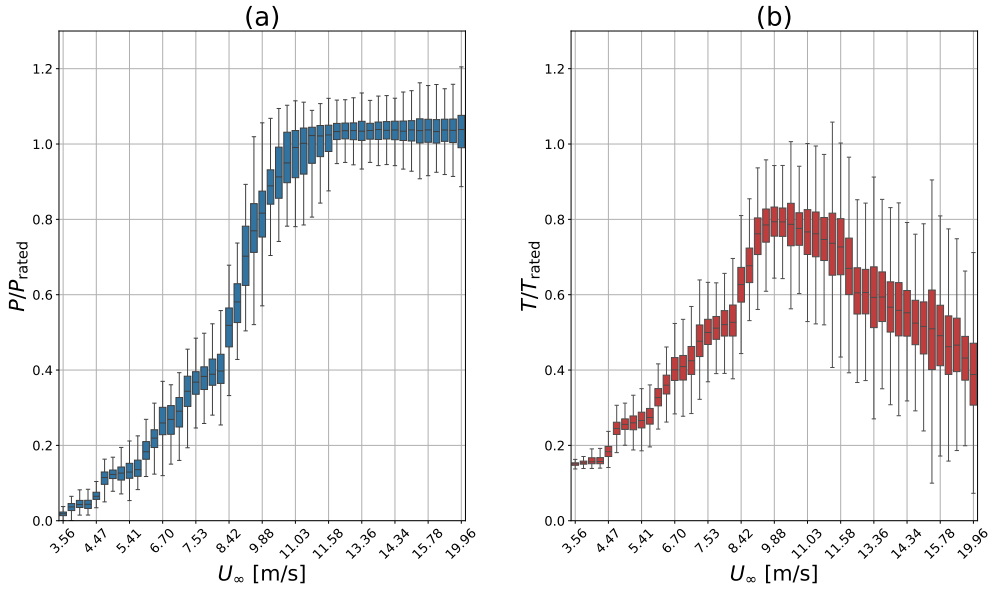

Figure 5.33: Box plot at each cluster center of the minimum, 25^{th} percentile, mean, 75^{th} percentile, and maximum of power (a) and thrust (b) for the Carolina Coast case study site.

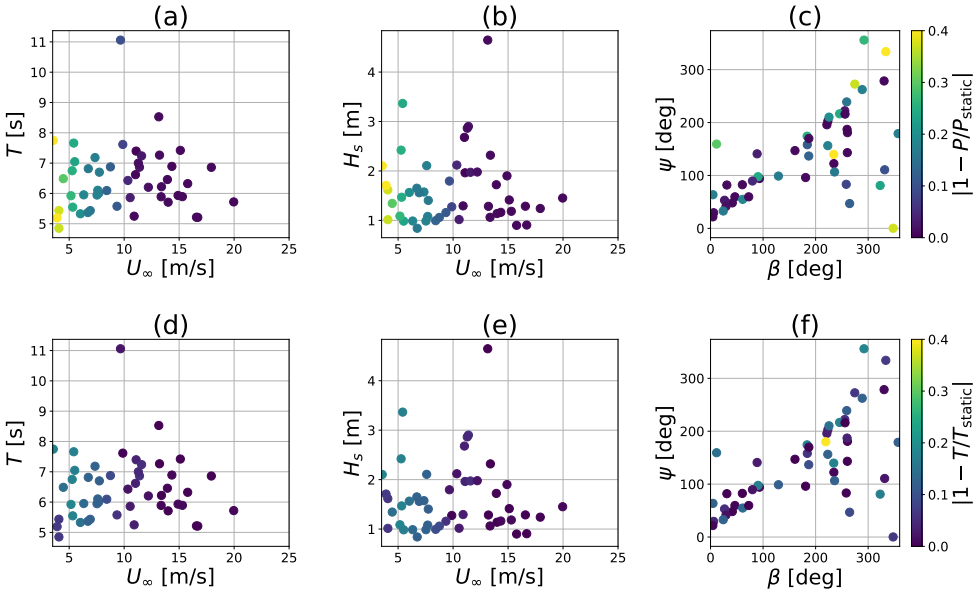

Figure 5.34: Normalized difference between FOWT power (a - c) and thrust (d - f) versus a static turbine mapped onto GMM cluster centers for the Carolina Coast case study site.

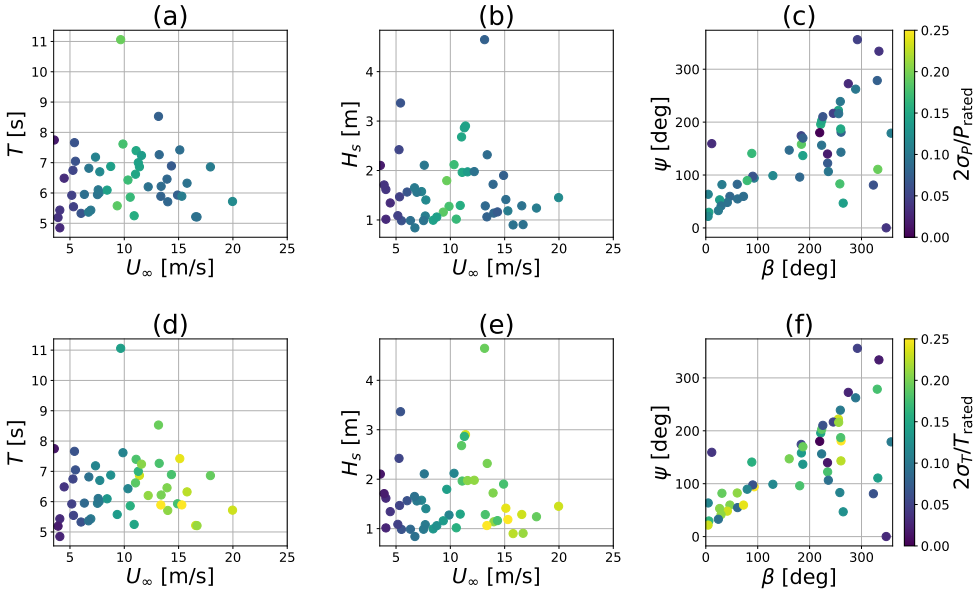

Figure 5.35: Two standard deviations of power (a - c) and thrust (d - f) normalized by rated turbine values mapped onto GMM cluster centers for the Carolina Coast case study site.

5.7 Discussion and Conclusions

Over all four case study locations, the increase in power capture relative to a static turbine in the below-rated region is decreased by the inclusion of misaligned cases. The range of significant wave heights and mean wave periods at low wind speeds in the full data set, and aligned subset of the data are similar. As described previously, wind and wave misalignment is more common at low wind speeds. As such, the decrease in average power capture at low wind speeds when including misaligned cases is most likely due to the effect of that misalignment. At 5 m/s wind speed, the inclusion of misaligned wind and wave cases reduces power capture by 5 to 15 % across the four case study locations. This result is reinforced by the findings of the misaligned regular wave cases in Chapter 4. This finding also agrees with the results of Fontanella et al. [30], who found the wave misalignment from the zero-degree heading also decreased average power capture at below-rated wind speeds. As misalignment between the wave and wind direction increases, platform motion induced by ocean waves does not cause streamwise rotor motion. Decreased streamwise rotor motion at low wind speeds decreases FOWT power capture.

The inclusion of cases in which wind and waves were misaligned from the platform zero degree heading also increases the predicted fluctuation of FOWT power

and thrust. At the Scotland and Celtic Sea sites, the ideal, aligned version of the model predicts power fluctuations of 33 % of turbine rated power slightly below the rated wind speed. The model incorporating the full parameter space predicts power fluctuations up to 50 % of rated power at those same wind speeds for the UK sites. The same is true for thrust fluctuations, which increase by an average of 0.38 MN, or 16 % of the turbine rated thrust, across the four site locations in the high-speed wind region, with the site-specific increase correlated to the number of highly misaligned cases. As a percent of the turbine rated power and thrust, wind-wave misalignment can cause an increase of 38 % and 20 % to the maximal range of power and thrust respectively. Bachynski et al. [105] found that wave misalignment from the zero degree heading decreased thrust loads on a FOWT with semi-submersible platform. They note that some non-zero incident wave angles induced greater platform motions than waves incident at zero degree heading. However, Bachynski et al. assumed a wind direction of zero degrees for all test cases, so this additional motion did not cause fluctuations in the streamwise rotor velocity and thus thrust loads. In contrast, our results consider wind and waves with misalignment and non-zero degree heading, and uncover possible high load scenarios in these types of conditions.

This emphasizes the importance of considering misaligned cases for the evaluation of turbine extreme loads. It also suggests that wind and wave misalignment will contribute to component fatigue damage. Sites such as the Carolina Coast, with more frequent misaligned conditions, may result in higher maintenance costs and decreased turbine lifespan. In general, we find that misaligned wind and waves decrease overall floating turbine performance by decreasing power capture and increasing maximum and fluctuating loads.

In all four case study sites, the site-specific power curves show a non-zero power generation at the cut-in wind speed of 3 m/s. The power capture at cut-in of the four case study power curves is larger than that for the FOWT power curves in still seas shown in Section 4.3.3. The rated turbine power at this wind speed is zero, and the fixed-bottom turbine baseline does not generate power at the cut-in wind speed. The power generated by FOWTs at the cut-in wind speed is small: approximately 5 % of the turbine rated power. However, this demonstrates the ability of the FOWT to act as a wave energy converter. Even in wind speeds at which the wind turbine generator would not produce power, wave-induced motion causes enough rotor motion that the effective wind speed is above cut-in. Power generation at cut-in, and generally improved power capture at low wind speeds, could allow FOWTs to have a larger capacity factor relative to static turbines. Additionally, FOWTs may

be beneficial in dealing with low wind speed events or lulls, a serious challenge to grid de-carbonization [106], as they can generate some power even at very low wind speeds. However, it is important to note that wind turbine power generation at near cut-in wind speed is heavily affected by shut-down and start-up control routines which have not been accounted for in this work. From these results alone, it is not clear that floating turbines will have significantly different cut-in power generation compared to static turbines in real-world operation taking into account the operational restrictions of near cut-in power generation.

Comparing the site-specific performance curves of the four case study locations to one another, we present tabulated results of the FOWT average power and thrust normalized by the static turbine performance at four wind speeds in Tables 5.3 and 5.4. The ScotWind site has a 31.4 % increase in average power capture relative to the static turbine baseline, at 5 m/s wind speed. The Celtic Sea and Carolina Coast sites perform the next best in average power capture at that wind speed, achieving a 30.6 and 28.1 % increase relative to static, respectively. This is followed by the New York site at 22.7 %. Variations between the sites are due to differences in the wave conditions of the site-specific GMM clusters at these wind speeds. At 11.5 m/s wind speed and above, the four sites become very similar, performing within 2 % of each other. The ScotWind, Celtic Sea, and Carolina Coast sites also generate similar levels of turbine load fluctuation: a range of 48 to 51 % of turbine rated power in power fluctuation between 9 and 10 m/s and a range of 78 to 80 % of rated in thrust fluctuation between 15 and 16 m/s. The New York site generates smaller fluctuations of power and thrust: 40 and 69 % of rated, respectively. For all of the case study sites, the load fluctuations due to wind speed turbulence for the static turbine are large. Platform motion in FOWTs increases power and thrust fluctuation. However, the largest variations in power and thrust are still due to wind speed turbulence. The greatest power and thrust fluctuations due to platform motion occur at above rated wind speeds.

To further characterize variation between sites, we show average power and thrust coefficients for all locations in Figure 5.36. Variation between the sites is up to 0.07 in C_P and C_T. In Figure 5.36 and Tables 5.3 and 5.4, it is clear that differences in turbine average power and thrust performance between sites are not significant. However, all four locations exhibit similar performance differences relative to the static turbine, and the difference in performance between static and FOWT is significant. Average power and thrust coefficients of the FOWT in all four locations exceed the static baseline across the below-rated region. As mentioned previously, this phenomenon

Ideal, Aligned Subset of Data (3D)				
Site	5 m/s Power	8 m/s Power	11.5 m/s Power	16 m/s Power
ScotWind	+45.0 %	+17.4 %	-3.18 %	-0.810 %
Celtic Sea	+33.0 %	+17.5 %	-2.59 %	-0.900 %
New York	+22.7 %	+15.7 %	-2.77 %	-0.690 %
Carolina Coast	+38.2 %	+7.20 %	-4.25 %	-0.870 %
Full Data Set (5D)				
Site	5 m/s Power	8 m/s Power	11.5 m/s Power	16 m/s Power
ScotWind	+31.4 %	+17.3 %	-3.01 %	-0.990 %
Celtic Sea	+30.6 %	+11.8 %	-2.47 %	-0.870 %
New York	+19.9 %	+16.7 %	-2.23 %	-0.870 %
Carolina Coast	+28.1 %	+15.3 %	-2.65 %	-0.930 %

Table 5.3: FOWT average power capture normalized by static power capture at 5, 8, 11.5, and 16 m/s wind speeds. Results are presented as percentage difference from the static turbine baseline.

Ideal, Aligned Subset of Data (3D)				
Site	5 m/s Thrust	8 m/s Thrust	11.5 m/s Thrust	16 m/s Thrust
ScotWind	+28.4 %	+11.8 %	-4.85 %	+0.200 %
Celtic Sea	+22.0 %	+12.1 %	-6.98 %	+1.40 %
New York	+16.0 %	+11.5 %	-6.27 %	+1.50 %
Carolina Coast	+24.0 %	+5.70 %	-5.44 %	-0.160 %
Full Data Set (5D)				
Site	5 m/s Thrust	8 m/s Thrust	11.5 m/s Thrust	16 m/s Thrust
ScotWind	+20.4 %	+11.6 %	-4.25 %	+0.100 %
Celtic Sea	+17.4 %	+8.80 %	-5.56 %	+0.900 %
New York	+13.7 %	+11.8 %	-6.33 %	-0.160 %
Carolina Coast	+17.5 %	+10.7 %	-5.20 %	+0.100 %

Table 5.4: FOWT average rotor thrust normalized by static rotor thrust at 5, 8, 11.5, and 16 m/s wind speeds. Results are presented as percentage difference from the static turbine baseline.

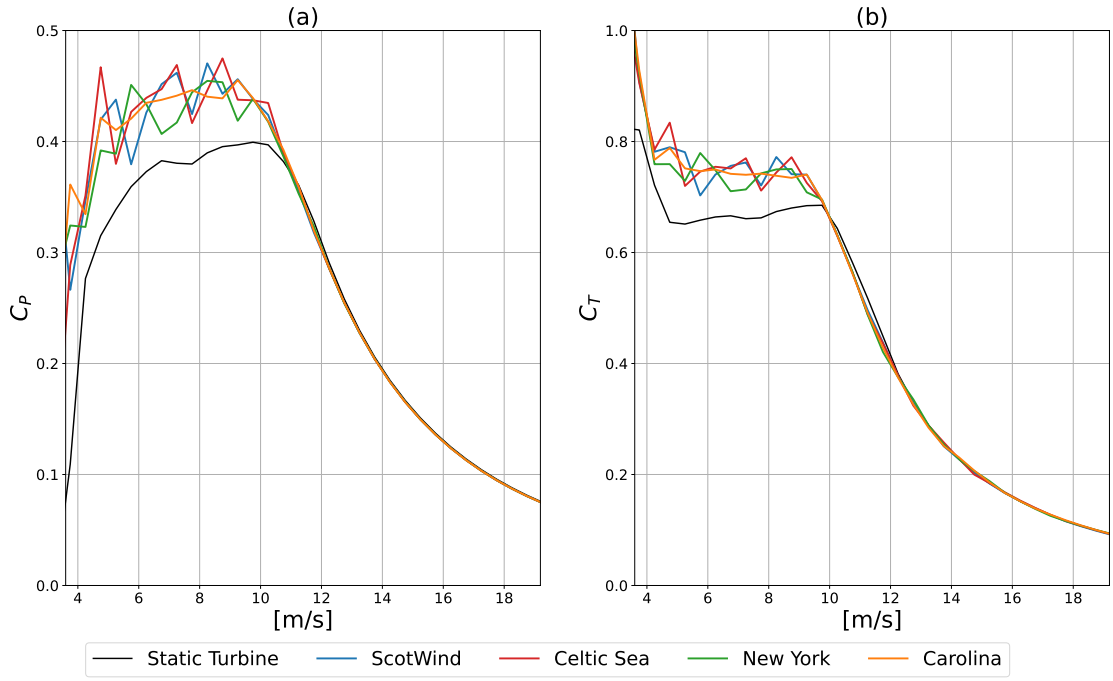

Figure 5.36: Power coefficient (a) and thrust coefficient (b) versus freestream wind velocity for the four case study locations and for the fixed-bottom turbine baseline.

is due to the biased mean of the power signal which is cubically related to the wind speed, a mean offset sinusoid, and has been described by multiple authors [26], [30], [107]. All four sites converge to a power and thrust coefficient slightly below the fixed bottom baseline at the rated wind speed. At high wind speeds, all four sites and the static turbine have almost identical power and thrust coefficients.

To compare long-term power performance of a prospective floating turbine in each of the four site locations, we compute the site-specific AEP. The site-specific Weibull wind speed distributions and AEPs are shown in Figure 5.37. As seen in Figure 5.36, there is some variation in average power coefficient between case study sites, but in general the average power performance relative to a static turbine is similar. The annual energy production of each site correlates with the probability of low wind speeds as shown in the Weibull distributions. The ScotWind site has the largest Weibull distribution peak wind speed, and thus the largest predicted AEP. However, when the site-specific AEP is normalized by the AEP of a static turbine at that same site, we see the inverse correlation. As shown in the site-specific power curves above, FOWTs outperform static turbines in low wind speed conditions. The magnitude of this over-performance varies based on other environmental parameters, but is always present. As such, floating turbines will tend to return higher AEPs than

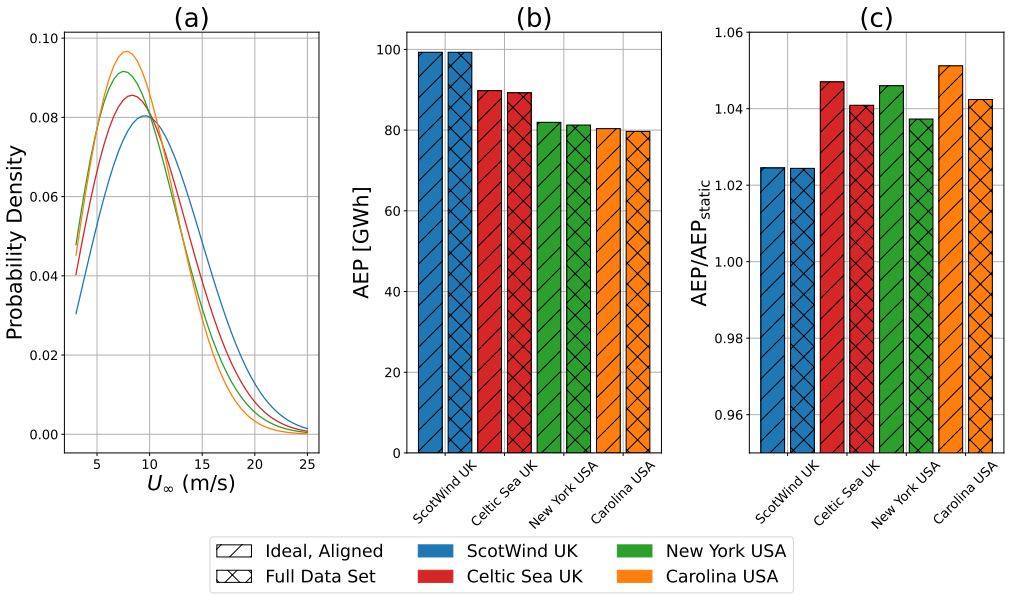

Figure 5.37: Best fit Weibull wind speed distribution (a), annual energy production (b), and normalized annual energy production (c) for the four case study locations.

static turbines in sites dominated by low wind speeds. This suggests that turbines, floating or fixed, should always be placed in locations with the highest possible wind speeds. However, if available sites are dominated by low wind speeds, a floating turbine will outperform a fixed-base turbine.

As discussed in Section 5.1, Fontanella et al. [30] used OpenFast to predict the AEP of the IEA 15 MW RWT in the Mediterranean Sea off of the French coast. Their modeling predicted a static turbine AEP of 46.7 GWh and a floating turbine AEP within 1 % of the static performance. The site-specific AEPs predicted here are much larger. This is due to the extremely low wind speed of the Mediterranean Sea case study site. The best-fit Weibull wind speed distribution for the site peaks under 4 m/s. The cut-in wind speed of the IEA 15 MW RWT is 3 m/s, so a wind turbine at the site studied by Fontanella et al. will be below cut-in and inactive for a significant portion of the year.

In addition to AEP, the capacity factor for the FOWT at the four sites is shown in Table 5.5. The ScotWind site has a significantly higher capacity factor compared to the other three sites. This is driven by the very high average wind speed distribution at the site. The ScotWind site has a peak in its best fit Weibull wind speed distribution of 9.8 m/s. Additionally, the toe (probability density at high wind speeds) of the distribution is large relative to the other three case study locations. As such, the

Site	FOWT	Static
ScotWind	0.756	0.738
Celtic Sea	0.679	0.652
New York	0.618	0.596
Carolina Coast	0.606	0.582

Table 5.5: Capacity factor over the calender year 2024 for the reference FOWT and static turbine in each case study location.

ScotWind site experiences wind speeds near or above the turbine rated wind speed for much of the year. This results in the high site-specific AEP and capacity factor. It also demonstrates that the ScotWind Ossian lease site is a highly productive potential development site for wind energy.

We see a similar trend as that identified in the site-specific AEP, where FOWT capacity factor is driven by the wind speed distribution of the site. Sites with higher average wind speeds exhibit higher floating and static capacity factors. Carreno-Madinabeitia et al. [108] modeled wind turbine capacity factor of the NREL 5 MW RWT in the Iberian Peninsula using ERA 5 and ERA-20C reanalysis data, finding capacity factors between 0.4 and 0.6. The capacity factors presented here are large in comparison, all exceeding 0.6. However, Carreno-Madinabeitia et al. calculate the capacity factor with an empirical equation based on rotor diameter. Their expression for the capacity factor increases as rotor diameter increases. As the rotor diameter of the IEA 15 MW RWT is roughly twice that of the 5 MW RWT we expect significantly larger capacity factors in our study. It is important to note that we assume 100 % turbine availability over the course of the year 2024. As such, we do not account for any turbine downtime due to routine maintenance, inspections, etc. We expect the capacity factor to decrease when this expected downtime is taken into account.

Also apparent is that in all four case study locations the FOWT model outperforms the static turbine baseline in terms of power capture. This ranges from a 2.4 to 4.3 % increase in AEP across the four sites as compared to static. The capacity factors for the floating turbine are also larger than the static capacity factors at all four sites. As mentioned previously, this is coupled with an increase in fluctuating loads. Based on these results, concerns about FOWT deployment should not be focused on decreased power capture compared to a fixed-bottom turbine. Instead, the main drawback of the FOWT technology is the increase in fluctuating loads which will contribute to blade, tower, and drivetrain fatigue damage. This increased fatigue damage can occur across the operational wind speed range as evidenced in Figures 5.11, 5.19, 5.27, and 5.35 where peak fluctuation of power occurs at low wind speeds while peak fluctuation

of thrust occurs at high wind speeds. As rotor thrust is more likely to result in blade and tower loading, we can expect that increased fatigue damage will occur at high wind speeds for those components. As mentioned in Section 5.1, Marin et al. [86] and Ravikumar et al. [87] identified wind turbine blades as prone to failure by fatigue damage induced cracking. As such, this high wind speed regime where thrust load fluctuation is high, and wind speed turbulence is high, will contribute significantly to blade damage. In contrast, increased fatigue to drivetrain components such as the main shaft, slip disk, and generator coupling will occur at below rated wind speeds.

Chapter 6

Summary and Conclusions

In Chapter 2, an extensive validation of an in-house blade element momentum theory code was undertaken. This validation campaign compared the low-fidelity BEMT solver to two experimental models and one high-fidelity RANS-CFD solver. Compared to a blade-resolved, RANS-CFD model, the BEMT model achieved 3 to 9 % root mean square error in the prediction of average and fluctuating components of turbine power and thrust coefficients. Compared to small-scale, experimental models, this error increased to be between 18 and 48 %. As discussed in Chapter 2, the highest error of 48 % may be due to measurement errors in the experimental modeling campaign. Comparing multiple corrections for blade element momentum theory, we concluded that there was no indication that dynamic inflow corrections would improve BEMT accuracy in predicting rotor integrated parameters. This conclusion was supported with the relevant literature and the validation results presented. Additionally, our work revealed drawbacks to the performance scaling experimental methodology, including uncertainty regarding its capacity to reproduce the transient dynamics of the full-scale system. From the validation work conducted, we conservatively expect the BEMT aerodynamic solver presented to operate with 10 to 20 % error relative to higher fidelity models.

In Chapter 3, turbine performance under a prescribed harmonic motion at natural frequencies of two representative floating platforms and a representative wave frequency of varying amplitude is analyzed. These results demonstrate a significant increase in turbine power capture, up to 160 % of the static baseline, in the below-rated wind speed region. Fluctuations of rotor thrust of over 50 % of the turbine rated thrust are also predicted. The effect of prescribed motion on turbine performance was dependent upon both the frequency and amplitude of motion. The representative wave frequency was seen to result in the largest increases in average power capture at low wind speeds. The result that motion at a representative wave

frequency results in enhanced FOWT power capture at low wind speeds should be highlighted, as platform motion at ocean wave frequencies will occur frequently during operation. Importantly, the below-rated increase in power capture and high thrust fluctuations are significant relative to our estimated error. The work presented in Chapter 3 provides a method for adjusting typical turbine performance curves to account for FOWT platform motion. With relatively little computational expense, the turbine power curve which is used for almost all site selection and wind resource assessment methods can be adjusted to account for platform motion effects.

In Chapter 4, a coupled aero-hydrodynamic model predicted an increase in turbine power capture compared to a static turbine of over 20 % under regular wave loading at a representative wave period of 11 s. The coupled model also predicted fluctuations of turbine thrust of over 70 % of the turbine rated thrust for these same wave conditions. Again, these trends in average power capture and rotor thrust fluctuation are significant relative to the uncertainty of the BEMT model. Additionally, we find that turbine performance is dependent on the regular wave frequency. Frequencies corresponding to the response maxima in the floating platform RAO are found to cause a greater change in turbine performance. 0.125 Hz frequency waves are identified as causing maximal fluctuations in turbine power and thrust as well as being a local maxima for regular wave loading's effect on average power and thrust. We also show that the amplitude of turbine power and thrust scales linearly with regular wave amplitude. The turbine average power capture and average rotor thrust exhibit non-linear behavior due to the turbine's controller. Average power capture in the below-rated region is shown to scale close to cubically with wave amplitude, mirroring the basic formulation of wind turbine power capture as a function of wind speed.

This work is continued in Chapter 5, where turbine performance in realistic sea-state conditions for four case study locations in the United States and United Kingdom is analyzed. Again, increases in floating turbine power capture of up to 45 % relative to the static baseline and fluctuations of rotor thrust greater than 50 % of the rated thrust are measured. The general agreement between prescribed harmonic motion, regular wave loading, and realistic irregular wave loading is noteworthy, supporting the supposition that low-fidelity, non-coupled models are still useful for analysis of FOWT performance. Additionally, the trend identified of floating turbines outperforming static turbine power capture at low wind speeds is significant relative to the aerodynamic model's uncertainty. The same is true for the trend identified that large fluctuations of rotor thrust will occur for floating turbines at near-rated

and high wind speeds. As noted in Chapter 5, this increase in power capture at wind speeds below 10 m/s, which are common at most offshore sites, allows FOWTs to generate the same or better annual energy production than their static counterparts. The difference between the four case study sites in power and thrust coefficient, and in average power and thrust normalized by static turbine performance, is not significant relative to the BEMT model's uncertainty. As such, our model predicts that site-specific performance variation is not significant within the four case study locations selected here.

Between the case study sites, FOWT predicted AEP was driven by the site-specific wind resource. Sites with higher average wind speeds were predicted to have a larger AEP. When considering FOWT performance relative to a fixed-bottom turbine in the same location, we found that FOWTs in sites with lower average wind speeds had higher AEPs relative to the static turbine baseline. This increase in AEP is due to the increased power capture at low wind speeds in FOWTs relative to fixed-bottom turbines. This suggests that in sites dominated by low wind speeds, a floating turbine will outperform a fixed-base turbine.

Examining the effect of wind and wave misalignment on turbine performance, we found through regular wave testing that wind-wave misalignment decreases power capture at below-rated wind speeds. Additionally, wind and waves coming from a 90 degree heading relative to the platform induced greater decreases in power capture at the rated wind speed relative to waves coming from a zero degree heading. In the irregular wave case studies, we compared a subset of the data containing only idealized, wind-wave aligned conditions, to the full data set. Simulation of this ideal, aligned subset was shown to result in higher power capture in the below rated wind speed region and lower fluctuations of turbine thrust relative to the full, misaligned data set. From both our exploration of regular waves and realistic irregular sea-states we conclude that misalignment is detrimental to turbine average power capture and causes larger load fluctuations. This load fluctuation will likely result in greater fatigue damage and increase turbine maintenance and downtime. Wind-wave misalignment is shown to generally decrease FOWT performance and should be taken into consideration in site-selection procedures. Despite this, even in the Carolina Coast case study site which had the highest number of cluster centers with greater than 45 degree wind-wave misalignment, the FOWT AEP was larger than the static AEP.

It is important to note that this work is based on low-fidelity aerodynamic and hydrodynamic modeling. As discussed above, we characterized the error of the in-

house BEMT solver used for aerodynamic modeling and conservatively expect BEMT to operate with 10 to 20 % error. With this in mind, we identify the increase in FOWT average power capture by 20 to 40 % relative to a fixed-bottom turbine at low wind speeds as significant relative to our margin of error. We also identify the thrust fluctuations between 60 and 80 % of the turbine rated thrust in the high wind speed region as significant relative to our margin of error. Our prediction of the FOWT AEP exceeding static turbine AEP by 2–4 % is a function of FOWT power generation at each wind speed, so it is sensitive to BEMT uncertainty. However, the predicted AEP increase is based on increased average power capture at low wind speeds, which is found to be significant relative to the BEMT error. However, other work has found that the IEA 15 MW RWT with a semi-submersible platform has a predicted AEP within 1 % of a static turbine [30]. As such, we conclude that floating turbine AEP is likely to be similar to static turbine AEP. In general, the results presented have a margin of uncertainty due to the low-fidelity nature of the model used. To achieve a more exact prediction of FOWT performance in a set of wind and sea state conditions, a higher fidelity model would be required. However, in that case, far fewer combinations of aerodynamic and hydrodynamic loading would have been considered, and large-scale trends in performance would not have been able to be identified.

From results presented in this work from prescribed harmonic motion, regular wave, and irregular wave loading cases, we conclude that floating offshore wind turbines will not lack in power generation compared to fixed-bottom turbines. Instead, the main drawback of floating technology will be the increase in load fluctuation and resulting fatigue damage and increase in maintenance requirements. Based on the wind speeds where the most load fluctuation occurs, we can predict where fatigue damage will accumulate. For components which are primarily loaded by rotor thrust, such as the turbine tower and blades, fatigue damage due to large load cycling will accumulate during high wind speeds. For components primarily loaded by rotor torque, such as the main shaft, generator coupling, and generator mount, fatigue damage will be large during wind speeds near rated. Our findings on the effect of platform motion on turbine load fluctuation are qualified by there being only one platform type analyzed here, where other platforms may behave differently. However, the UMaine Volturn-US is widely representative of potential FOWT platform technologies, and floating platforms broadly will always have motion responses at incoming wave frequencies.

Low fidelity models are not only useful but necessary in FOWT design. The FOWT system has added required modeling complexity as all wave conditions and

all realistic combinations of wind and wave conditions must be explored. As seen in this work, small variations in combinations of wind and sea-state can have large effects on turbine performance. As such, computationally inexpensive tools are required to explore the large number of possible variations in FOWT operational conditions. As we have presented, comparison of these low-fidelity models to experimental studies can be challenging. In particular, creating scale models of FOWT performance is challenging due to the competing scaling requirements of the system aerodynamics and system hydrodynamics. The best-case scenario of validation would be the comparison of multiple models of varying fidelity to performance data of installed floating turbines, such as those in the Hywind Scotland or Portugal WindFloat farms. Unfortunately, performance data from these turbines is generally proprietary and protected. However, we would urge academic partnerships with industry that could result in validation of typical models with real-world turbine data wherever they are possible. Large scale, onshore, turbine models have been constructed by the United States National Renewable Energy Laboratory and used for validation of models for onshore turbines. A similar project for floating turbines would have a large impact in validating low fidelity models for FOWTs.

Generally, we have shown that the power performance and component loading of a FOWT can be significantly different from that of a fixed-bottom turbine. Additionally, this performance difference is dependent upon specific environmental parameters that affect the motion of the FOWT coupled aero-hydrodynamic system. The typical design methodology for fixed wind turbine rotors looks at a discrete number of design load cases which include operational and extreme wind conditions. These results suggest that this typical design methodology, which was developed for onshore wind turbines and adapted to fixed offshore wind turbines, may not be appropriate for FOWTs, as any aerodynamic design load cases must be coupled with an appropriate sea state. Moreover, we have shown that variation in the sea state, even with the same aerodynamic loading, can cause significant variation in FOWT performance. The combinations of wind and sea state loading that have the greatest effect on FOWT performance will likely be related to the specific hydrodynamic properties of the floating platform. As such, creating generalizable design load cases for all FOWTs will be challenging. Instead, FOWT design methods will likely have to model performance and safety over a wide range of sea states, possibly in the frequency domain.

The large performance difference between FOWTs and static turbines in specific operating conditions also suggests that further optimization in FOWT technology could occur. As mentioned above, FOWT performance in specific sea states will be

determined by the frequency dependent motion response of the platform. FOWT platform designs vary widely, suggesting that many design morphologies are feasible. This leaves a large design space for optimization of the platform. Furthermore, site-specific platform optimization, creating platforms with desired motion responses at typical wave conditions of the site, could result in large performance gains. Similar optimizations could be conducted for the turbine controller. Specifically, FOWT's capture increased power relative to a fixed bottom turbine at low wind speeds and decreased power at near-rated wind speeds. As turbine controllers are typically gain scheduled according to the wind speed region, significantly different controller behavior in these two regions is possible. Development of FOWT controllers that allow streamwise rotor motion at low wind speeds, but minimize it at higher wind speeds, would maximize a floating turbine's performance.

Based on the results presented, sea-state variation between case study sites did not result in significantly different average power or thrust coefficients for a large floating turbine. However, future work should be undertaken to explore further possible installation sites for FOWTs. Sites with varying water depth, or more frequently misaligned wind and wave conditions due to currents, could yield different results. This work also did not consider wave directional spreading or interactions between wave groups propagating in different directions. The results of this work are valid for the assumption of unidirectional, irregular waves. As many ocean states can be approximated with this model, these results are indicative of FOWT performance, but may not generalize to all sea states. Longer time periods than one year should also be modeled. For our purposes, we utilized one year of ERA 5 reanalysis data to generate representative sets of environmental parameter data. However, annual variation could skew results. Turbines are expected to operate for 15-25 years, so larger data sets could be helpful in better characterizing performance over these time spans. Additionally, coupled modeling, such as the methodology presented here, can be utilized to examine site-specific performance of various turbine design options. For example, comparing the performance of varying platform types, or turbine controllers within the context of a site-specific environmental parameter set. The work presented here has demonstrated the opportunity for FOWTs to have enhanced power capture compared to fixed-bottom turbines. This additional power capture is at the cost of increased turbine load fluctuation. However, increased FOWT power capture occurs in a different wind speed regime than the increased power or thrust fluctuation, so control strategies which can maintain this below rated increase in power capture while minimizing fluctuating loads at higher wind speeds should be explored. This would

be a significant contribution to floating wind turbine technology. It is important to note that this work was based on a BEMT aerodynamic model that did not track individual blade position or individual blade inflow characteristics. Additionally, the aerodynamic model did not consider tower shadow or blade passing effects. The assumption of uniform inflow velocity between the three turbine blades and no blade passing load effects means that the load fluctuation described in these results is indicative of average load fluctuations across the rotor, but not necessarily of effects on an individual blade level. The same is true of the assumption of uniform turbulence across the rotor plane; load fluctuation in this work is indicative of average load fluctuation, but not localized loading. However, the observation that average load fluctuation will increase for FOWTs compared to static turbines is still significant and highly relevant to FOWT design. Through our regular wave testing we also identified frequencies at which platform motion and turbine performance responses are maximum. Based on these results, future work in FOWT platform and turbine design which conducts optimizations in the frequency domain can be narrowed to focus on the frequencies of interest we have identified. In this work, load fluctuation was used as a proxy for turbine component fatigue damage. Although this is helpful for making broad comparisons between floating and static turbine performance, a more quantitative analysis of blade or tower fatigue damage due to rotor thrust variation is needed.

References

[1] M. Collins, R. Knutti, J. Arblaster, J.-L. Dufresne, T. Fichefet, P. Friedlingstein, X. Gao, W. J. Gutowski, T. Johns, G. Krinner, M. Shongwe, C. Tebaldi, A. J. Weaver, M. Wehner, Long-term climate change: Projections, commitments and irreversibility, in: T. F. Stocker, D. Qin, G.-K. Plattner, M. Tignor, S. K. Allen, J. Boschung, A. Nauels, Y. Xia, V. Bex, P. M. Midgley (Eds.), Climate Change 2013: The Physical Science Basis. Contribution of Working Group I to the Fifth Assessment Report of the Intergovernmental Panel on Climate Change, Cambridge University Press, Cambridge, United Kingdom and New York, NY, USA, 2013.

[2] S. Rodrigues, C. Restrepo, E. Knotos, R. T. Pinto, P. Baur, Trends of offshore wind projects, Renewable and Sustainable Energy Reviews 49 (3) (2015) 1114–1135.

[3] Global Wind Energy Council, GWEC global wind report 2023 (2023).
URL `https://gwec.net/wp-content/uploads/2023/04/GWEC-2023_interactive.pdf`

[4] Global Wind Energy Council, Floating offshore wind a global opportunity (2022).
URL `https://gwec.net/wp-content/uploads/2022/03/GWEC-Report-Floating-Offshore-Wind-A-Global-Opportunity.pdf`

[5] R. Meier, E. L. Davin, G. B. Bonan, D. M. Lawrence, X. Hu, G. Duveiller, C. Prigent, S. Seneviratne, Impacts of a revised surface roughness parameterization in the community land model 5.1, Geosci. Model Dev. (2022).

[6] P. A. Hwang, Ocean surface roughness from satelite observations and spectrum modeling of wind waves, Journal of Physical Oceanography (2022).

[7] E. Edwards, A. Holcombe, S. Brown, E. Ransley, M. Hann, D. Greaves, Evolution of floating offshore wind platforms: A review of at-sea devices, Renewable and Sustainable Energy Reviews 183 (2023).

[8] Equinor, Hywind tampen (2023).
URL https://www.equinor.com/energy/hywind-tampen

[9] Offshore Wind Scotland, Floating wind in Scotland, (2023).
URL https://www.offshorewindscotland.org.uk/the-offshore-wind-market-in-scotland/floating-wind-in-scotland/#:~:text=Floating%20Wind%20in%20Scotland,-Information%20on%20floating&text=Scotland%20is%20a%20world%20leader,become%20the%20world's%20largest%20project.

[10] EDP, WindFloat atlantic floating offshore wind-power generating platform (2023).
URL https://www.edp.com/en/innovation/windfloat

[11] R. Wiser, K. Jenni, J. Seel, E. Baker, M. Hand, E. Lantz, A. Smith, Expert elicitation survey on future wind energy costs, Nature Energy (2016).

[12] M. Lerch, M. De-Prada-Gil, C. Molins, G. Benveniste, Sensitivity analysis on the levlized cost of energy for floating offshore wind farms, Sustainable Energy Technologies and Assessments (2018).

[13] G. Barter, A. Robertson, W. Musial, A systems engineering vision for floating offshore wind cost optimization, Renewable Energy Focus (2020).

[14] C. Qun, X. Longfei, C. Zhengshun, L. Mingyue, W. Binrong, Operational and extreme responses of a new concept of 10MW semi-submersible wind turbine in intermediate water depth: An experimental study, Ocean Engineering (2020).

[15] B. Wang, Y. Li, S. Gao, K. Shen, Z. Hu, X. Zheng, Motion characteristics and aero-elastic responses of floating offshore wind turbine under coupling action of waves and wind, Frontiers in Enviornmental Science 10 (2022).

[16] Technical Committee TC 88 Wind energy generation systems, IEC61400-3-1, Tech. rep., International Electrotechnical Commission (2019).

[17] M. Shafiee, Extending the lifetime of offshore wind turbines: challenges and opportunities, Energies (2024).

[18] Y. Liu, Q. Xiao, A. Incecik, C. Peyrard, D. Wan, Establishing a fully coupled CFD analysis tool for floating offshore wind turbines, Renewable Energy 112 (2017).

[19] T. Tran, D. Kim, A CFD study into the influence of unsteady interference on wind turbine surge motion, Renewable Energy 90 (2016).

[20] T. Sebastian, M. Lackner, Development of a free vortex wake method code for offshore floating wind turbines, Renewable Energy 46 (2012).

[21] H. Lee, D. Lee, Effects of platform motions on aerodynamic performance and unsteady wake evolution of a floating offshore wind turbine, Renewable Energy 143 (2019).

[22] N. Ramos-Garcia, S. Kontos, A. Pegalajar-Jurado, S. Horcas, H. Bredmose, Investigation of the floating IEA wind 15 MW RWT using vortex methods Part I: Flow regimes and wake recovery, Wind Energy 25 (2021).

[23] K. Shaler, B. Anderson, L. Martines-Tossas, E. Branlard, N. Johnson, Comparison of free vortex wake and blade element momentum results against large-eddy simulation results for highly flexible turbines under challenging inflow conditions, Wind Energy Science (2023).

[24] T. Tran, D. Kim, The platform pitching motion of floating offshore wind turbine: A preliminary unsteady aerodynamic analysis, Journal of Wind Engineering and Industrial Aerodynamics 142 (2015).

[25] J. de Vaal, M. Hansen, T. Moan, Effect of wind turbine surge motion on rotor thrust and induced velocity, Wind Energy 17 (2014).

[26] L. Cottura, R. Caradonna, R. Novo, A. Ghigo, G. Bracco, G. Mattiazzo, Effect of pitching motion on production in a OFWT, Journal of Ocean Engineering and Marine Energy (2022).

[27] M. Chen, P. Xiao, H. Zhou, C. Li, X. Zhang, Fully coupled analysis of an integrated floating wind-wave power generation platform in operational sea-states, Front. Energy Res. (2022).

[28] M. Mahfouz, C. Molins, P. Trubat, S. Hernandez, F. Vigara, A. Jurado-Pegalajar, H. Bredmose, M. Salari, Response of the international energy agency

(IEA) wind 15 MW WindCrete and Activefloat floating wind turbines to wind and second-order waves, Wind Energy Science 6 (2021).

[29] L. Cottura, R. Caradonna, A. Ghigo, R. Novo, G. Bracco, G. Mattiazzo, Dynamic modeling of an offshore floating wind turbine for application in the Mediterranean Sea, Energies 14 (2021).

[30] A. Fontanella, G. Colpani, M. De Pascali, S. Muggiasca, M. Belloli, Assessing the impact of waves and platform dynamics on floating wind-turbine energy production, Wind Energy Science (2024).

[31] M. Buhl, G. Hayman, J. Jonkman, B. Jonkman, R. Mudafort, A. Platt, M. Sprague, OpenFast (2022).
URL {https://github.com/OpenFAST}

[32] T. J. Larsen, A. M. Hansen, A. Baumgart, H. A. Madsen, HAWC2: The Horizontal Axis Wind turbine simulation Code, version 2, Tech. rep., Risø National Laboratory, Technical University of Denmark (2007).

[33] P. Moriarty, A. Hansen, AeroDyn theory manual, Tech. rep., US National Renewable Energy Laboratory (2005).

[34] A. Ning, Using blade element momentum methods with gradient-based design optimization, Structural and Multidisciplinary Optimization (2021).

[35] D. Marten, J. Peukert, G. Pechlivanoglou, C. Nayeri, C. Paschereit, Qblade: An open source tool for design and simulation of horizontal and vertical axis wind turbines, International Journal of Emerging Technology and Advanced Engineering (2013).

[36] J. Ledoux, S. Riffo, J. Salomon, Analysis of the blade element momentum theory, SIAM Journal on Applied Mathematics 81 (2021).

[37] L. Prandtl, Applications of the vortex theory to propeller and rotor systems (1923).

[38] H. Glauert, The analysis of experimental results in the windmill brake and vortex ring states of an airscrew, ARCR R and M (1926).

[39] H. Snel, J. G. Schepers, Joint investigation of dynamic inflow effects and implementation of an engineering method, Tech. rep., Netherlands (1995).

[40] C. Ferreira, W. Yu, A. Sala, A. Vire, Dynamic inflow model for a floating horizontal axis wind turbine in surge motion, Wind Energy Science 7 (2022).

[41] S. Mancini, K. Boorsma, G. Schepers, F. Savenije, A comparison of dynamic inflow models for the blade element momentum method, Wind Energy Science 8 (2023).

[42] D. Apsley, P. Stansby, Unsteady thrust on an oscillating wind turbine: Comparison of blade-element momentum theory with actuator-line CFD, Journal of Fluids and Structures 98 (2020).

[43] R. Bergua, A. Robertson, J. Jonkman, E. Branlard, A. Fontanella, M. Belloli, P. Schito, A. Zasso, G. Persico, A. Sanvito, E. Amet, C. Brun, G. Campaña-Alonso, R. Martín-San-Román, R. Cai, J. Cai, Q. Qian, W. Maoshi, A. Beardsell, G. Pirrung, N. Ramos-García, W. Shi, J. Fu, R. Corniglion, A. Lovera, J. Galván, T. A. Nygaard, C. R. dos Santos, P. Gilbert, P. Joulin, F. Blondel, E. Frickel, P. Chen, Z. Hu, R. Boisard, K. Yilmazlar, A. Croce, V. Harnois, L. Zhang, Y. Li, A. Aristondo, I. M. Alonso, S. Mancini, K. Boorsma, F. Savenije, D. Marten, R. Soto-Valle, C. Schulz, S. Netzband, A. Bianchini, F. Papi, S. Cioni, P. Trubat, D. Alarcon, C. Molins, M. Cormier, K. Brüker, T. Lutz, Q. Xiao, Z. Deng, F. Haudin, A. Goveas, OC6 project Phase III: validation of the aerodynamic loading on a wind turbine rotor undergoing large motion caused by a floating support structure, Wind Energy Science (2023).

[44] A. Fontanella, I. Bayati, R. Mikkelsen, M. B. A. Zasso, UNAFLOW: a holistic wind tunnel experiment about the aerodynamic response of floating wind turbines under imposed surge motion, Wind Energy Science (2021).

[45] F. Papi, J. Jonkman, A. Robertson, A. Bianchini, Going beyond BEM with BEM: an insight into dynamic inflow effects on floating wind turbines [preprint], Wind Energy Science Discussions (2023).

[46] M. Hansen, Aerodynamics of Wind Turbines, Routledge, 2015.

[47] H. Glauert, Aerodynamic Theory, Springer, 1935.

[48] M.L. Buhl, Jr, A new empirical relationship between thrust coefficient and induction factor for the turbulent windmill state, Tech. rep., National Renewable Energy Laboratory (2005).

[49] R. Lupton, Frequency-domain modelling of floating wind turbines, Ph.D. thesis, University of Cambridge (2014).

[50] E. Branlard, M. Gaunaa, Cylindrical vortex wake model: right cylinder, Wind Energy 18 (2015).

[51] S. Øye, A simple vortex model of a turbine rotor, Proc. of the third IEA Symposium on the Aerodynamics of Wind Turbines, ETSU (1990).

[52] E. Gaertner, J. Rinker, L. Sethuraman, F. Zahle, B. Anderson, G. Barter, N. Abbas, F. Meng, P. Bortolotti, W. Skrzypinski, G. Scott, R. Feil, H. Bredmose, K. Dykes, M. Shields, C. Allen, A. Viselli, IEA wind TCP task 37: Definition of the IEA 15-megawatt offshore reference wind turbine, Tech. rep., National Renewable Energy Laboratory (2020).

[53] N. Abbas, D. Zalkind, L. Pao, A. Wright, A reference open-source controller for fixed and floating offshore wind turbines, Wind Energy Science Discussions (2021).

[54] J. Schluntz, R.H.J. Willden, The effect of blockage on tidal turbine rotor design and performance, Renewable Energy (2015).

[55] A. Wimshurst, R.H.J. Willden, Tidal power extraction on a streamwise bed slope, Ocean Engineering (2016).

[56] F. Zilic de Arcos, A. Wimshurst, R.H.J. Willden, G. Pinon, C.R. Vogel, A CFD study on high-thrust corrections for blade element momentum models, Wind Energy (2023).

[57] M.H. Bin Osman, Unsteady loading on floating horizontal axis wind turbine, Ph.D. thesis, University of Oxford (2022).

[58] C. Bak, F. Zahle, R. Bitsche, T. Kim, A. Yde, L. Henriksen, M. Hansen, J. Blasques, M. Gaunaa, A. Natarajan, The DTU 10 MW reference wind turbine, Tech. rep., Danish Technical University (2013).

[59] F. Taruffi, F. Novais, A. Vire, An experimental study on the aerodynamic loads of a floating offshore wind turbine under imposed motions, Wind Energy Science (2024).

[60] A. Fontanella, G. Da Pre, M. Belloli, Integrated design and experimental validation of a fixed-pitch rotor for wind tunnel testing, Energies (2023).

[61] C. Bak, F. Zahle, R. Bitsch, K. Robert, T. Kim, A. Yde, L. Henriksen, M. Hansen, J. Blasques, M. Gaunaa, A. Natarajan, The DTU 10-MW reference wind turbine, DTU Library (2013).

[62] C. Allen, A. Viselli, H. Dagher, A. Goupee, E. Gaertner, N. Abbas, M.Hall, G. Barter, Definition of the UMaine VolturnUS-S reference platform developed for the IEA wind 15-megawatt offshore reference wind turbine, Tech. rep., National Renewable Energy Laboratory (2020).

[63] A. Fontanella, A. Facchinetti, S. D. Carlo, M. Belloli, Wind tunnel investigation of the aerodynaic response of two 15 MW floating wind turbines, Wind Energy Science (2022).

[64] S. Øye, Fast pitch step experiments in a wind tunnel and comparison with computational methods, Proceedings on the 1996 European Union Wind Energy Conference (1996).

[65] J. G. Schepers, Engineering models in wind energy aerodynamics, Ph.D. thesis, Technical University of Delft (2012).

[66] H. Snel, J. Schepers, JOULE1: joint investigation of dynamic inflow effects and implementation of an engineering method, Tech. rep., Energy Research Centre of the Netherlands, ECN (1994).

[67] E. Ransley, S. Brown, E. Edwards, T. Tosdevin, K. Monk, A. Reynolds, D. Greaves, M. Hann, Real-time hybrid testing of a floating offshore wind turbine useing a surrogate-based aerodynamic emulator, ASME Open J. Engineering (January 2023).

[68] H. Diaz, C. G. Soares, An integrated GIS approach for site selection of floating offshore wind farms in the atlantic continental european coastline, Sustainable Energy Reviews 134 (2020).

[69] A. Martinez, G. Iglesias, Site selection of floating offshore wind through levelised cost of energy: A case study in ireland, Energy Conversion and Management 266 (2022).

[70] M. Mahfouz, M. Salari, S. Hernandez, F. Vigara, C. Molins, P. Trubat, H.Bredmose, A. Pegalajar-Jurado, Public design and FAST model of the two 15MW float-turbine concepts, Tech. rep., Corewind (2020).

[71] J. Jonkman, S. Butterfield, W. Musial, G. Scott, Definition of a 5-MW reference wind turbine for offshore system development, Tech. rep., National Renewable Energy Laboratory (2009).

[72] M. Hansen, L. Henriksen, Basic DTU Wind Energy controller, no. 0028 in DTU Wind Energy E, DTU Wind Energy, Denmark, 2013.

[73] J. Dabiri, Theoretical framework to surpass the Betz limit using unsteady fluid mechanics, Physics Review 5 (2020).

[74] M. Hall, S. Housner, D. Zalkind, P. Bortolotti, D. Ogden, G. Barter, An open-source frequency-domain model for floating wind turbine design optimization, The Science of Making Torque from Wind (TORQUE) (2022).

[75] International Electrotechnical Commission, OD-554-1 Type Certification Scheme for Small Wind Turbines, `https://www.iec.ch`, geneva, Switzerland (2021).

[76] DNV, DNV-ST-0437: DNV Standard - Loads and Site Conditions for Wind Turbines, `https://www.dnv.com`, høvik, Norway (2021).

[77] R. Damiani, D. Davis, Design load basis guidance for distributed wind turbines, Tech. rep., National Renewable Energy Laboratory (2024).

[78] Copernicus Climate Change Service (C3S) Climate Data Store (CDS), Copernicus climate change service (2024): ERA5 hourly data on single levels from 1940 to present (2024).

[79] F. Zilic de Arcos, C. Vogel, R. Wilden, A numerical study on the hydrodynamics of a floating tidal rotor under the combined effects of currents and waves, Ocean Engineering, Volume 286, Part 2 (2023).

[80] ANSYS, ANSYS student AQWA, release 2024 R1, help system, AQWA theory manual, Tech. rep., ANSYS, inc (2024).

[81] ANSYS, ANSYS student AQWA, release 2024 R1, help system, AQWA reference manual, Tech. rep., ANSYS, inc.

[82] Technical Committee TC 88 Wind energy generation systems, IEC61400-1, Tech. rep., International Electrotechnical Commission (2019).

[83] H. Ahn, H. Shin, Experimental and numerical analysis of a 10 MW floating offshore wind turbine in regular waves, Energies (2020).

[84] S. Loughney, J. Wang, M. Bashir, M. Armin, Y. Yan, Development and application of a multiple-attribute decision-analysis methodology for site selection of floating offshore wind farms on the UK continental shelf, Sustainable Energy Technologies and Assessments 47 (2021).

[85] H. Diaz, C. G. Soares, A novel multi-criteria decision-making model to evaluate floating wind farm locations, Renewable Energy 185 (2022).

[86] J. Marin, A. Barroso, F. Paris, J. Canas, Study of fatgiue damage in wind turbine blades, Engineering Failure Analysis (2009).

[87] K. Ravikumar, R. Subbiah, N. Ranganathan, J. Bensingh, A. Kader, S. Nayak, A review on fatigue damages in the wind turbines: Challenges in determining and reducing fatigue failures in wind turbine blades, Wind Engineering (2020).

[88] A. Saenz-Aguirre, A. Ulazia, G. Ibarra-Berastegi, J. Saenz, Floating wind turbine energy and fatigue loads estimation according to climate period scaled wind and waves, Energy Conversion and Management (2022).

[89] A. Lopez, Offshore wind resource assessment for the United States, Tech. Rep. NREL/TP-5000-81784, National Renewable Energy Laboratory (2022).

[90] S. Cavazzi, A. Dutton, An offshore wind energy geographic information system (OWE-GIS) for assessment of the UK's offshore wind energy potential, Renewable Energy (2016).

[91] A. Pillai, T. Gordelier, P. Thies, C. Dormenval, B. Wray, R. Parkinson, L. Johanning, Anchor loads for shallow water mooring of a 15 MW floating wind turbine - Part I: Chain catenary moorings for single and shared anchor scenarios, Ocean Engineering (2022).

[92] American Petroleum Institute, API RP 2SK: Design and analysis of stationkeeping systems for floating offshore structures, Tech. rep., American Petroleum Institute (2024).

[93] H. Hersbach, B. Bell, P. Berrisford, G. Biavati, A. Horányi, J. M. Sabater, J. Nicolas, C. Peubey, R. Radu, I. Rozum, D. Schepers, A. Simmons, C. Soci, D. Dee, J.-N. Thépaut, ERA5 hourly data on single levels from 1940 to present, Copernicus Climate Change Service (C3S) Climate Data Store (CDS) (2025).

[94] F. Pedregosa, G. Varoquaux, A. Gramfort, V. Michel, B. Thirion, O. Grisel, M. Blondel, P. Prettenhofer, R. Weiss, V. Dubourg, J. Vanderplas, A. Passos, D. Cournapeau, M. Brucher, M. Perrot, E. Duchesnay, Scikit-learn: Machine learning in python, J. Mach. Learn. Res. (2011).

[95] A. P. Dempster, N. M. Laird, D. B. Rubin, Maximum likelihood from incomplete data via the EM algorithm, Journal of the Royal Statistical Society. Series B (Methodological) (1977).

[96] R. Marcille, M. Thiébaut, P. Tandeo, J. Filipot, Gaussian mixture models for the optimal sparse sampling of offshore wind resource, Wind Energy Science (2023).

[97] L. Ricciotti, M. Picone, A. Pollice, A. Maruotti, Modelling and clustering sea conditions: Bivariate finite mixtures of generalized additive models for location, shape, and scale applied to the analysis of meteorological tides and wave heights, J. Mar. Sci. Eng. (2024).

[98] G. Schwarz, Estimating the dimension of a model, The Annals of Statistics (1978).

[99] K. Hasselmann, T.P. Barnett, E. Bouws, H. Carlson, D.E. Cartwright, K. Enke, J.A. Ewing, H. Gienapp, D.E. Hasselmann, P. Kruseman, A. Meerburg, P. Müller, D.J. Olbers, K. Richter, W. Sell, H. Walden, Measurements of wind-wave growth and swell decay during the Joint North Sea Wave Project (JONSWAP), Tech. rep., Deutsche Hydrographische Zeitschrift, Ergänzungsheft Reihe A, Hamburg, Germany (1973).

[100] A. Pecher, J. Kofoeod, Handbook of Ocean Wave Energy, Springer Open, 2016.

[101] P. Marek, T. grey, A. Hay, A study in the variation in offshore turbulence intensity around the British Isles, in: Wind Eruope Summit, 2016.

[102] T. Sheng Lun, L. Berg, R. Krishnamurthy, A. Kirincich, Validation of turbulence intensity as simulated by the Weather Research and Forecasting model of the US northeast coast, Wind Energy Science (2023).

[103] N. Bodini, J. Lundquist, A. Kirincich, Offshore wind turbines will encouter very low atmospheric turbulence, NAWEA WindTech, Journal of Physics: Conference Series (2019).

[104] Technical Committee TC 88 Wind energy generation systems, IEC61400-12, Tech. rep., International Electrotechnical Commission (2019).

[105] E. Bachynski, M. Kvittem, C. Luan, T. Moan, Wind-wave misalignment effects on floating wind turbines: Motions and tower load effects, ASME Journal of Offshore Mechanics and Arctic Engineering (2014).

[106] P. Potisomporn, T.A.A. Adcock and C.R. Vogel, Evaluating ERA5 reanalysis predictions of low wind speed events around the UK, Energy Reports (2023).

[107] D. Stockhouse, M. Phadnis, A. Henry, N. Abbas, M. Sinner, M. Pusch, L. Pao, A tutorial on the control of floating offshore wind turbines, IEEE Control Systems (2024).

[108] S. Carreno-Madinabeitia, G. Ibarra-Berastegi, J. Saenz, A. Ulazia, Long-term changes in offshore wind power density and wind turbine capacity factor in the Iberian Peninsula (1900-2010), Energy (2021).